Advances in biophysical characterisation through micron scale flow engineering

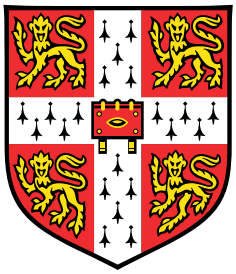

Kadi Liis Saar

Department of Chemistry
University of Cambridge

This dissertation is submitted for the degree of
Doctor of Philosophy

Trinity College

November 2018

I would like to dedicate this thesis to my family.

Declaration

I hereby declare that except where specific reference is made to the work of others, the contents of this dissertation are original and have not been submitted in whole or in part for consideration for any other degree or qualification in this, or any other university. This dissertation is my own work and contains nothing which is the outcome of work done in collaboration with others, except as specified in the text and Acknowledgements. This dissertation contains fewer than 65,000 words including appendices, bibliography, footnotes, tables and equations and has fewer than 150 figures.

Kadi Liis Saar
November 2018

Acknowledgements

First and foremost, I would like to express my greatest gratitude to my supervisor prof. Tuomas Knowles for giving me the opportunity to work in such a dynamic and interdisciplinary environment. His enthusiasm, encouragement and scientific discussions were extremely valuable to me, and I truly could not have wished for a more supportive mentor for my graduate research days, fully committed to helping my development as a scientist.

I would also like to thank prof. Christopher Dobson. Discussions with Chris were a great inspiration for my work and he has been a person whose support and guidance I knew I could always rely on. Similarly, I am very grateful to prof. David Weitz for hosting me in his laboratory at Harvard University. I benefited greatly from his frank and highly insightful comments on my work and career. I am also grateful to prof. Chris Howe for introducing me to working with cyanobacteria and for providing a lot of guidance for every aspect of the work involving their use.

Scientific research today is fuelled by collaboration and I would like to thank all my collaborators for their invaluable contributions. I feel privileged having had the chance to interact with a number of highly talented researchers of whom Dr. Pavankumar Challa and Dr. Thomas Müller deserve a special mention as I feel I have learned incredibly much from them both. Conversations with Dr Therese Herling, Dr Sean Devenish, Dr Paolo Bombelli, Dr Jerome Charmet, Dr John Heyman, Tadas Kartanas and Quentin Peter were of great help for the execution of a number of projects I worked on during my PhD. Last but not least, I am grateful to the Knowles group for generating a highly dynamic, diverse and supportive research environment, where I truly enjoyed working.

On a more personal note, I would like to thank my family. It is thanks to their support that I have been able to pursue my interests, which ultimately led to my choice

to become a scientist. My husband deserves the greatest possible gratitude for his immense and continuous support towards my endeavours.

Abstract

Advances in biophysical characterisation through micron scale flow engineering

KADI LIIS SAAR

Department of Chemistry, University of Cambridge

Proteins are the chief actor molecules of cells central to the majority of biochemical and biophysical processes that sustain life. Interactions between proteins and other biomolecules are crucial to a faultless execution of biological function, yet it has remained challenging to analyse these biomolecular interactions with current protein science tools - they commonly rely on non-physiological conditions for performing analysis, thereby compromising the ability to analyse biological interactions.

This thesis describes the development and applications of platforms that facilitate rapid analysis of heterogeneous systems of proteins and protein interactions directly in solution, under fully native conditions. I achieved this objective by fabricating micron scale structures, where, in contrast to macroscale systems, chaotic mixing of fluids and the molecules therein was suppressed. In this manner, I was able to dispense with the support structures that prevent mixing in conventional protein analysis platforms and decrease analysis times by orders of magnitude, from hours to seconds.

The first part of the thesis was centred around the use of micron scale strategies for probing proteins, protein interactions and protein self-assembly *in vitro*. First, I demonstrated a platform for performing automated high-throughput measurements on protein self-assembly in a label-free environment. I proceeded by addressing two challenges at the core of creating micron scale separation platforms - the integration of strong and stable electric fields with micron scale channels and the enhancing of the resolution limit of such separation systems. Finally, I devised and demonstrated devices for combined biomolecular separation and analysis, which allowed me to size mixtures of proteins at an unprecedented resolution and gain multidimensional data

on biomolecular systems.

The second part focussed on probing protein behaviour inside cells. I first described a strategy for detecting intracellular proteins in individual cells in a high throughput manner, offering a substantially advanced multiplexing capability in comparison to existing approaches for analysing intracellular proteins. I then focussed on a specific application of cellular biophysics and measured electrical outputs of cells. This work led to record high power outputs for systems that use biological matter for converting sunlight into electricity. To my knowledge, this was also the first demonstration of a biological solar cell equipped with energy storing capacity, the lack of which had been viewed as one of the most notable limitations of current solar cells.

Abbreviations

Aβ	Amyloid-β
BIL	Bio-layer interferometry
BPV	Biological photovoltaic devices
BSA	Bovine serum albumin
CD	circular dichroism
chl	Chlorophyll
cryo-EM	Cryogenic electron microscopy
DBCO	Dibenzocyclooctyne-amine
DLS	Dynamic light scattering
DMEM	Dulbecco's Modified Eagle Medium
DMSO	Dimethyl sulfoxide
DNA	Deoxyribonucleic acid
DTT	Dithiothreitol
EC	Electron carrier
EDTA	Ethylenediaminetetraacetic acid
EM	Electron microscopy
FACS	Fluorescence activated cell sorting
FCS	Fluorescence correlation spectroscopy
FFE	Free flow electrophoresis
FTIR	Fourier transform infrared spectroscopy
Fwd	Forward
GuHCl	Guanidinium chloride
HLPC	High pressure liquid chromatography
ID	Identifier
IPA	Isopropyl alcohol
ITC	Isothermal titration calorimetry
LED	Light-emitting diode
Lys	Lysozyme

MDS	Microscale diffusional sizing
ML	Multi layer
mRNA	Messenger RNA
MST	Microscale thermophoresis
MWCO	Molecular weight cut-off
NMR	Nuclear magnetic resonance
nt	Nucleotide
PAGE	Polyacrylamide electrophoresis
PBS	Phosphate buffer saline
PCR	Polymerase chain reaction
PDMS	Polydimethylsiloxane
PEG	Polyethylene glycol
PFO	Perfluorooctanol
PGME	Propylene glycol monomethyl ether acetate
pI	Isoelectric point
PKB	Protein kinase B
PV	Photovoltaic devices
qPCR	Quantitative polymerase chain reaction
Rev	Reverse
rpm	Rotations per minute
SDS	Sodium dodecyl sulphate
SEC	Size exclusion chromotography
SEC-MALS	Size exclusion chromotography with multi-angle light scattering
SEM	Scanning electron microscopy
SL	Single layer
SPR	Surface plasmon resonance
ThT	Thioflavin T
UMI	Unique molecular identifier
UV	Ultraviolet
μ-FFE	Microscale free-flow electrophoresis
2D	Two-dimensional
3D	Three-dimensional

Nomenclature

A	cross-sectional area of a microfluidic channel
A_{anode}	anodic area
$A_{cathode}$	cathodic area
c_i	concentration of species i
d	diameter
d_H	hydraulic diameter
d_{ID}	internal diameter
D	diffusion coefficient
E	electric field strength
F	Faraday constant
f_D	friction factor
g	gravitational acceleration
h	height of a microfluidic channel
I	current
k	Boltzmann constant
L	length of a microfluidic channel
N	number of channels
N_A	Avogadro constant
P	Pressure
ΔP	pressure drop
p	power
Pe	Péclet number
Q	flow rate
q	charge
R	universal gas constant
R_{EL}	electrical resistance
R_H	hydrodynamic radius
R_{HD}	hydraulic resistance

r	rate
Re	Reynolds number
T	temperature
t	time
t_{res}	residence time
u	velocity
V	voltage
ΔV_{eff}	effective applied voltage
v	volume
w	width of a microfluidic channel
x_{diff}	diffused distance
$x_{deflection}$	deflected distance
Δ	uncertainty
η	viscosity
η_{eff}	efficiency
κ	conductivity
$\lambda_{excitation}$	excitation wavelength
μ_{el}	electrophoretic mobility
ρ	density

Publications

My research has resulted in a number of manuscripts, which have been published or submitted for publication. Six of these in particular form the basis for the work presented in this thesis:

[1] Therese Herling*, Aviad Levin*, **Kadi L Saar***, Christopher M Dobson, Tuomas PJ Knowles, "Microfluidic approaches for probing amyloid assembly and behaviourm", *Lab on a Chip*, 18**(7)**, 2018.
Chapter 1

[2] **Kadi L Saar**, Emma V Yates, Thomas Müller, Severine Saunier, Christopher M Dobson, Tuomas PJ Knowles, "Automated *ex situ* assays of amyloid formation on a microfluidic platform", *Biophysical Journal*, 110**(3)**, 2016.
Chapter 3

[3] **Kadi L Saar***, Yingbo Zhang*, Thomas Müller, Challa P Kumar, Sean Devenish, Andrew Lynn, Urszula Lapinska, Xiaoting Yang, Sara Linse, Tuomas PJ Knowles, "On-chip label-free protein analysis with downstream electrodes for direct removal of electrolysis products", *Lab on a Chip*, 18**(1)**, 2018.
Chapter 4

[4] **Kadi L Saar**, Thomas Müller, Jerome Charmet, Pavan Kumar Challa, Tuomas PJ Knowles,"Enhancing the resolution of micro free flow electrophoresis through spatially controlled sample injection", *Analytical Chemistry*, 90**(15)**, 2018.
Chapter 4

[5] **Kadi L Saar**, Quentin Peter, Pavan Kumar Challa, Therese W. Herling, Tuomas PJ Knowles, "Rapid two-dimensional characterisation of proteins in solution", accepted.
Chapter 5

[6] **Kadi L Saar**, Paolo Bombelli, David J Lea-Smith, Toby Call, Eva-Mari Aro, Thomas Müller, Christopher J Howe, Tuomas PJ Knowles, "Enhancing power density of biophotovoltaics by decoupling storage and power delivery", *Nature Energy*, 3**(1)**, 2018.
Chapter 7

In addition to the publications listed above, I have been fortunate to be involved in a number of collaborations and for the methods described in this thesis to find further application.

[1] Thomas CT Michaels, Alexander J Dear, Julius B Kirkegaard, **Kadi L Saar**, David A Weitz, Tuomas PJ Knowles, "Fluctuations in the kinetics of linear protein self-assembly", *Physical Review Letters*, 116**(25)**, 2016.

[2] Urszula Lapinska, **Kadi L Saar**, Emma V Yates, Therese W Herling, Thomas Müller, Pavan K Challa, Christopher M Dobson, Tuomas PJ Knowles, "Gradient-free determination of isoelectric points of proteins on chip", *Physical Chemistry Chemical Physics*, 19**(34)**, 2017.

[3] Lingling Kong, **Kadi L Saar**, Raphael Jacquat, Liu Hong, Aviad Levin, Hongze Gang, Ruqiang Ye, Bozhong Mu, Tuomas PJ Knowles"Mechanism of biosurfactant adsorption to oil/water interfaces from millisecond scale tensiometry measurements", *Interface focus*, 7**(6)**, 2017.

[4] Pavan Kumar Challa*, Quentin Peter*, Maya A Wright, Yuewen Zhang, **Kadi L Saar**, Jacqueline A Carozza, Justin LP Benesch, Tuomas PJ Knowles, "Real-Time Intrinsic Fluorescence Visualization and Sizing of Proteins and Protein Complexes in Microfluidic Devices", *Analytical Chemistry*, 90**(6)**, 2018.

[5] Michele Perni, Pavan K Challa, Julius B Kirkegaard, Ryan Limbocker, Mandy Koopman, Maarten C Hardenberg, Pietro Sormanni, Thomas Müller, **Kadi L Saar**, Lianne WY Roode, Johnny Habchi, Giulia Vecchi, Nilumi Fernando, Samuel Casford, Ellen AA Nollen, Michele Vendruscolo, Christopher M Dobson, Tuomas PJ Knowles, "Massively parallel *C. elegans* tracking provides multi-dimensional fingerprints for phenotypic discovery", *Journal of Neuroscience Methods*, 12**(306)**, 2018.

[6] Yuewen Zhang, Emma V Yates, Liu Hong, **Kadi L Saar**, Georg Meisl, Christopher M Dobson, Tuomas PJ Knowles, "On-chip measurements of protein unfolding from direct observations of micron-scale diffusion", *Chemical Science*, 9**(14)**, 2018.

[7] William E Arter, Jerome Charmet, Jinglin Kong, Kadi L Saar, Therese W Herling, Thomas Muüller, Ulrich F Keyser, Tuomas PJ Knowles, "Combining affinity selection and specific ion mobility for microchip protein sensing", *Analytical Chemistry*, 90**(17)**, 2018.

[8] Maria J Matos, Claudio D Navo, Tuuli Hakala, Xhenti Ferhati, Ana Guerreiro, David Hartmann, **Kadi L Saar**, Isamel Compañón, Francisco Corzana, Tuomas PJ Knowles, Gonzalo Jimenéz-Osés and Gonçalo JL Bernardes, "Quaternization of Vinyl/Alkynyl Pyridine Enables Ultrafast Cysteine-Selective Protein Modification and Charge Modulation", *Anglewandte Chemie International Edition*, in press.

[9] Maya A Wright, Simone Ruggeri, **Kadi L Saar**, Pavankumar Challa, Justin LP Benesch, Tuomas PJ Knowles, "Insights into αB-crystallin polydispersity from native microfluidic high-field electrophoresis measurements", under review.

[10] Tadas Kartanas, Tom Scheidt, Quentin Peter, **Kadi L Saar**, Thomas Müller, Pavan Kumar Challa, Sean Devenish, Tuomas PJ Knowles, "Multidimensional protein characterisation using liquid chromatography combined with microfluidics", in preparation.

[11] Yuewen Zhang*, Maya Wright*, Pavan Kumar Challa, Alexey Morgunov,**Kadi L Saar**, Quentin AE Peter, Emma V Yates-Sukdao, Sean Devenish, Chrisopher M Dobson, Tuomas PJ Knowles, "Top-down protein identification on a microfluidic platform", in preparation.

[12] Annie HK Chiu, Tadas Kartanas, Sean Devenish, Carina Luxhoj, **Kadi L Saar**, Tuomas PJ Knowles. "High Sensitivity Chemiluminescent Detection of Proteins On-Chip", in preparation.

[13] Alexander PM Guttenplan*, **Kadi L Saar***, Marc Rodriguez-Garcia, Laura S. Itzhaki, Tuomas PJ Knowles, "Parallelised Mechanical Testing of Microscale Soft Materials on the Micron Scale", in preparation.

Additionally, some of the devices presented in this thesis have been filed and licensed our for product development:

[1] GB 1720627.7, Fluidic Apparatus and Methods. Filed (2017) and licensed (2018)

[2] GB 1815360.1, Improvements in or relating to profiling of particles using microfluidic devices. Filed (2018) and licenced (2018).

[3] GB1819033.0. Particle Characterization Using Optical Microscopy. Filed (2018).

[4] GB1819029.8. Optical microscopy. Filed (2018).

[5] GB1820870.2. Detection of components. Filed (2018).

Table of contents

List of figures

List of tables

Chapter 1

Introduction

This chapter is in part based on the publication:
*Herling TW and Levin A and Saar KL et al., Lab Chip, 18(**7**), 999-1016, 2018.*

1.1 Proteins and protein interactions

Proteins are the chief effector molecules of cells, forming the basis of the molecular machinery that sustains life. Proteins and their complexes play a central role in a diverse range of cellular processes, including replication of genetic information, catalysis of metabolic reactions, transportation of cargo into and out of cells, transmission of the signals involved in body's immune response against foreign invaders and regulation of the folding and unfolding of other proteins, thereby enabling their function [1–3]. Thus, a faultless behaviour of proteins is of paramount importance to well balanced cellular function and, ultimately, to our well being, whereas its disrupted behaviour, on the contrary, is associated with the onset and progression of an increasingly larger number of disease states [4–7].

While the analysis of individual proteins can shed light onto their key properties and thereby aid us in understanding protein function and activity, in the dynamic and crowded environment of cells [8–10], proteins are in constant contact with each other and frequently carry out their functions as part of larger complexes or assemblies [11–16]. Indeed, any one of the aforementioned biochemical processes takes place through an interplay between proteins of differing functions or involve their interactions with other biomolecules, such as lipids, oligonucleotides or small molecule ligands. It has been estimated that over 80% of proteins do not perform their function on their own but through interacting with other molecules [17] with the interactions being frequently transient and non-covalent in their nature [18–20]. This tendency firmly highlights the requirement for analysing proteins with tools that function directly in solution and under native conditions where such biomolecular interactions can be

preserved. However, due to the tendency of fluids to uncontrollably mix, in-solution analysis of heterogeneous mixtures of proteins has remained a challenging goal to reach. As such, the analysis of heterogeneous protein mixtures is usually achieved through operation in the gaseous phase or on a solid support medium as I will discuss in more detail in Section 1.2. In both of these scenarios, care has to be taken to ensure that all interaction between proteins and their binding partners remain intact when samples are transferred away from their native solution phase.

In this thesis, I focus on the development and application of methods that permit *in vitro* systems of proteins, protein complexes and protein interactions to be probed directly in solution. I will achieve this objective predominantly through the use of micron scale fabrication and flow engineering approaches that allow exerting tight control over fluid behaviour and, thereby, quantitative characterisation of protein properties and behaviour. Moreover, I will also explore the possibilities of extending these analysis strategies to describing the behaviour of intact cells and to detecting and probing proteins inside a cellular environment.

1.2 Protein characterisation and analysis tools

The past decades have seen remarkable developments in techniques that permit highly accurate structural characterisation of biomolecules, often down to atomic resolution. X-ray crystallography and, as of more recently, cryogenic electron microscopy (cryo-EM) in particular have extensively advanced our understanding of the structures of key proteomic species [21–26]. These methods have been historically used for resolving the structures of individual proteins, yet recent advancements in the sample preparation process have allowed their application to resolving the structures of macromolecular complexes, such as ribosomes [27, 28].

While the focus of aforementioned techniques has been to obtain highly resolved structural information on proteins in their fixed states, different types of analysis approaches have been developed for probing the dynamic behaviour of proteins. The latter objective can be achieved when the analysis is performed in a rapid manner and in the native environment of biomolecules, which in the case of *in vitro* studies is usually mimicked through the use of physiological buffers. Such conditions ensure that the interactions between protein molecules or between proteins and their ligands are fully preserved throughout the analysis while the rapid analysis speeds guarantee that it is possible to probe the dynamic behaviour of such

protein based systems.

In-solution characterisation of proteins can be achieved through a number of biophysical methods. For instance, dynamic light scattering (DLS) [29], and fluorescence correlation spectroscopy (FCS) [30] are widely used techniques for non-invasively obtaining information on the key biophysical properties of biomolecules. Specifically, by correlating the fluctuations in scattered (DLS) or fluorescent (FCS) signals over time, these techniques yield information on the diffusional movement of molecules, which in turn provides insight into their hydrodynamic radii. Both of these techniques have been used widely for sizing and characterising homogeneous biomolecular samples, including proteins and their complexes [31–34]. Their direct application to analysing heterogenous biomolecular samples, however, has remained limited. The latter objective could be achieved by deconvoluting the observed fluorescence or scattering traces, which is an ill-posed inverse problem [35]. In the case of DLS, accurate sizing has been further challenged by the fact the intensity of scattered light is proportional to the sixth power of particle size, which results in the presence of larger species masking signals from smaller ones [29]. Moreover, DLS often requires samples at concentrations exceeding the biologically relevant range [16]. For the characterisation of heterogenous samples, a micron scale diffusional sizing approach based on tracking the movement of molecules both in space and time was recently described [36]. Using such a two-dimensional tracking strategy, the accessible information content was increased and, thus, the deconvolution capability of the method enhanced in comparison to prevoiusly described in-solution sizing approaches. Its performance, however, was nevertheless observed to become limited when the analytes did not exhibit a few fold difference in their sizes, which in biological mixtures occurs only for carefully chosen specimens [16, 37, 38].

Another type of in-solution protein analysis method involves spectroscopic characterisation. Indeed, spectral signatures of proteins can yield a myriad of information about the positioning of atoms within a protein and, thereby, about their structure. In this context, nuclear magnetic resonance spectroscopy (NMR) has been used to obtain accurate predictions about the structure of proteins directly in solution and has been applied for characterising samples that cannot be crystallised straightforwardly as is required for X-ray crystallography [39]. Other spectroscopy based approaches, such as Fourier-transform infrared spectroscopy (FTIR) [41, 42] and far-UV circular dichroism spectroscopy (CD) [43] do not resolve the structure of proteins but can be used for effectively examining the secondary structures of proteins and specifically, for detecting the presence of features, such as α-helices, random coils and β-sheets. These approaches have been applied very widely for obtaining highly time-resolved insight into the folding, unfolding and misfolding events of proteins [41].

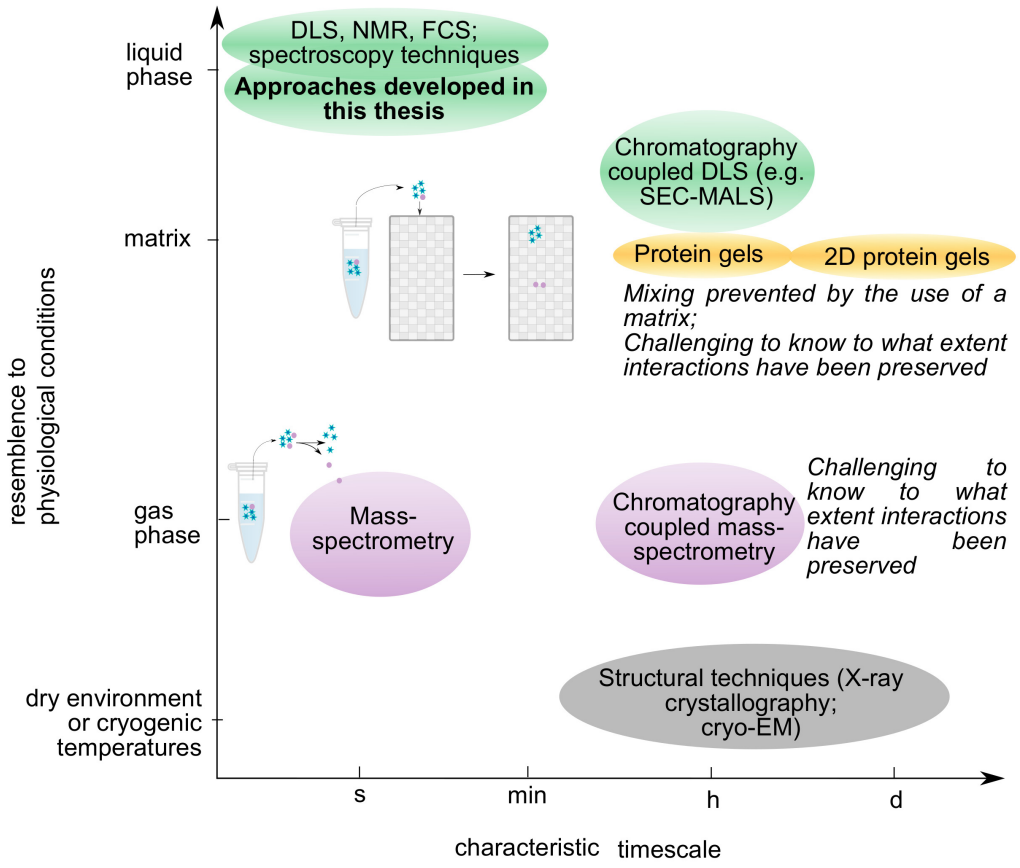

Fig. 1.1 Commonly used protein characterisation tools and their characteristic features. In this thesis we focus on the development of methods that enable protein behaviour to studied on rapid timescales and under conditions that closely resemble physiological environments.

As all the aforementioned in-solution characterisation approaches work the best on homogeneous proteins samples, when heterogeneous mixtures of proteins are to studied, these approaches are usually coupled to an upstream separation process, so that each component or fraction in the mixtures could be analysed sequentially. While it would be, in principle, desirable to perform this separation process also directly in solution and on a similarly rapid timescale (Figure 1.1), a fundamental challenge associated with performing protein or any other type of biomolecular analysis directly in solution is the tendency of diffusion and random motion to oppose orderly separation and analysis. It is conventional, therefore, to perform protein separation step through the integration of physical matrices that keep molecules of similar sizes together. Indeed, chromatography based approaches, including various forms of gel electrophoresis (e.g. agarose and polyacrylamide gel electrophoresis (PAGE)) and column chromatography (e.g. size exclusion or ion-exchange chromatography), have been at the centre of protein purification and analysis for decades and they can be performed as one-dimensional or as two-dimensional separation processes. The separated species are subsequently characterised either through a biochemical method, such as an immunoassay (Western blot) or a biophysical characterisation process, such as light scattering. In this context, SEC-MALS (size exclusion chromatography with multi-angle light scattering) has been actively used to obtain a unique insight into the polydispersity of specific types of biomolecular mixtures [44, 45].

An alternative strategy to working with heterogeneous mixtures of proteins involves transferring the sample into gaseous phase, as is the case for mass spectrometry based analysis. Such a strategy allows separating the formed ions based on their mass-to-charge ratio to detect the components and infer their charges sequentially. Mass-spectrometry based analysis approaches have for many decades yielded extremely high resolution information on the molecular weights of biomolecules and have through this capability extensively advanced our understanding of protein based systems [46, 47]. Its more recent versions, such as tandem mass spectrometry (MS/MS) have enabled the quaternary structure and topology of various protein complexes to be elucidated [48, 49]. Mass-spectrometry is often coupled to upstream separation processes in order to simplify the complexity of the sample prior analysis [50, 51]. This reduction in complexity has been achieved through integrating it with chromatography based approaches, such as liquid chromatography (LC-MS), or through gas-phase based ion mobility spectrometry (IMS-MS) and have thereby enabled polydisperse mixtures of proteins to be characterised at resolutions unachievable with any other protein characterisation method [52, 53]. It is important to note that while the recent decades have seen extensive research into the approaches how to best ionise the proteins and their complexes in particular in a manner where they remain as close to their in-solution state as possible and these efforts have led to the emergence of a term “native mass-spectrometry” [54], it is challenging to be fully certain whether the ionised sample fully corresponds its biological solution state.

An additional set of techniques have been developed and used for specifically probing interactions between proteins. In this context, surface plasmon resonance (SPR) measurements have been employed across a variety of biological research fields to determine the binding affinities between proteins and their molecular binding partners [55, 56]. Notably, a systematic comparison of binding affinity measurements has revealed that SPR measurements are frequently reporting considerably lower binding affinities that gas-phase and in-solution measurements [57]. It has been hypothesised to be the use of a dextran matrix involved in the immobilisation step that contributes to this difference through a low affinity binding of the target protein to the dextran [58]. A number of other label-free surface based and surface-free techniques have been developed to overcome this limitation. In particular, bio-layer interferometry (BIL) based measurements have been shown to yield high quality data on the strength of various protein-ligand interactions and have offered the possibility to perform high-throughput screening studies [59–61]. Isothermal titration calorimetry (ITC) and microscale thermophoresis (MST) have been used to probe protein interactions directly in solution in an immobilisation-free manner [62]. While the former approach has traditionally required relatively large sample sizes and a relatively long measurement timescale, which has limits its applications, the latter approach has been developed and commercialised only relatively recently [63] and has already been actively used for probing a wide variety of biomolecular systems [62, 64, 65].

Last but not least, some of the most valuable and frequently used protein approaches involve the introduction of chemical specificity to the analysis through the use of affinity reagents, such as antibodies or aptamers. Specifically, enzyme-linked immunosorbent assays [66, 67], Western blots [68–70] and proximity extension and ligation assays [71, 72] are all frequently used molecular biology tools when highly heterogenous mixtures of proteins, including cell lysates, are to be analysed. However, in contrast to approaches described earlier in this Section, their use is restricted to the cases where suitable affinity reagents are available. Moreover, such probe-based approaches do not permit explorative studies and detection of hitherto unknown molecules but permit the identification of only pre-defined targets or complexes. Notably, approaches relying on chemical specificity always result in a certain degree of cross-reactivity and hence, similarly, yield best results if they are performed in combination with tools that facilitate physical separation [73].

In summary, the majority of in-solution protein analysis approaches used today are work best when homogeneous protein samples are used and usually address the problem of probing heterogenous mixtures through the integration of a matrix aided separation process. While this matrix aided separation process effectively fractionates molecules according to their biophysical or biochemical properties, the presence of such matrices can affect the relative strength of interactions and result in a preferential disassembly of selected complexes and,

ultimately, in a bias in the observed results [74]. Moreover, its use prevents the examination of samples that exhibit significant size variations, such as heterogeneous mixtures of proteins and their self-assembled species, because the larger complexes present in such mixtures obstruct the matrix pores. Last but not least, such matrix based separation approaches usually operate on the timescale of hours with even when simplest one-dimensional separation processes lasting for close to an hour. This long analysis time scale restricts the use of such matrix aided systems to only slowly evolving systems. In the work described in this thesis, I have focussed on the development of platforms that would enable the analysis of heterogeneous samples directly in solution and on rapid time-scales (Figure 1.1). These features make it possible to probe dynamic biomolecular interactions in solution and open up the possibility to study biologically relevant interactions between biomolecules under their fully native conditions.

1.3 Micron scale platforms for probing cells

In biological organisms, a significant fraction of proteins exert their function inside cells and even those that do not, are at the first instance, synthesised inside cells. While *in vitro* studies provide an effective route for probing the behaviour of proteins under well-controlled conditions, it is of utmost importance to in parallel develop and apply methods that enable probing protein behaviour inside cells.

Micron scale analysis platforms have been shown to serve as an attractive strategy for studying the behaviour of cells. In particular, the possibility to exert tight spatial control over fluid movement has been exploited to expose cells to various external stimuli and examine their effect on cellular growth in a much more controllable and reproducible fashion than has been possible on macroscale platforms [75, 76]. These strategies have also been used for developing organ-on-chip platforms for screening the effect of various drug candidates in conditions closely mimicking *in vivo* environments [77–79]. While these approaches focus on studying the collective behaviour of a variety of cells, the possibility to tightly control fluid behaviour micron scale platform has also been put into action for specifically probing the interactions between two neighbouring cells. Such experiments have been used to develop and understanding the molecular mechanisms that underlie cell-to-cell communication [76, 80]. In parallel, microfluidic devices have been used for separating and fractionating cells and cellular organelles as well as for spatially positioning them, which has been achieved mainly through the application of electrophoretic and dielectrophoretic fields [81, 82].

Last but not least, micron scale platforms and the possibility to encapsulate individual cells into individual compartments as will be highlighted in more detail in Section 1.4, has set the basis for performing high-throughput single cell studies. Indeed, cells are the fundamental units of living cells with their behaviour having been observed to differ substantially between cells. Micron scale channels have been for many decades used to perform high-throughput sorting of cells through approaches such as fluorescence activated cell sorting (FACS) that rely on a cellular biochemical pathway emitting a fluorescent signal indicative of the property according to which the cells are to be screened and sorted. More recently, such high-throughput single cell analysis approaches have been extended to probing the transcriptomic content of individual cells and have thereby yielded unique insight into the most fundamental biological questions in areas ranging from immunology to developmental biology [83–91]. These approaches have been to some degree extended to studying other biological molecules in cells, such as proteins or metabolites but the methods developed to date have remained limited in their throughput or in their multiplexing capability, allowing only a small number of targets to be probed simultaneously. I will discuss these developed approaches and their applications and limitations in more detail at the start of Chapter 6.

1.4 Micron scale approaches for analysing biological systems

Fluid behaviour on the micron scale differs substantially from the macroscale environment. One of the key differences between the behaviour of fluids at these two length scales is captured by the ratio of the inertial to viscous forces, also called the Reynolds number:

$$\mathrm{Re} = \frac{\text{interial forces}}{\text{viscous forces}} \sim \frac{\rho \mathrm{u} \mathrm{d}}{\eta} \tag{1.1}$$

where ρ and η are the density and the dynamic viscosity of the medium, respectively, u is velocity of the fluid and d is the characteristic length scale of the fluid movement. In the case of fluid flow inside micron scale channels, this characteristic length scale is the hydraulic diameter $\mathrm{d_H}$ of the channel.

In the work described in this thesis, the channel dimensions ranged between 1 and 2000 μm and the flow rates between 1 and 2000 μL h^{-1}. Under these conditions, the Reynolds number was estimated to be below $\mathrm{Re} \sim 10^{-1}$. As a result, the inertial movement of molecules was suppressed and molecular transport was defined by diffusion, which can be precisely controlled and modelled [92, 93]. This feature was a key factor to the strategies for probing

the properties of proteins and protein mixtures and obtaining highly accurate quantitative insight to biological systems that I will be presenting in the following chapters.

Whereas all the devices described, developed and applied in this thesis involved operation under low Reynolds number conditions, I used the arising ability to tightly control the movement of fluids to serve a range of different goals. Namely, in some of the work, I aimed to keep analyte molecules confined. I achieved this objective by designing the systems such that the relative residence times of fluids was slow in comparison to the diffusional movement of the molecules therein (Figure 1.2a, i). This relative extent of diffusion could be captured by a dimensionless quantity called Péclet number:

$$\mathrm{Pe} = \frac{t_{\mathrm{diffusive}}}{t_{\mathrm{advective}}} = \frac{{}^{L}/_{u}}{{}^{h^2}/_{D}}, \tag{1.2}$$

which was here defined as the ratio of the diffusive time scale in the y-direction and the advective time scale in the x-direction (Figure 1.2). In other studies, my objective was to generate non-physical semipermeable membranes (Figure 1.2a, ii) that could be crossed by selected species. I realised this goal by ensuring that the Péclet number for one species was significantly larger than for another. Last but not least, when my intention was to obtain quantitative information based on the diffusional movement of molecules, I ensured that the Péclet number of the analyte molecules was of an intermediate value, so that the extent of diffusional movement could be used for estimating diffusion coefficients of the analytes and thereby their hydrodynamic radii.

In addition to opening up the possibility of precisely controlling fluid behaviour and thereby maintaining the localisation of analyte molecules, the use of micron scale channels introduces additional attractive features for working with biological samples, such as the reduced sample consumption and the high recovery rate that such platforms afford [94–99]. Moreover, such platforms permit building tandem devices and combining multiple processes onto a single chip [100, 101], thereby both speeding up the analysis process and automating it. Whereas the first micron scale devices were fabricated in glass and silicon already many decades ago [102], it was during the past decade that fast and replicable approaches emerged for generating such devices out from optically transparent and easily mouldable soft polymers [103, 104]. These rapid prototyping approaches have had of central contribution to the increasing use of micron scale devices in biological and biomedical research [96, 82, 105]. In particular, it has to a very large degree been the polydimethylsiloxane (PDMS) based fabrication process through its highly reproducible yet rapid prototyping has set the basis for this advancement.

An additional attractive feature associated with the use of micron scale channels in the context of biological analysis is the possibility to generate micron scale droplets of extremely

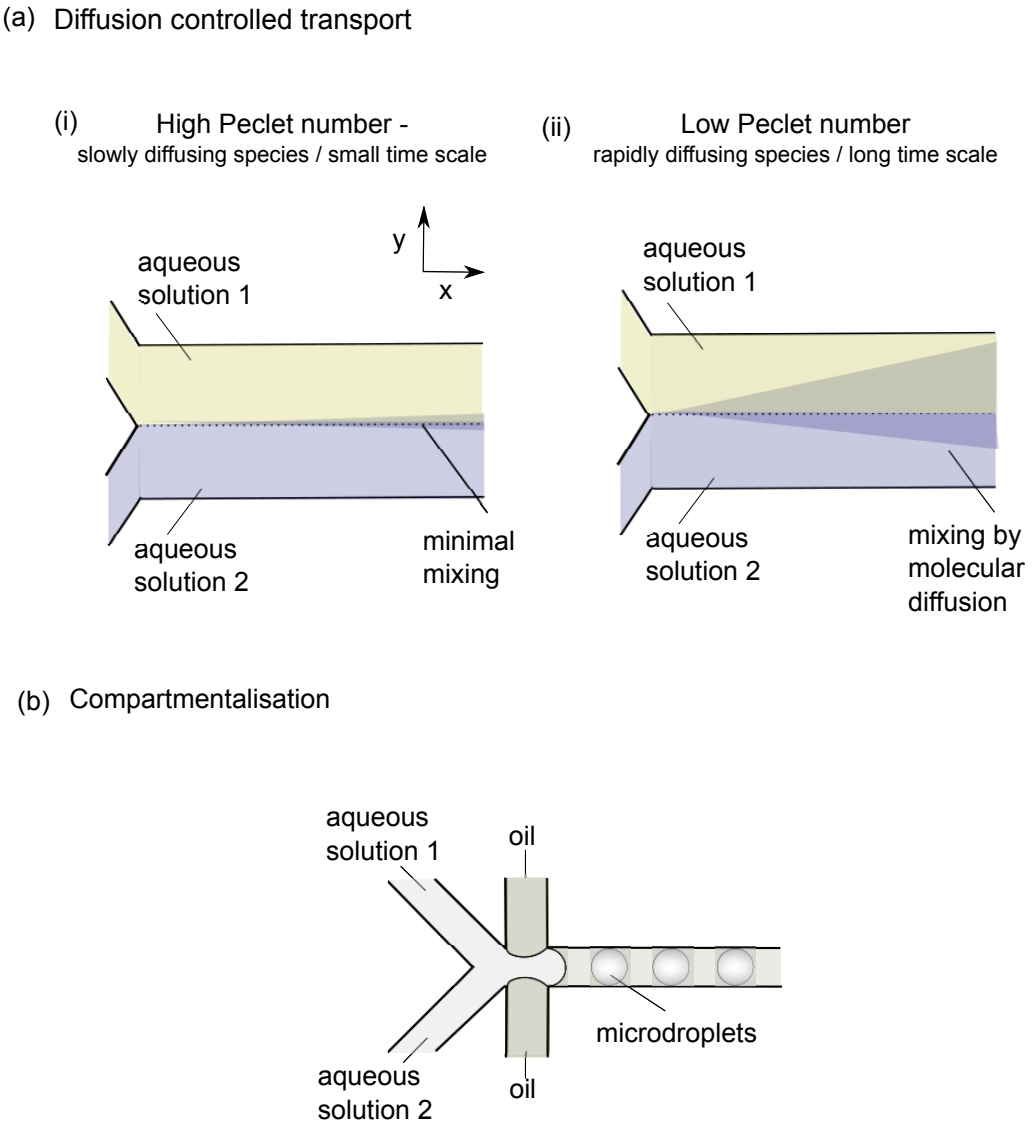

Fig. 1.2 Controlling fluid behaviour on the micron scale. **(a)** In micron scale channels, due to the absence of turbulent mixing, the movement of molecules is governed by their diffusion. This behaviour can be exploited (i) to prevent molecules from mixing (high Péclet number conditions) or (ii) to construct non-physical membranes that can be crossed selectively only by the fastest diffusing species (molecules in aqueous solution 2; low Péclet number conditions). **(b)** Micron scale channels can be used to produce miniature water-in-oil droplets that can serve as individual reactions vessels for compartmentalising biochemical reactions or biophysical processes.

uniform volumes (Figure 1.2b). Such microdroplets allow a large number of independent reactions to be monitored in parallel in volumes which are several orders of magnitude smaller than in conventional bulk assays [106–108]. The arising possibility to perform analysis at high throughputs has proven extremely valuable for analysing individual cells and detecting heterogeneities within cellular samples that are masked when the analysis is performed in bulk [83–91]. In addition to parallelised screening, volume confinement has been exploited to observe stochastic and often rare events, such as those taking part when proteins self-assemble in order to obtain statistic information on their occurrence [109, 110]. Indeed, self-assembly process is governed by a series of microscopic steps, which vary in relative importance between systems of different sizes, with the more dominant steps masking the rarer ones in non-compartmentalised bulk scale assays. The use of micron scale structures, however, opens up the possibility to track of such rarer events as well [111, 112].

1.5 Summary of the thesis

In this thesis, I discuss the development and application of new tools for probing the behaviour of proteins and protein interactions first *in vitro* and then inside cells using micron scale fabrication and flow engineering approaches.

The first half of the thesis focuses on *in vitro* analysis platforms. Specifically, in Chapter 3, I will discuss the development of a microfluidic device that facilitates high-throughput measurements on protein self-assembly in a label-free environment. I will outline and illustrate a series of advantages that this measurement strategy provides over conventional manual approaches. In Chapter 4, I will focus on the development of a rapid separation platform and demonstrate its application for separating and quantitatively characterising biomolecular species and their complexes. I will describe a series of technical and conceptual advances that led to the development of this platform and use the devices for detecting and visualising interactions between proteins and protein complexes. In Chapter 5, I will further demonstrate the possibility to combine this separation platform with direct on-chip analysis. These devices enabled me to obtain multidimensional data on biological mixtures and to characterise biological samples on resolutions not accessible by current state-of-the art in-solution analysis approaches.

I will proceed by describing the use of micron scale flow engineering approaches for understanding protein behaviour inside cells. In Chapter 6, I will describe a general-purpose strategy for detecting intracellular proteins inside single cells in a high-throughput manner.

Unlike previously described approaches, this platform offers significantly greater multiplexing extent than existing single cell protein analysis platforms. Finally, in Chapter 7, I will focus on a specific application of cellular biophysics. I will characterise cellular electrical responses and further develop solar panels that use biological photosynthetic organisms as catalysts.

Chapter 2

Materials and Methods

2.1 Preparation of microfluidic devices

2.1.1 Fabrication of replica master moulds

Singlelayer (SL) replica master moulds were fabricated through standard lithography approaches [103, 113] as illustrated in Figure 2.1. Briefly, a thin layer of SU-8 photoresist (MicroChem, Massachusetts USA) was spinned onto a three inch polished silicon wafer (MicroChemicals, Germany) using a spin-coater (Specialty Coating Systems, Indiana USA; Figure 2.1a). The grade of the photoresist (SU-8 3010, SU-8 3025, SU-8 3050) and the rotational speeds and times were varied according to the manufacturer's guidelines to achieve a desired feature height varying between 5 and 100 μm as outlined in the specific sections.

To selectively cross-link the photoresist in the areas were microfluidic channels were to appear, the wafer was exposed to custom-built UV-LED based apparatus [114] through an acetate transparency (Figure 2.1b). The structures on the transparency had been designed using AutoCAD software (Autodesk Education, California USA) and were printed by Micro Lithography Services Ltd, UK. All the uncross-linked photoresist was then removed by immersing the wafer in propylene glycol monomethyl ether acetate developer solution (PGME; Sigma, UK), followed by rinsing the wafer with isopropanol (IPA) and blow-drying it with pressurised nitrogen. This PGME development step (Figure 2.1c) resulted in the production of an inverse mould master with raised patterns corresponding to the channels in the final device (Figure 2.1d). The precise feature heights on the master were verified by profilometer (Dektak, Bruker) and were usually found to be within a 10% margin of the desired height. The master moulds were converted into patterned PDMS chips and ultimately, to microfluidic devices as described in Section 2.1.2.

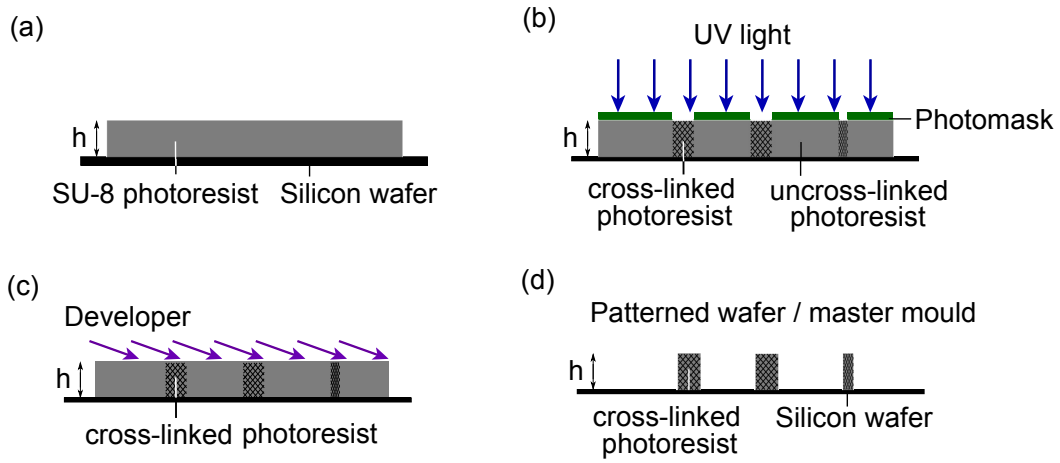

Fig. 2.1 Fabrication of master moulds for reproducible production of polymer-based microscale devices. **(a)** A thin layer ($5 - 100\mu$m) of photoresist is spinned onto a smooth silicon wafer and **(b)** covered with a photomask to expose selected areas of the wafer to UV-light and cross-link the photoresist in these areas. **(c)** The non cross-linked photoresist is then dissolved away in a developer solution **(d)** to yield a patterned wafer used as a master mould for reproducible production of microscale devices.

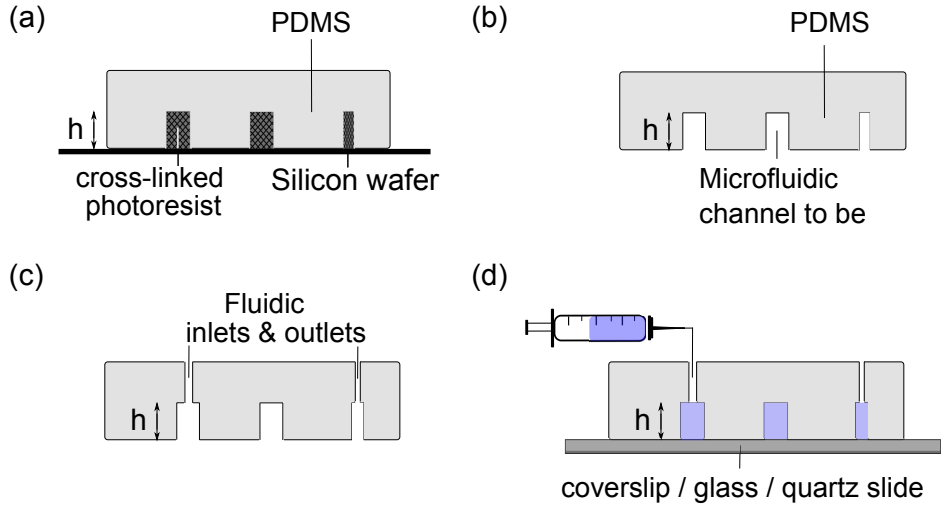

Fig. 2.2 Fabrication of PDMS microfluidic devices. **(a)** The replica mould (Figure 2.1) is casted in PDMS **(b)** to yield micropatterned PDMS surfaces. **(c)** Small sections of the PDMS are then punched off to introduce orifices for fluid inlets and outlets. **(d)** Finally, the patterned PDMS surfaces were irreversibly sealed with or glass (visible wavelength excitation) or a quartz (UV wavelength excitation) microscope slide or coverslip.

The fabrication of multilayer (ML) replica mould involved two subsequent UV-lithography steps each performed analogously to the singlelayer lithography process described in the previous section. After the first layer of structures had been developed, a new layer of SU-8 was spinned onto the wafer and exposed to UV light through a second lithography mask including the relevant structures. The alignment of the structures on this second mask with the already existing features was ensured with the inclusion of alignment markers on the edges of both of the masks. The features on the thinner layer were always produced first to minimise the obstructive effect on the formation of a uniform layer during the second photoresist spinning step. As for the SL mould, the heights of the structures on both of the layers were determined by a profilometer and were usually found to be within a 10% margin of the desired height.

2.1.2 Fabrication of 2D PDMS devices

To prepare polydimethylsiloxane (PDMS) microfluidic devices, single or multilayer replica moulds were casted in PDMS and cured, after which their surfaces were sealed to yield microscale channels (Figure 2.2). Specifically, PDMS elastomer and curing agent (Sylgard® 184, Dow Corning, Onecall, UK) were mixed in 10 : 1 ratio by weight, poured into the negative patterns of the master mould (Figure 2.2a) and cured for 90 minutes at 65°C, after any air bubbles had been removed in a desiccator. For experiments that involved fluorescent detection, 0.2% w/w, of carbon powder was included in the PDMS mixture to suppress the background fluorescence arising from the autofluorescence of PDMS.

After curing, the PDMS was removed from the master and orifices for fluidic ports introduced (Figure 2.2b-c) using a 0.75 mm biopsy puncher (World Precision Instruments, Florida USA). The patterned surfaces of the PDMS slabs were then cleaned by Scotch Magic™ Tape, following which the slabs were placed in a 50 mL Falcon tube containing IPA and sonicated in a water bath for 5 minutes to yield as clean surfaces as possible. The slabs were allowed to dry completely and bonded to either a glass (ThermoFisher Scientific or a quartz (Alfa Aesar) microscope slide or coverslip to yield closed channels (Figure 2.2d). The bonding was achieved by activating both the PDMS and the glass or the quartz surface with oxygen plasma (Electronic Diener Femto, 40% power for 15 seconds). Immediatelly prior to the experiments, the devices were exposed to an additional plasma oxidation step (80% power for 500 seconds) to form silanol groups on the PDMS surface and render channel surfaces more hydrophilic [115] and avoid protein or protein fibril samples adhering to the PDMS walls of the device.

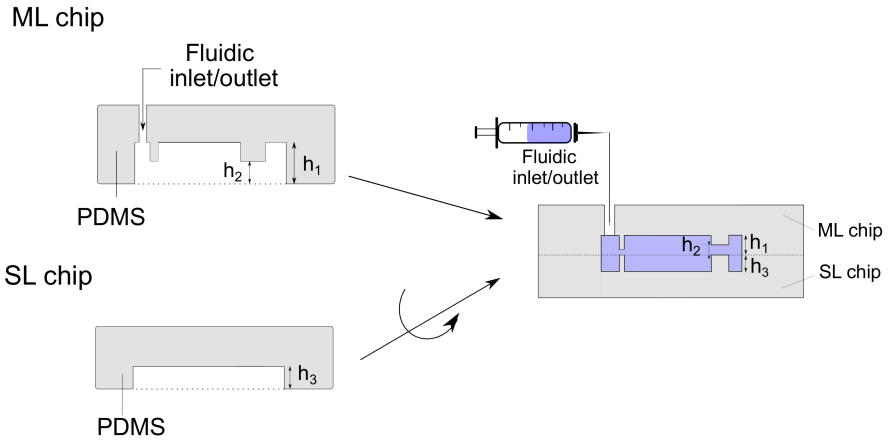

Fig. 2.3 Fabrication of 3D PDMS microfluidic devices. Two polymer slabs, one produced from a single layer and the other one from a multilayer replica mould are bonded together to yield 3D devices.

2.1.3 Fabrication of 3D PDMS devices

Three-dimensional (3D) PDMS devices were generated by plasma bonding two individual PDMS chips to each other (2.3). Specifically, one of the two chips involved the casting of a ML replica master and the other one a SL replica master in PDMS through the protocol described in Section 2.1.2. To achieve an alignment accuracy of the order of micrometers, water droplets were sprayed onto the patterned surfaces of the two chips after the surfaces had been activated by oxygen plasma. This procedure prevented their instantaneous sealing and allowed adjusting their relative positions under a stereomicroscope before a seal between the chips was formed. The aligned chips were then placed in an oven at 65 °C for one hour to allow the water to evaporate and the covalent bonding to take place. This procedure enabled producing injection orifices in the centre of the microfluidic channels as was desired for the devices used in Chapters 3 and 4.

2.1.4 Controlling fluid flow in microscale channels

Fluid flow into the devices was controlled using neMESYS syringe pumps (Cetoni GmbH). The solutions were injected using syringes (Hamilton™) that were connected to the microfluidic access ports using polyethylene tubing (Smiths Medical; 800/100/120) and 27-gauge needles.

Depending on the particular application, the flow in the devices was controlled either by injecting the fluids into the devices or alternatively, by placing fluid reservoirs to the device

inlets and withdrawing fluid from the device outlet. In the latter case, the flow rates of the fluids in the channels were determined by the hydraulic resistances of the channels, R_{HD}. Under the laminar flow conditions, fluid flow rate Q is linearly proportional to the applied pressure difference ΔP and inversely proportional to the hydraulic resistance R_{HD} of the channel

$$\Delta P = R_{HD} \cdot Q \tag{2.1}$$

This relationship allowed me to predict the flow rates in networks of microscale channels by applying requiring current balance and equipotentiality criteria at each node, similarly to how Kirchoff's Laws are used for predicting currents in a network of resistors.

2.2 Methods specific to protein self-assembly measurements

2.2.1 Microwell plate protein aggregation assays

Throughout the experiments, bovine insulin (Sera Laboratories GEM-700-112-P; used without further purification) was used as a model system and it was aggregated in 50 mM NaCl at pH 2.0 (adjusted with HCl) unless specified otherwise. In order to accelerate the aggregation process, 5% of the initial insulin was added in the form of pre-formed seeded fibrils with the rest of the protein being in its monomeric form. The pre-formed fibrils were generated by incubating 10 mg mL^{-1} insulin (pH 2.0, no NaCl) for 24 hours at 60 °C. Before adding the seeds to the aggregation mixture, they were sonicated (3 times for 5 minutes, Bandelin Sonopuls HD2070, 8 W, VS 70 probe) to fragment the fibrils and increase the number of free ends available for aggregation [116].

To track the aggregation process, Thioflavin T (ThT) was added to a final concentration of 30 μM either at the start of the aggregation process (*in situ* assays) or right before the fluorescence reading was taken (*ex situ* assays). In both cases the fluorescence intensities were recorded on a microplate reader (BMG LabTech, FLUOstar) using a 96 well half-area black bottom polystyrene plates (Corning, product #3881) with 100 μL sample in each well. The multiwell plate was sealed with an aluminum tape (Corning, product #6570) to reduce any evaporation of the fluid from the wells.

2.3 Methods specific to protein on-chip separation and analysis

2.3.1 Preparation of protein samples

Unless otherwise stated, the proteins were purchased from Sigma-Aldrich and used without further purification. The experiments were performed with the proteins dissolved in 10 mM sodium phosphate buffer at pH 7.4 and the buffer and protein solutions were filtered before performing the experiment (EMD Millipore^{TM}, 0.22 μm).

The recombinant Amyloid-β 1-42 with an N-terminal methionine (hereafter abbreviated as Aβ) was prepared by collaborators in the research group of prof. Sara Linse (Department of Biochemistry and Structural Biology, University of Lund, Sweden). Briefly, the protein was expressed in *Escherichia coli* from a PetSac plasmid [117] and the inclusion bodies dissolved in 8 M urea, 10 mM Tris/HCl, 1 mM EDTA buffer (pH 8.5). The Aβ protein was then isolated using ion exchange on diethylaminoethyl cellulose resin followed by two rounds of size exclusion purification in 20 mM sodium phosphate, 0.2 mM EDTA buffer (pH 8.5) using a Superdex 75 HR 26/600 column (GE Healthcare) and by one further round in 20 mM sodium phosphate, 0.2 mM EDTA buffer (pH 8.0) using a Superdex 75 HR 10/300 column (GE Healthcare). Before each round the peptide solution was lyophylised and dissolved in 6 M Guanidinium chloride (GuHCl), 20 mM sodium phosphate buffer (pH 8.5) as described previously [117, 118] .The final round of the purification process served to isolate the pure Aβ monomer and it was performed right before the protein was used for the experiments.

C-terminal pro-SPC Brichos (hereafter called Brichos) was similarly prepared by collaborators in the research group of prof. Sara Linse. In short, the protein was expressed in *Escherichia coli* cells with thioredoxin and His6 tags as previously described [119] with the plasmid being a gift from Jenny Presto and Jan Johansson, Karolinska Institute, Sweden. The inclusion bodies suspended in 2 M urea, 20 mM Tris, 0.5 M NaCl, 5 mM imidazole buffer (pH 8.0), following which the fusion protein was purified on a Ni^{2+}-loaded HiTrap Chelating HP column (GE Healthcare) and cleaved to release the thioredoxin and His6 tag, which was removed using the same chelating column. The Brichos protein was then further purified via ion exchange chromatography using salt gradient wash. The Brichos peak was collected and dialysed against 20 mM sodium phosphate buffer (pH 7.4) and equimolar amount of amine reactive Alexa488 (Life Technologies) added from a 5 mM stock dissolved in DMSO to label the Brichos. The solution was incubated at room temperature in dark for one hour and any unreacted dye was removed by gel filtration in 20 mM sodium phosphate, 0.2 mM EDTA (pH 8.0).

2.3.2 Label-free detection of proteins in the deep UV-wavelength range

Proteins were visualised in their unlabelled forms using a custom-built inverted deep-UV fluorescence microscope a described in detail in Ref.[114]. Briefly, the sample was illuminated using a 30 mW 280 nm LED (Thorlabs) exploiting the intrinsic fluorescence of aromatic residues of proteins in the deep-UV wavelength range. Briefly, the light was passed through an aspherical lens of a focal length of 20 mm to get a nearly collimated beam and after this onto a dichroic filter cube (280/20-25 nm excitation, 357/44-25 nm emission, 310 nm dichroic beamsplitter). The reflected light from the dichroic mirror was focused onto the sample by an infinity corrected UV objective lens (Thorlabs LMU-10X-UVB; numerical aperture of NA=0.25) and the emitted light collected through the same objective, passed through the emission filter and focused onto an EMCCD camera (Rolera EM-C2). All the used optics were made out of fused silica to enable high transmission in the UV wavelength region.

2.4 Methods specific to detecting proteins in individual cells

2.4.1 Preparation of DNA conjugated antibodies

The work described in Chapter 6, involved using protein kinase B as the protein target. The protein was detected using protein kinase B antibody pair (PKB; Abcam Human AKT1 Matched Antibody Pair Kit; #ab219528) with the capture antibody conjugated to a DNA sequence as described in this section and the biotinylated detector antibody conjugated to a streptavidin bead as described in Section 2.4.3.

The capture antibody to be conjugated to a DNA sequence was first exchanged from its storage buffer into a 100 mM pH 8.0 phosphate buffer using Zeba^{TM} 7K MWCO Spin Desalting Columns (#89882) following the manufacturer's guidelines. Specifically, the storage solution of the column was removed by spinning it at 1500 g for 1 minute, after which it was washed 3 times with 300 μL buffer similarly at 1500 g for 1 minute. To exchange the buffer, 100 μL of the antibody solution was placed on top of the resin bead and the fractionate collected after centrifuging for 1 minute at 1500 g. The antibody concentration after the buffer exchange was determined by absorbance at 280 nm (BMG LabTech, FLUOstar).

To initiate the conjugation reaction, 2 mg of DBCO-PEG5-NHS Ester (Click Chemistry Tools; #A102P-2) was dissolved in dimethyl sulfoxide (DMSO; Sigma-Aldrich; #D8418) to a final concentration of 100 μM and a fraction of it further diluted to 10 μM and distributed

into 7 μL aliquots. The buffer exchanged antibody was then reacted in 1:47 molar ratio with the DBCO-PEG5-NHS ester by mixing 94 μL of 13 μM antibody with 6 μL of 10 mM DBCO-PEG5-NHS Ester. The mixture was incubated at room temperature for 30 minutes, following which any unreacted DBCO-PEG5-NHS ester removed using the three Zeba^{TM} 7K MWCO columns each washed with PBS buffer as described in the previous paragraph. Finally, the DBCO activated antibody was reacted with an azide modified DNA (Integrated DNA Technologies; HLPC purified) in 1:4 molar ratio by mixing 50 μL of 10 μM antibody with 25 μL of 100 μM azide-DNA. The mixture was incubated overnight at 4°C.

To examine the extent of the conjugation reaction, the mixture was analysed on a NuPAGE^{TM} 4-12% Bis-Tris protein gels (ThermoFisher Scientific; # NP0322BOX) by loading around 2 μg of protein into each well and running it for 35 minutes at 180 V. The gel was stained with InstantBlue^{TM} (Coomassie) protein stain (Expedeon; #ISB1L).

2.4.2 Cell growth and barcoding the proteomic material

Human SH-SY5Y neuroblastoma cells (A.T.C.C.) were kindly cultured by Nina Kloss (Centre for Misfolding Diseases, Department of Chemistry, University of Cambridge) in Dulbecco's Modified Eagle Medium (DMEM) as described previously [120]. Before the experiments, the cells were centrifuged at 1000 rpm for 3 minutes and resuspended in PBS to yield a concentration of $4 \cdot 10^7$ cells mL^{-1} - this concentration was estimated to result in an average concentration of one cell per one microdroplet during their encapsulation into droplets.

The cells were mixed on-chip in 1:1 ratio with lysis buffer that also included barcoded capture antibodies for protein kinase B prepared as described in Section 2.4.1 and acrydite modified cell barcode DNA sequences(Table 6.1). Specifically, the lysis bufffer was prepared by mixing 300 μL of 20% Ficoll PM-400 (Sigma-Aldrich; #F5415), 10 μL of 20% Sarkosyl (Sigma-Aldich; N-Lauroylsarcosine sodium salt solution; #L7414), 40 μL of 0.5 M EDTA pH 8.0 (Sigma-Aldrich; #03690), 100 μL of 2 M Tris HCl pH 7.5, 100 μL of 2 M Tris HCl pH 7.5 and 50 μL of 1 M Dithiothreitol (DTT; ThermoFisher Scientific; #P2325). The protein kinase B (PKB) specific capture antibody was diluted into this lysis buffer at 2 μg mL^{-1} as suggested in the manufacturer's protocol and the cell barcode DNA to a concentration of 50 nM. The buffer was then diluted to 1 mL with deionised water.

The co-encapsulation was performed using a microfluidic chip with an on-chip mixing module (Figure 6.2a). The device was fabricated in PDMS to a height of 100 μm as described in Section 2.1.2. The flow rates of both the cells suspended in PBS and the lysis buffer with the barcoding sequences and barcoded antibodies were set to 150 μL h^{-1} and the flow rate

of the surfactant and the oil - 2% w/v FluoroSurfactant^{TM} (#008; Ran Biotechnologies) in FC-40 (Fluorinert^{TM}; 3M^{TM}) - to 800 μL h^{-1}. After a stable droplet formation had been established, 150 μL of the emulsion product was collected into a 200 μL PCR tube and left at 4° for 30 minutes for the cells to lyse and hybridisation between the two DNA strands to occur.

Following the cell lysis and barcoding in droplets, the emulsion droplets was de-emulsified by first removing the oil from the tube and then adding 2 μL of neat perfluorooctanol (PFO) per every 10 μL of emulsion. The contents were mixed thoroughly. After phase separation had established, any oil was removed and fresh PFO added. This process was repeated 3-5 times until no emulsion droplets were observed. Finally, the aqueous phase was carefully transferred into a clean PCR tube - only around the top 80% of the aqueous product was taken to ensure that it is completely free of oil.

2.4.3 Purification of the DNA library

To prepare antibody conjugated magnetic beads for purifying the DNA library, 50 μL of 10 mg mL^{-1} of the streptavidin coated M-280 Dynabead^{TM} suspension (ThermoFisher Scientific; #11205D) was mixed with 5 μL of 0.25 mg mL^{-1} of the biotinylated PKB detector antibody (Section 2.4.1), and diluted to 200 μL with PBS. The mixture was incubated at room temperature for 20 minutes under continuous stirring and washed four times with 200 μL PBS supplemented with 0.1% v/v bovine serum albumin (BSA). The washed product was dissolved in 200 μL of PBS.

To purify the de-emulsified product including both the DNA sequences of PKB bound and non-bound antibodies (Section 6.3.2), 20 μL of this mixture was mixed with 1.6 μL of the magnetic bead conjugated detector antibody stock solution to result a final concentration of 0.5 μg mL^{-1} of the detector antibody as suggested by the manufacturer. The mixture was left to incubate at room temperature for 30 minutes, and washed four times with 50 μL PBS supplemented with 0.1% v/v BSA and 0.01% v/v Tween® 20 (Sigma-Aldrich). The product was resuspended in 20 μL of PBS including 0.1% sodium dodecyl sulphate (SDS) and boiled at 95°C for 3 minutes to cleave the biotin streptavidin bond and release the DNA sequences from the magnetic beads.

2.4.4 Amplification of the DNA library

The PCR reaction was performed by mixing 10 μL of 2X Taq DNA Polymerase master mix (ThermoFisher Scientific; #K0171) with 0.5 μL of 10μM forward (Fwd) and reverse (Rev)

primers (Table 6.1) and 2 μL of the test sample, and diluted to 20 μL using deionised water. The PCR reaction mixture was amplified by first heating it to 95° for 2 mins for initial deannealing, then running 35 melting, primer annealing and extension cycles at 95°C (20 s), 62°C (30 s) and 68°C (30 s), respectively and finally, performing the final extension at 72°C for 3 mins. The amplification process was followed in real time using a QuantStudio 3 qPCR instrument (ThermoFisher Scientific).

2.5 Methods specific to measurements in biological photovoltaics

2.5.1 Culturing of the *Synechocystis* sp. PCC6803 cells

Wild-type *Synechocystis* sp. PCC6803 and its recombinant strains were routinely cultured in BG-11 medium (Gibco®) supplemented with 10 mM $NaHCO_3$ and maintained in sterile conditions at 30 $\pm$ 2 °C under continuous moderate light of 40 μmol photons m^{-2} s^{-1} and shaking at 160 rpm [121, 122]. Suspensions including higher cell concentrations were formed by centrifuging the original cell culture (5000 rpm for 3 minutes) and re-suspending the supernatant in fresh growth medium. The concentration of chlorophyll in cell cultures was determined spectrophotometrically from the optical density values at 680 nm and 750 nm as described previously [123]. Mutant strains of *Synechocystis* sp. PCC6803 were generated by Dr. David Lea-Smith (Department of Biochemistry, University of Cambridge) with the details on the experimental steps outlined in Appendix 1.

2.5.2 Integration of electronic components with the BPV

The anode of the device was fabricated as a long electrode spanning the full length of the device. For this purpose, an array of pillars was fabricated between the fluidic BPV chamber and the channel were the electrode was to appear. Such a design strategy allowed for the insertion of molten anode material (Indalloy 19 (51% In, 32.5% Bi, 16.5% In), Conro Electronics), which solidified upon removal from the hot-plate, yielding self-aligned electrode walls as has been previously described [124].

The cathode of the device comprised of a point electrode at the end of the channel. It was produced by inserting a strip of 100 μm diameter platinum wire (AlfaAesar) or platinum plated wire (GoodFellow) through polyethylene tubing (Smiths Medical; 800/100/120) sealed by an epoxy glue from both ends with approximately 1 mm metal left outside the tubing.

This allowed direct contact of the metal with the fluids flowing in the BPV when placing the cathode in the BPV via its designated access port. Copper wires were soldered to both the cathode and the anode, and alligator clamps were used to connect the electrodes to the potentiometer to characterise the performance of the device.

2.5.3 BPV operation and characterisation

The "charging unit" of the BPV was illuminated under red light (Maplin Strip RGB kit) with its intensity of the incident light measured using a quantum sensor uniformly detecting photosynthetically active radiation between 400 and 700 nm (Skye Instruments). The performance of the BPV system was characterised by applying a linear voltage sweep across the positive and negative terminals of the power delivery unit using a potentiostat (Autolab PGSTAT 12). After a stable terminal voltage value had been reached, the voltage was varied from 800 mV to 0 mV at a rate of 2 mV s^{-1} and the current output recorded at each voltage. The device was kept at 22 $\pm$ 2 °C throughout the characterisation process. In order to accurately characterise the biological power output the measurements were first performed in biologically non-loaded and then in biologically loaded form. All the power outputs were quoted as the difference between values describing the biologically loaded and non-loaded forms.

Chapter 3

Automated high throughput *ex situ* measurements on protein self-assembly

This chapter is based on the following publication:
Saar KL et al., Biophysical Journal, 110(3), 555-560, 2016.

3.1 Motivation

The process of protein self-assembly is of central importance for both normal [125] and aberrant biology [4–7], as well as for the development of novel materials for nanotechnology [126, 127, 111]. Specifically, it has been brought into connection with the onset of over a few dozen diseases, including those of rapidly increasing prevalence, such as the Alzheimer's and Parkinson's disorders and type II diabetes [4, 5, 128–130]. Despite the well established connection between the protein amyloid formation process and the onset of these diseases, the molecular mechanisms that underlie the onset of these conditions have been challenging to establish [128, 129, 131–135]. This difficulty has in part originated from the challenges associated with reliably probing the protein aggregation process *in vitro*.

One of the most frequently employed techniques for monitoring protein aggregation *in vitro* involves the use of extrinsic amyloidophilic probes. Upon binding to β-sheet rich fibrils, such dyes exhibit changes in their fluorescent spectra, which can be recorded externally with a spectrophotometer, thereby allowing the β-sheet rich amyloid aggregates to be detected and their amount to be quantified. However, many of the frequently used probes, such as Congo red or Thioflavin S, have a propensity to influence protein misfolding and aggregation processes and do not permit reliable extraction of quantitative information about the concentration of

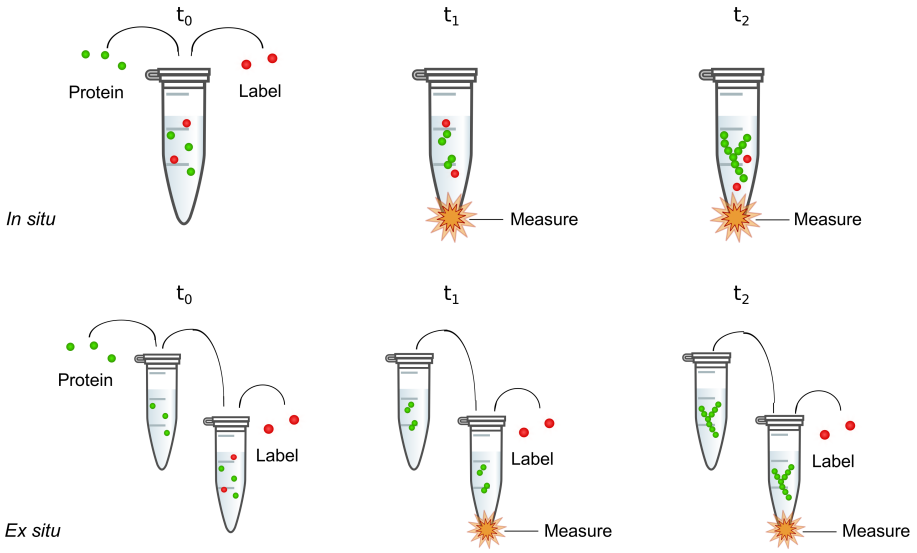

Fig. 3.1 *In situ* assays (top) are straightforward to perform but they require direct introduction of probe molecules into the assays. *Ex situ* assays (bottom), where at specific time points small samples of an aggregating protein solution are extracted and diluted into buffered dye, eliminate any undesired interference of the probe molecules on the aggregation process. However, conventional *ex situ* measurements are labour intensive to perform and perturb the reaction mixture.

aggregated material present [136–138]. Indeed, some very effective "beta-breaker" molecules that inhibit protein aggregation have structures that are modelled on amyloidophilic dyes [139–142]. Other probes, such as thioflavin T (ThT) have been suggested not to exhibit any or exhibit only minimal interference with the aggregation process [138, 143]. However, the exact mechanism of their binding to fibrils is still unclear [138, 142, 144] and conventional *in situ* assays (Figure 3.1, top) where the marker molecules are present throughout the reaction, commonly yield signals which are not directly proportional to the concentration of aggregates and are hence challenging to interpret in a quantitative manner [145, 146]. Moreover, the fluorescence properties of fluorescent probes, especially their quantum yields are affected by extrinsic conditions [136]. Therefore, since the readouts take place directly within the reaction medium, the measured signals are highly dependent on the surrounding environment, making it challenging to compare the aggregation process under different experimental conditions, such as the ionic strength or pH of the aggregation environment.

These drawbacks can be effectively eliminated through the use of an *ex situ* measurement strategy, where the probe molecules are not brought into contact with the reaction mixture but rather with aliquots taken from the aggregation sample (Figure 3.1, bottom), thus avoiding any interaction between the aggregating protein and the dye. In addition to allowing

extracting quantitative information about the amount of aggregates present, the reaction and measurement steps are spatially separated and chemically decoupled, making comparison between aggregation reactions that take place in different environmental conditions possible.

Despite their advantages, *ex situ* measurement strategies possess different drawbacks which have limited their widespread adoption: they are laborious to perform as every time point requires manual intervention and the reaction can be followed only at a limited number of time points. Furthermore, the requirement to physically separate aliquots from the reaction mixture implies the use of large physical volumes for the aggregating protein solution. Last but not least, withdrawing aliquots often results in agitation of the reaction mixture and can have a significant effect on the aggregation process if the process is to be studied under quiescent conditions. In the experiments described in this chapter, I address the limitations of conventional *ex situ* measurements and design and demonstrate devices that eliminate the need for physical aliquot extraction and instead allow for *ex situ* aggregation measurements to be performed in an automated and high throughput manner.

3.2 An automated high throughput *ex situ* measurement strategy

I set out to design and fabricate devices that would automate the manual aliquot taking process implicated in conventional *ex situ* measurements yet retain all of its advantages - most notably, the spatial separation and the resulting chemical decoupling of the aggregation process and the fluorescent measurement - while offering additional benefits of eliminating the need for manual aliquot taking, allowing tight control over the reaction time of the dye with the aggregate species, avoiding agitation of the aggregation mixture and providing the capability to follow the aggregation process in real time.

My devised design involved a two inlet system (Figure 3.2) where a label-free aggregating protein sample (marked green) and buffered dye are continuously transferred to a measurement system. Upon entry into the mixing and labelling area (marked yellow), the buffered dye mixed with the protein sample. The time period that it took for the fluids to move between the point where the protein and the dye first met and where the fluorescence readings were recorded was short (seconds) compared to that of most protein self-assembly processes (hours). Hence, effectively no further aggregation occurred in the presence of the probe molecules. Moreover, the residence time, t_{res}, between the points where the two streams of fluids first met and where the fluorescence was recorded was designed to be longer than the time needed for the ThT molecules to diffuse into the central protein stream. Specifically, the time and

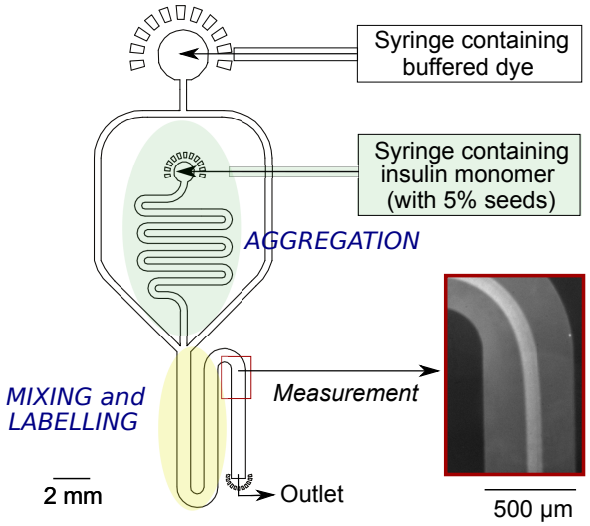

Fig. 3.2 Device architecture for performing *ex situ* measurements on chip. When the aggregating protein and the buffered dye streams mix, the probe molecules can start diffusing into the protein stream and bind the protein fibrils. Inset: the measurement is taken sufficiently downstream for all the protein stream to have become labelled.

diffused distance, x_{diff}, were related by the approximate relation

$$t_{res} = \frac{x_{diff}}{2D_{ThT}} \tag{3.1}$$

and the diffusion coefficient, D, for ThT estimated from its hydrodynamic radius, R_H, using the Stokes-Einstein relation

$$D = \frac{kT}{6\pi\eta R_H}, \tag{3.2}$$

where k is the Boltzmann constant, T is the temperature and η is the viscosity of the solution.

In the following chapters I show that this proposed strategy underlies a significant improvement in terms of data throughput compared to manual *ex situ* assays, allowing hundreds of individual measurements to be performed in real time and on a single aggregating protein system.

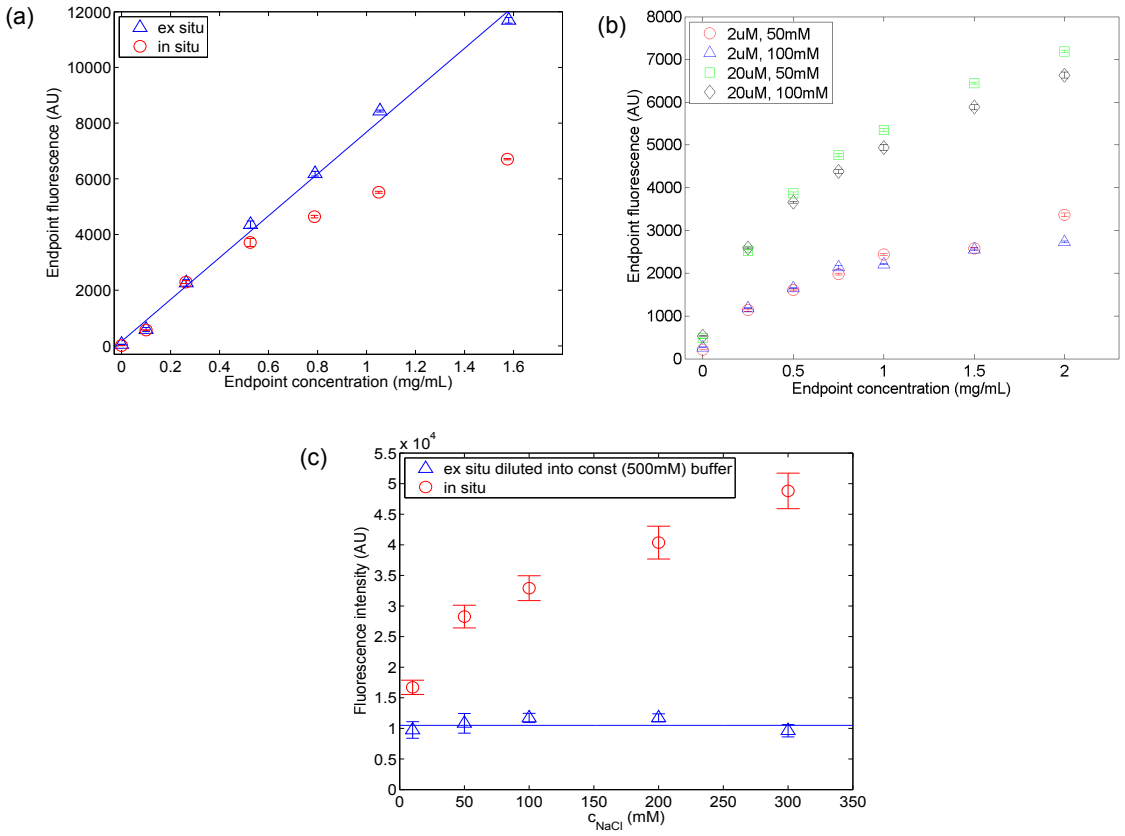

Fig. 3.3 Advantages of *ex situ* aggregation assays over *in situ* assays. **(a)** As opposed to *in situ* aggregation assays (red circles), the fluorescence intensity in *ex situ* assays (blue triangles) scales linearly with the aggregate concentration ($R^2 = 0.997$). The data points correspond to fluorescence signal at the aggregation end-point with the aggregation occurring at pH 2.0 and NaCl concentration of 50 mM. **(b)** A similar non-linear scaling between the end-point fluorescence intensity and the insulin fibril concentration was observed in *in situ* assays in different aggregation environments (50 mM and 100 mM NaCl, both at pH 2.0) and ThT concentrations (2 μM and 20 μM). **(c)** When studying *ex situ* aggregation assays in a standard buffer (500 mM NaCl), any effect from the aggregation buffer can be eliminated (blue triangles). Such spatial and chemical decoupling is not possible in *in situ* assays (red circles). All the data shown are an average of n = 3 repeats with the error bars corresponding to standard deviations.

3.3 Results

3.3.1 Microplate reader assays

I first evaluated the performance of *in situ* and *ex situ* assays in bulk scale experiments. To this effect, a series of different concentrations of insulin was left to aggregate for 12 hours following seeding the reaction (Materials and Methods, Section 2.2.1). The end-point fluorescence intensity at all the concentrations for both *in situ* and *ex situ* assays were recorded and are shown in Figure 3.3a. The *ex situ* assays were observed to exhibit a linear scaling of the end-point fluorescence intensity with the insulin concentration across the full range of the protein concentrations analysed (blue triangles); by contrast, such simple linear scaling was not detected in the *in situ* assays (red circles). I also examined the *in situ* aggregation process of insulin in different reaction environments (50 mM and 100 mM NaCl, both at pH 2.0) and dye concentrations (2 μM and 20 μM ThT) and noted that the lack of such a scaling relationship is a more general trend occurring across all these environments (Figure 3.3b). A similar absence of linear scaling between the end-point fluorescence and the fibril concentration has been observed for other protein systems [145, 146], indicating that ThT *in situ* assays are in general only semi-quantitative. As ThT molecules are known to specifically bind to β-sheet structures [142], I hypothesise that the different trend between the fluorescence intensity and the protein endpoint concentration for *in situ* and *ex situ* assays originates from the ThT molecules binding to the formed protein aggregates already over the course of the *in situ* assays, thereby resulting in a different morphology and, hence, ThT sensitivity of the formed fibrils.

To examine the effect of the aggregation environment on the end-point fluorescence intensity, I followed the aggregation of a pre-set concentration of insulin (0.5 mg mL^{-1}) in aggregation buffers of varying ionic strengths (20 mM to 300 mM NaCl) with (*in situ*) and without (*ex situ*) the inclusion of ThT in aggregation medium. For the *in situ* assays the end-point fluorescence was recorded directly in the aggregation environment, whereas the *ex situ* assays were monitored by withdrawing samples and diluting these into a set measurements solution. Specifically, a 1:10 dilution into a 500 mM NaCl (pH 2) was chosen for the salt that was present in the original aggregation solution not to affect the recorded fluorescence values. I observed that in the *in situ* assays the presence of salt had a marked effect on the observed fluorescent signal (Figure 3.3c, red circles), making a connection between the observed fluorescence and the concentration of aggregated protein challenging to establish. By contrast, in the *ex situ* assay, the recorded fluorescence intensities were independent of the salt concentration in the aggregation medium (blue circles), since the measurement was always taken under set conditions. These data illustrate that *ex situ* assays open up the

possibility to compare the extent of aggregation under different reaction conditions.

3.3.2 Automated *ex situ* assays in 2D microfluidic devices

The data in Figure 3.3 highlight the robustness of *ex situ* assays under varying solution conditions compared to *in situ* strategies. However, the use of such *ex situ* analysis methods in a conventional laboratory has been limited because the measurement process is slow, labour intensive and requires large volumes of the aggregating protein mixture in order to allow for a number of aliquots with macroscopic volumes to be extracted. Furthermore, extracting aliquots perturb the aggregating sample, making it virtually impossible to reliably analyse aggregation processes if quiescent conditions are required.

To overcome these limitations of conventional *ex situ* measurements, I devised and fabricated microfluidic devices that enable *ex situ* measurements to be performed in an automated and a high-throughput manner (Section 3.2). Specifically, pre-seeded insulin and ThT (30 μM) solutions were injected into the device at flow rates of 50 μL h^{-1} and 200 μL h^{-1}, respectively, and the ThT fluorescence was monitored in the "mixing and labelling" area (Figure 3.2). Under these conditions, for the ThT molecules to mix with the aggregating protein sample, the former have to diffuse by

$$\mathrm{x_{diff}} = \frac{1}{2} \cdot \mathrm{w_{protein}} = \frac{1}{2} \cdot \mathrm{w_{total}} \cdot \frac{\mathrm{Q_{protein}}}{\mathrm{Q_{total}}} = 0.5 \cdot 400\mu\mathrm{m} \cdot \frac{50\ \mu\mathrm{L\ h^{-1}}}{(200+50)\ \mu\mathrm{L\ h^{-1}}} = 40\ \mu\mathrm{m}, \quad (3.3)$$

where the factor $\frac{1}{2}$ arises from symmetry of the device, w_{total} and $w_{protein}$ are the total width of the microfluidic channel and that of the protein beam, respectively, and $\mathrm{Q_{total}}$ and $\mathrm{Q_{protein}}$ are the respective flow rates.

Using equation 3.1, this mixing process can be estimated to take around

$$\mathrm{t_{ThT}} \sim \left(\frac{\mathrm{x_{diff}^2}}{2\ \mathrm{D_{ThT}}}\right) \sim \left(\frac{\left(40 \cdot 10^{-6}\right)^2\ m^2}{2 \cdot 8 \cdot 10^{-10}\ m^2\ s^{-1}}\right) \sim 1\ \mathrm{s} \quad (3.4)$$

Additionally, in a rectangular channel the centreline velocity of the fluid can be approximated as

$$\mathrm{u} = \frac{\mathrm{Q_{total}}}{\mathrm{wh}} = \frac{\frac{250\ \mathrm{mm^3}}{\mathrm{h}} \times \frac{1\ \mathrm{h}}{3600\ \mathrm{s}}}{400 \cdot 10^{-3}\ \mathrm{mm} \cdot 100 \cdot 10^{-3}\ \mathrm{mm}} = 1.7\ \mathrm{mm\ s^{-1}} \quad (3.5)$$

In my designed device, the measurement was taken around 14 mm downstream of the point where the fluids first mixed, corresponding to a well-defined location where the mixing

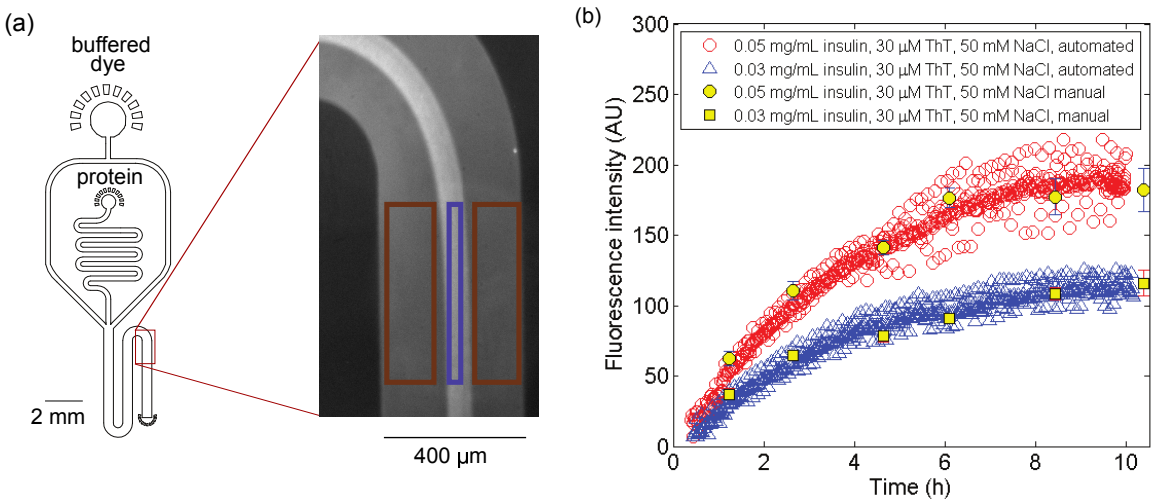

Fig. 3.4 **(a)** The fluorescence intensity at each time point was calculated as the difference between the fibril-bound form of the ThT at the centre of the channel (inset, blue rectangle) and its unbound form at the edges of the channel (the average of the two brown rectangles). Both values were averaged across rectangular shapes to eliminate variations from potential non-uniform illumination of the imaging area. **(b)** Seeded *ex situ* aggregation assays at 0.03 mg mL^{-1} (blue triangles) and 0.05 mg mL^{-1} insulin (red circles) using the microfluidic device in Fig. 3.2. The data agree with the curves obtained through manual aliquoting (yellow circles and squares).

channel curved (Figure 3.4) and by which the ThT molecules and the fibrils had mixed fully (Figure 3.4, inset).

Figure 3.4b shows the seeded *ex situ* aggregation curves obtained at protein concentrations of 0.03 mg mL^{-1} (blue triangles) and 0.05 mg mL^{-1} (red circles). The curves were obtained by recording the fluorescence intensity in the measurement area (Figure 3.4a) at 60 second time intervals. At each time point, the fluorescent reading was estimated as the difference between the intensity of the aggregate-bound ThT in the centre of the microfluidic channel and that of the unbound ThT at the edges of the channel. Both values were averaged across rectangular shapes in order to eliminate any variations from potential non-uniform illumination of the imaging area. From the acquired data I observed that the fluorescence signal at long times when the aggregation process had reached completion was proportional to the initial monomer concentrations, as expected for *ex situ* measurement (113 ± 6 AU and 192 ± 11 AU for 0.03 mg mL^{-1} and 0.05 mg mL^{-1}, respectively; average of $n = 30$ final values). The observed two-level fluctuations in the data are likely to have arisen from pulsation of the flow.

To validate these results, the obtained aggregation curves were compared to the data acquired when the process was studied using conventional manual *ex situ* approaches. Specifically, these experiments involved preparing a number of separate aggregation assays and detecting the presence of fibrils at selected time points of interest using a new parallel assay every time. The ThT was added to a final concentration of 30 μM and the fluorescence intensity was recorded on a microplate reader right after the probe molecules had been introduced. I found that the aggregation curves obtained on the microfluidic platform agreed well with the manual assays (Figure 3.4b).

3.3.3 Automated *ex situ* assays in 3D microfluidic devices

The 2D device could be effectively used for following protein aggregation at low protein concentrations. However, at higher concentrations, adhesion of protein fibrils to the PDMS surface was observed. For instance, the bottom inset of Figure 3.5a shows the adhesion of protein fibrils to the PDMS walls of the microfluidic device (green circles) at a concentration of 0.2 mg mL^{-1} after 2 hours. In order to follow the aggregation process accurately at higher concentrations, three-dimensional (3D) devices were built that allowed the sample aliquot stream to be flanked by co-flowing labelling solution in all directions (Figure 3.5a, top inset), thus preventing direct contact between protein and the walls of the microfluidic channel where adhesion could otherwise occur. Such 3D devices were fabricated by bonding two plasma activated PDMS polymers slabs to one another with one formed through a single layer photolithography process and the other one through two subsequent photolithography steps as described in detail in Materials and Methods (Section 2.1.3) . The channels through which the buffered dye entered the device as well as the "mixing and labelling area" (Figure 3.2) were fabricated onto both microfluidic chips so that they spanned across the height of the device. The protein channel, however, was fabricated only onto the thinner layer of the ML replica master, so that it would form the middle layer of the 3D device and would enter the centre of the "mixing and labelling area" .

Using such 3D device a seeded aggregation curve at insulin concentration of 0.2 mg mL^{-1} was obtained (Figure 3.5b) to illustrate that the device opens up the possibility to study aggregation at higher protein concentrations. As for the lower concentrations, the data was seen to agree with manually performed *ex situ* where ThT molecules were introduced into separate aliquots at various time points right before the measurement was taken. Moreover, when normalising the three aggregation curves (0.03 mg mL^{-1} and 0.05 mg mL^{-1} in the 2D devices and 0.2 mg mL^{-1} in the 3D device) with respect to the intensity at long times (the average of $n = 30$ final values) all the three curves were seen to a good approximation collapse onto a master curve, as expected for first order kinetics observed under fully seeded

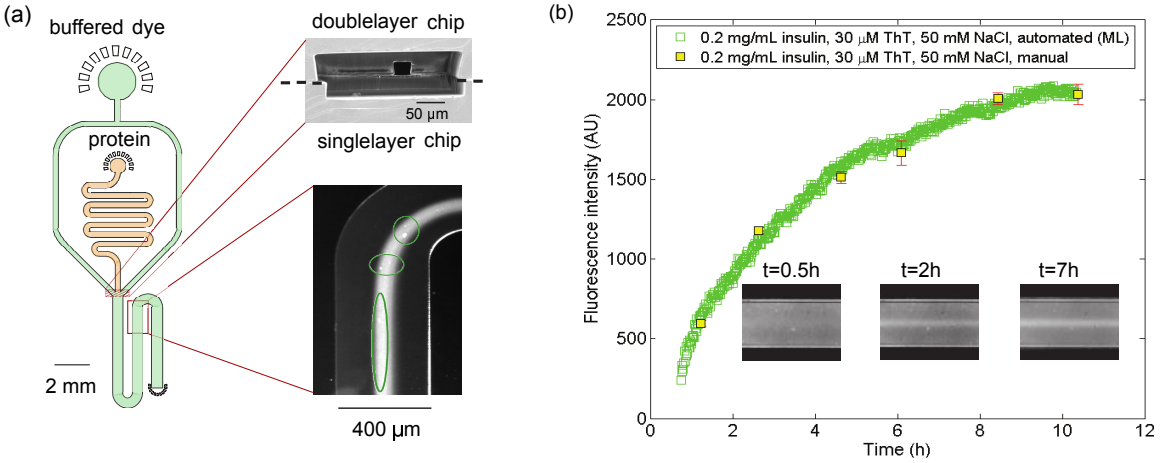

Fig. 3.5 **(a)** At higher protein concentrations fibrils were observed to adhere to the PDMS walls of the device - bottom inset: the measurement area after 2 hours at protein concentration of 0.2 mg mL^{-1}. To monitor the aggregation at higher protein concentrations, I fabricated devices where the protein sample was flanked by co-flowing buffer in all directions, which I achieved by bonding together a single layer chip including the channel for the buffered dye and for the mixing and measurement area (green) and a multilayer chip which included these same areas on its taller layer and only the protein inlet channel (orange) on its thinner layer. Top inset: SEM image of the nozzle of such 3D device. **(b)** Seeded aggregation curve of 0.2 mg mL^{-1} insulin using manual aliquoting (yellow squares) and the 3D microfluidic device (green squares).

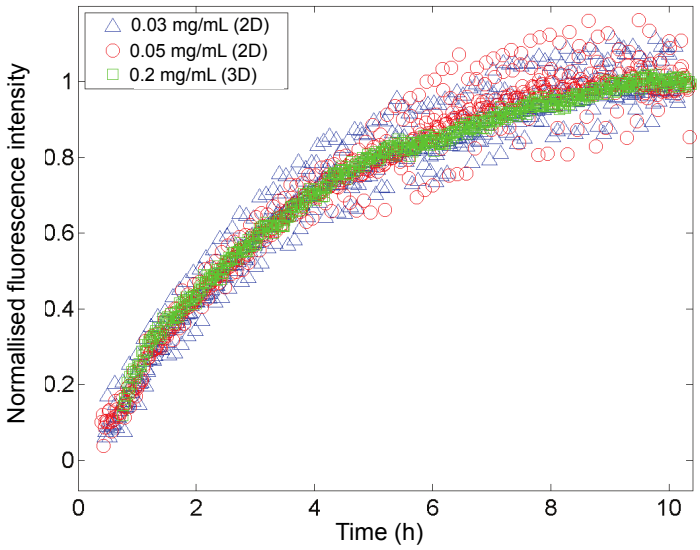

Fig. 3.6 When normalised with respect to the average of the $n = 30$ final values, the three aggregation curves - 0.03 mg mL^{-1} (blue triangles) and 0.05 mg mL^{-1} (red circles) in the 2D devices and 0.2 mg mL^{-1} (green squares) in the 3D device - were seen to collapse onto a single master curve as expected for a fully seeded aggregation process.

conditions [147, 148].

3.4 Discussion

The microfluidic devices demonstrated in Chapters 3.3.2 and 3.3.3 have a number of advantages over conventional methods of following protein aggregation reaction. Most importantly, spatial separation ensures that the aggregation reaction is decoupled from the measurement process, hence eliminating interference between the probe and the aggregating protein of the type that is encountered in *in situ* assays.

In addition to providing spatial separation between the two processes, the devices allow the aggregation reaction and the measurement step to be performed in chemically different environments. Thus, for example, a different buffer, such as one with higher ionic strength, could be used to prepare the ThT solution in order to amplify the fluorescence signal [149] but leaving the environment of the aggregation unaffected; the latter process could still take place in a buffer with lower ionic strength. Furthermore, when a set measurement buffer is used, comparison between aggregation reactions happening in different environments becomes

possible as illustrated in Figure 3.3c (blue triangles).

The acquisition of *ca* 600 data points over a time period of 10 hours is more than an order of magnitude improvement over manually performed *ex situ* measurements of protein aggregation where the time resolution is usually of the order of tens of minutes as defined by the normal aliquoting of a reaction cycle [150–153]. Moreover, as the process of transferring the protein sample into the measurement system is continuous, fluid handling is no longer the limitation of the achieved time resolution. Instead, it is the detection system that determines the frequency of measurements. Therefore, the strategy outlined here opens the possibility to study processes which exhibit fast kinetics and can be challenging to follow by manual aliquot taking.

A further key feature of these assays is that the small scale of microfluidic devices combined with the lack of the requirement to physically separate macroscopic aliquots enables only miniature volumes of protein solution to be used. More specifically, the 2D devices consumed *ca* 500 μL of protein sample to obtain the full *ex situ* aggregation curve. As the high protein flow rate is a necessary requirement to eliminate adhering of protein fibrils to the PDMS walls, these simpler devices are best suited for experiments which are less sensitive towards sample consumption. The 3D devices, however, are not restricted to the use of specific flow rates as any interaction between the PDMS walls of the device and the protein is eliminated due to three-dimensional flow. Specifically, in this work, *ca* 75 μL of protein sample (includes a 25 μL dead volume connecting the syringe to the microfluidic device, this could be reduced further) was sufficient to acquire the full *ex situ* aggregation curve (600 data points over 10 hours; 120 nL of sample per measurement point). The flow rate can be decreased further until the precision of the syringe pumps is reached. Which of the two types of devices is more appropriate for a particular experiment is a compromise between a multi-step fabrication technique and the amount of protein sample consumed.

In addition to this, if following the aggregation process at high time resolution or continuously is not of relevance, the syringe pump could be operated under a flow ramp with the protein sample ejected only at the time when a measurement is to be taken or alternatively, control valves could be integrated with the design [154, 155], decreasing the protein consumption even further. This reduction could be particularly relevant for non-seeded aggregation assays where high time resolution is more beneficial during some stages of the process than others. This approach is applicable to both the 2D and the 3D devices.

Unlike conventional *ex situ* assays, this microfluidic setup does not rely on user interactions to physically extract aliquots from the aggregation mixture, thus reducing the risk of perturbing the sample and affecting the aggregation process. This is especially of import if fully quiescent

aggregation conditions are required.

Last but not least, it is worth noting that the design strategy that this device uses can be extended to other types of measurements where interference with probe molecules is not desirable.

3.5 Conclusion and further developments

Conventional *ex situ* measurements yield high quality data but are labour intensive to perform, can disturb the reaction mixture and allow reactions to be monitored only at limited numbers of time points rather than continuously. To address these limitations, I devised, built and demonstrated microfluidic devices that eliminate fluid aliquoting as the limiting factor on the possible time resolution and instead allow continuous, real time and automated measurements of protein aggregation assays, thereby offering a unique combination of monitoring the aggregation process in a label free and in a high throughput manner. The use of these devices could be extended to other measurement systems where avoiding interference between the process and the measurement probes is desirable.

Chapter 4

New approaches for protein separation under native conditions

This Chapter is based on the following publications and a patent application:
*Saar KL and Zhang Y et al., Lab on a Chip, 18**(1)**, 162-170, 2018*
*Saar KL et al., Analytical Chemistry, 90**(15)**, 8998-9005, 2018*
Saar KL and Müller T and Knowles TPJ. GB1720627.7. Filed (2017) and licensed (2018)

4.1 Motivation

Whereas the experiments described in Chapter 3 offer the possibility to monitor the protein aggregation process in a label free environment and a precisely controlled automated high throughput manner, in these devices performed the detection on the scale of the full assay, only yielding information on the total amount of protein aggregates present. Aggregating mixtures are known to be highly heterogeneous with differently sized aggregates exhibiting a different level of toxicity. In the following two Chapters, I aim to develop separation approaches that would be suitable for biomolecular separation and for yielding size resolved data on the aggregation process, in addition to the time resolved information described previously.

When separating molecules according to specific biophysical or biochemical properties, common platforms employ matrices to oppose chaotic molecular movement and keep identical molecules in distinct bands. The integration of such matrices, however, severely limits the speeds at which molecules can be fractionated with even the simplest one-dimensional processes lasting for over an hour, a timescale that is poorly compatible with the dynamic nature of many biological phenomena. Moreover, the involvement of matrices can affect the relative strength of biomolecular interactions and result in preferential disassembly of selected

complexes. Last but not least, their use prevents examining samples that exhibit significant size variations, such as heterogeneous and self-assembled systems, as the larger molecules present in such mixtures can obstruct the matrix pores.

A fundamentally different approach to controlling molecular movement and keeping molecules of similar sizes together involves scaling down the compartment in which the process occurs. As outlined in the Introduction of this thesis, in micron scale channels fluid flow is confined to laminar layers with any molecular movement between the layers restricted to controllable diffusion. Hence, if appropriately designed, micron scale separation systems can remove the reliance on matrices integral to traditional separation platforms. Moreover, not only would such micron scale separation systems decrease sample consumption and increase the recovery rate in comparison to conventional matrix-based approaches, they would also allow molecules to move through the separation area much faster, thereby enabling a second or a subminute rather than an hour timescale operation. In this Chapter, I present a strategy for designing such miniature separation systems and address two critical challenges associated with their engineering, namely the effective integration of strong and stable electric fields as described in publication [156], and increasing the resolution limit of the process based on the invention described in patent application [157] and in publication [158].

4.2 Integration of electric fields with micron scale channels

The traditional route to functionalising micron scale channels with electric fields involves the incorporation of metal electrodes [159–163]. The generation of electrolysis products at the electrode/liquid interface, however, imposes severe limitations on the stabilities of the systems that exploit this strategy, especially when the separation is to be performed in conductive media, such as biological aqueous buffers. Indeed, the prime concern in this context is the formation of gaseous products on the electrode surface: the generated bubbles do not only disturb the flow, leading to unstable separation, they also influence the strength of the field, making quantitative characterisation challenging.

I first set out to estimate the required field strengths for performing biomolecular separation. To achieve separation, molecules have to deflect to at least as far as the sample beam broadens when moving down the electrophoresis chamber as a result of diffusion (Figure 4.1b):

$$\frac{x_{def}}{2x_{diffusion}} = \frac{v_{drift} \cdot t_{res}}{\sqrt{2Dt_{res}}} = \frac{\mu \cdot E \cdot t_{res}}{\sqrt{2Dt_{res}}} = \frac{\mu_{el}}{\sqrt{2D}} \cdot E \cdot t_{res} > 1, \tag{4.1}$$

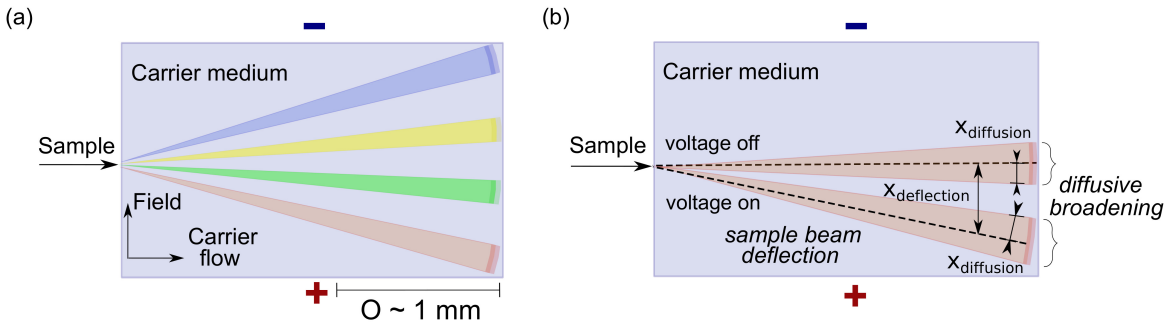

Fig. 4.1 **(a)** Micron scale free flow electrophoresis (μ-FFE) involves the continuous separation of molecules when they flow in a carrier medium and are subjected to a perpendicularly applied electric field. This approach allows for continuous biomolecular separation and its integration with relevant downstream processes. **(b)** While moving down the electric field, the sample beam broadens due to the diffusive movement of molecules. For effective separation the deflected distance, $x_{deflection}$, has to exceed the diffused distance, $x_{diffusion}$.

where v_{drift} is the velocity at which the analyte of electrophoretic mobility, μ_{el} and diffusion coefficient D, moves in electric field of strength E, and t_{res} is the residence time of the analyte molecule in the separation chamber.

Remarkably, the application of such fields in micron scale channels leads to the formation of very noticeable amount of gaseous products. Indeed, for a representative protein molecule with $D = 10^{-10}$ m^2 s^{-1} ($R_h = 3$ nm) and $\mu_{el} = 10^{-8}$ m^2 s^{-1} V^{-1} (a protein with isoelectric point in the range of 4-6 under physiological pH - around a third of the proteins in the human proteome are predicted to have their isoelectric point values in that range [164, 165]), I can estimate from equation 4.1 that separation on a second scale time scale - which is required for molecules to move through micron scale channels - can be achieved at electric field strengths above $E > 20$ V cm^{-1}.

I can relate this electric field strength E and the amount of charge generated in a medium of conductivity κ over a cross-sectional area A over time t through

$$q = I \cdot t = (E \cdot \kappa \cdot A) \cdot t = (E \cdot \kappa \cdot L \cdot h) \cdot t \tag{4.2}$$

where I is the current flowing in the separation area and L and h are its length and the height, respectively. This amount of charge corresponds to the generation of about

$$V_{gases} \sim \frac{RT}{p}\frac{q}{F} = \frac{RT}{p}\frac{(E \cdot \kappa \cdot L \cdot h) \cdot t}{F}, \tag{4.3}$$

gaseous products, where F is the Faraday constant, R is the ideal gas constant and T and p are the temperature and pressure, respectively.

Finally, I can estimate the ratio of the volume of the generated gases and the volume of the microfluidic chip to be

$$\frac{V_{gases}}{V_{chip}} = \frac{RT}{p}\frac{(E\kappa \cdot L \cdot h) \cdot t}{F}\frac{1}{w \cdot h \cdot L} = \frac{RT}{p}\frac{E\kappa}{Fw}t, \tag{4.4}$$

From equation 4.4 I obtain that when an electric field of $E = 20\ V\ cm^{-1}$, as was estimated to be the minimum strength required for the effective separation of representative protein molecules as per equation 4.1), is applied, for instance, over $t = 1$ min time scale in a $w = 2$ mm wide separation channel, the volume of gases generated is around equal to the volume of the separation chamber itself even when only low conductivity buffers ($\kappa = 0.02\ \Omega^{-1}m^{-1}$ corresponding to e.g. 10 mM phosphate buffer) are used. This result indicates that in order to apply electric fields of the strength that enable separating protein molecules over the time scales needed for most operations, effective strategies for either continuously removing the generated gases or barriers for preventing them from entering the separation area are required.

To address this issue, conventional macroscopic separation setups introduce ion-permeable barriers between the electrodes and the separation chamber, preventing the gaseous products from interfering with the separation process [166, 167]. Several approaches have been presented to similarly use physical structures for reducing the detrimental effects of electrolysis products in micron scale separation platforms, such as physically separating the analysis chamber from the electrodes by membranes [168–173] or by (partial) partitions [159, 167, 174, 175]. Alternatively, redox electron carriers have been used to suppress the formation and build-up of gas bubbles [166]. Despite addressing the concerns related to the formation of gaseous electrolysis products, these approaches introduce different limitations, such as significant restriction on the applicable field strengths, intricate fabrication procedure, or both. Moreover, displacing gas bubbles does not overcome the issues that the presence of dissolved electrolysis products creates, such as local changes in pH [167]. Finally, external electrodes have been used to facilitate device fabrication alleviating the risk of gases being introduced onto chip [176–178], but their placement at both inlets and outlets at the same time can still result in electrolysis products and heat flowing through the device.

Due to these difficulties, current studies usually limit the applied fields to small values where the rate of generating electrolysis products is low [166, 124, 81, 179, 180]. However, efficient separation for more general purposes is possible only in the presence of strong electric fields where the deflection of the analyte molecules in response to the field exceeds their

diffusion over the same time [181, 182]. In this section I present a strategy for overcoming the aforedescribed limitations and demonstrate a micron scale separation device that actively transports away both gaseous and non-gaseous electrolysis products before they enter the separation chamber, thereby facilitating the application of strong and stable electric fields also in aqueous biological buffers. Notably, the device can be fabricated in a straightforward manner via a single layer lithography process and without involving alignment steps between fluidic and metallic components as has conventionally been the requirement for micron scale separation systems. The device design strategy and the results are based on a published article [156].

4.2.1 Device design and operation

To facilitate the application of strong electric fields carrying high conductive currents, I devised and implemented a strategy where the electric potential was applied outside the chip and a highly conductive solution (3M KCl) used to simultaneously achieve two goals: (i) actively transport all generated electrolysis products away before they come into contact with the micron scale channels and the separation area and (ii) facilitate the propagation of the electric field back into the device in the direction opposite to the flow (Figure 4.2a-b).

Specifically, the device contained three wide parallel channels connected by narrow perpendicular channels (Figure 4.2a) and it was fabricated in poly(dimethylsiloxane) via standard soft photolithography approaches with the structures sealed by quartz slides (Materials and Methods, Section 2.1.2). The separation process occurred in the middle channel, which included the analyte stream that was flanked by co-flowing carrier medium from both sides. The two side channels contained the conductive electrolyte solution that transmitted the electric field upstream to the electrophoresis area. The connecting channels between the three main channels were designed to have a large hydrodynamic resistance to minimise mass transfer of the electrolyte solution to the central electrophoresis area. They were further designed to have meandering shapes such that the overall area of the device and hence the variations in the height across its cross-section would be minimised. The flow out from the separation channel was split towards two separate outlets - this prevented the positive and negative liquid electrodes coming into close contact with one another and short-circuiting the system.

The flow of the solutions to the device was controlled by syringe pumps (Materials and Methods, Section 2.1.4) and set to 280 μL h^{-1} with the injection rate of the carrier medium being 19 times higher than that of the protein, such that the latter would form a narrow beam at the centre of the chamber. As expected, due to the laminar nature of the flow under our chosen operating conditions, the analyte molecules remained confined in the centre and

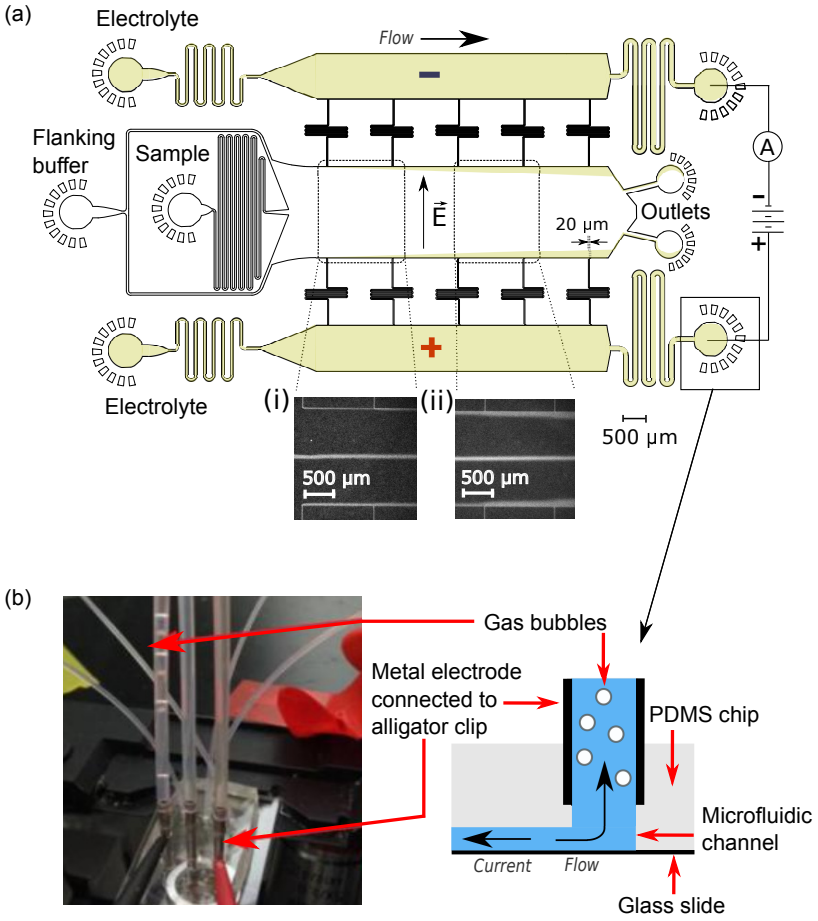

Fig. 4.2 Device design. **(a)** The electrophoresis chamber was connected to co-flowing electrolyte solution (3M KCl) through narrow perpendicular channels that control the mass transfer of the electrolyte to the electrophoresis chamber forming a thin sheet of electrolyte at the edges of the chamber (insets **(i)**, **(ii)**; visualised via the addition of trace amounts of bovine serum albumin). The areas that are filled with the electrolyte during the device operation are annotated in yellow. Electric potential was applied from metal clips at the outlets of the electrolyte channels from where it propagated to the electrophoresis channel along the flowing electrolyte solution. **(b)** The co-flowing electrolyte solution transported the electrolysis products away from the chip while simultaneously propagating the field in a direction opposite to the flow back into the device.

broadened minimally due to diffusion (Figure 4.2a, insets i-ii). The flow of the electrolyte into the two side channels was adjusted to 330 μL h^{-1} - these conditions allowed the generation of a thin sheet of the electrolyte along the edges of the main channel as is visualised in Figure 4.2a where the flow of the electrolyte was visualised by the addition of 1 mg mL^{-1} bovine serum albumin (BSA)).

To integrate electric fields with the devices, hollow metal dispensing tips were inserted to the outlets of the electrolyte channels serving as external electrodes from which the electric potentials were applied. The electrolyte effluent was collected in sections polyethene tubing connected to the metal clips (Figure 4.2b). Gas bubbles generated as a result of the electrolysis process nucleated only at the interface of the metal clips and the electrolyte solution and they were carried away from the device with the electrolyte flow such that they could not affect the electric or the flow field in the microfluidic device. The metal clips were bent at 90° angles to restrict the build-up of hydrostatic pressure at the electrolyte outlets. To ensure a stable operation, additional channels acting as hydrodynamic "resistors" were included at the electrolyte outlets - their omission was found to result in asymmetric flow profiles in the separation chamber as small variations in the depth to which the two metal electrodes were manually inserted affected the fraction of the electrolyte flow that entered the narrow perpendicular channels instead of moving directly to the electrolyte outlet. Moreover, these meandering channels were designed to have large enough hydrodynamic resistances, R_h, for the pressure drop across these channels to exceed the hydrostatic pressure in the linear section ($h \sim 10$ mm) of the metal clips:

$$R_h \cdot Q_{el,out} \sim 9 \cdot 10^{13} \ \frac{kg}{m^4 \ s} \cdot 300 \ \frac{\mu L}{h} \sim 840 \text{ Pa} \gg \rho \cdot g \cdot h = 100 \text{ Pa} \tag{4.5}$$

where $Q_{el,out}$ is the flow rate of the electrolyte out of the chip, ρ is the density of the electrolyte solution and g is the gravitational acceleration. The hydrodynamic resistance of the microfluidic channel at the electrolyte outlet was estimated from the approximate equation [183]:

$$R_h = \frac{12\eta L}{wh^3(1 - 0.63\frac{h}{w})} \tag{4.6}$$

with η being the viscosity of the solution flowing in the channel and w, h and L its width, height and length, respectively. The use of such a design strategy ensured that the fluid flow rates in the different parts of the device were controlled merely by the external injection rates and that they remained stable over the course of the separation process and beyond.

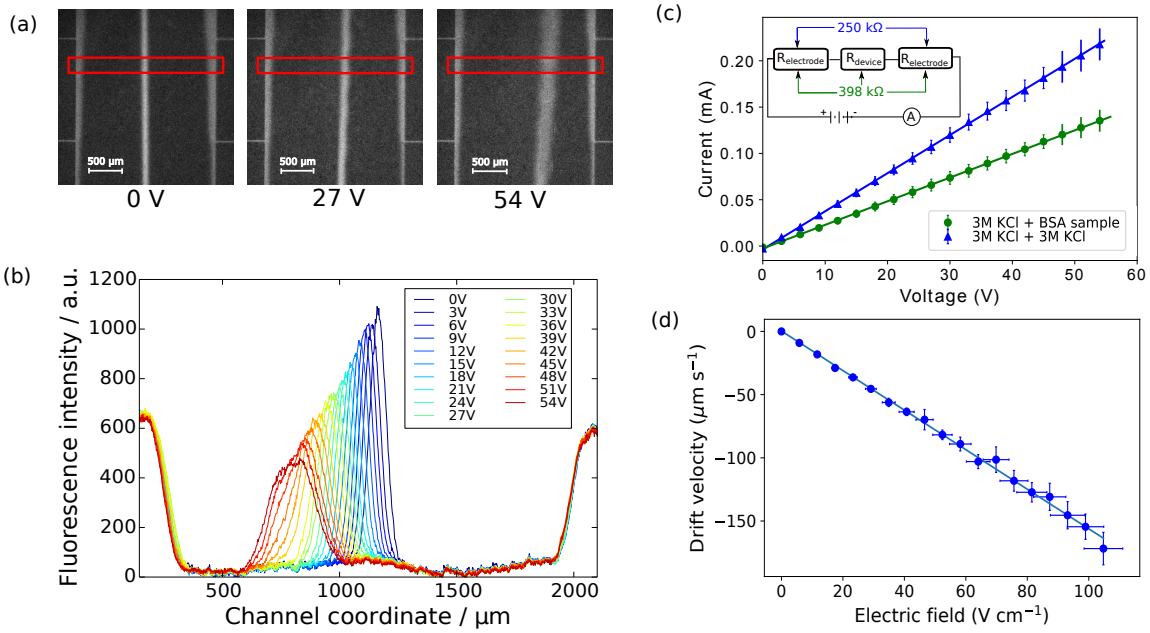

Fig. 4.3 **(a)** The movement of bovine serum albumin (BSA) in the separation chamber was recorded between 0 V and 54 V with a step size of 3 V using deep-UV fluorescent microscopy relying on the intrinsic fluorescence of proteins in this wavelength range. The images were taken between the third and the fourth connecting channels counting from upstream (Figure 4.2,ii). **(b)** The intensity profiles were extracted to quantify the movement of the molecules in the electric field and confirm that there was no bulk movement of fluid in response to the field. **(c)** The current flowing in the device was recorded at each of the voltages - first, under the conditions where the protein sample and co-flowing buffer flowed in the chamber (green circles, average of n = 3 repeats) and then replacing these by highly conductive electrolyte (3M KCl) solutions (blue triangles, average of n = 3 repeats). These data were used to estimate the electrical resistances of the electrodes (250 kΩ) and the overall device (398 kΩ), indicating around 40% voltage efficiency with around 5% uncertainty. **(d)** From these measurements, the electrophoretic mobility of the BSA sample was estimated to be $\mu_{el} = \frac{v_{drift}}{E} = (-1.58 \pm 0.17) \cdot 10^{-8}$ m^2 V^{-1} s^{-1} and its solution charge to be -7 elementary charge units.

4.2.2 Performance of the high field electrophoresis device

To examine the presence of electric field in the device, I injected bovine serum albumin (BSA dissolved to a concentration of 2 mg mL^{-1} in 10 mM phosphate buffer) molecules via the sample inlet and tracked their movement in response to applied electric field. The movement of the molecules was visualised through their intrinsic fluorescence using deep-UV fluorescence microscopy (excitation wavelength of $\lambda_{excitation} = 280$ nm; as described in Materials and Methods, Section 2.3.2) exploiting the intrinsic fluorescence of aromatic residues of proteins in this wavelength range. A voltage ramp from 0 V to 54 V with a step size of 3 V was applied using a 500 V bench power supply (Elektro-Automatik EA-PS 9500-06) and the profiles of the protein samples were recorded towards the end of the electrophoresis area at the position indicated in Figure 4.2a inset (ii) - at this distance the deflection was small enough to ensure that even at the highest voltages the protein molecules did not interact with the electrolyte that entered the electrophoresis area via the perpendicular connecting channels. The clear deflection of the negatively charged protein molecules towards the positively charged electrode indicated the presence of electric field (Figure 4.3a).

To monitor the mass transport of the electrolyte solution into the main separation channel, I supplemented the former solution with a low concentration of BSA (1 mg mL^{-1}) and observed its spatial localisation by UV microscopy when applying electric potential. As desired, the electrolyte formed a thin fluorescent layer at the sides of the electrophoresis chamber and remained at a constant position when the electric field was applied and varied (Figure 4.3b), indicating that there was no bulk movement of the electrolyte fluid into the separation area due to effects such as electroosmosis. Instead, the interface was described by diffusion of the BSA molecules. Crucially, the diffusion coefficient of BSA molecules ($6 \cdot 10^{-11}$ m^2 s^{-1}) is around two orders of magnitude smaller than that of potassium and chloride ions ($\sim 2 \cdot 10^{-9}$ m^2 s^{-1} [184, 185]). Therefore, within the same residence time the electrolyte ions diffuse about six times further. Specifically, the average residence time of the fluids within the electrophoresis chamber up to the measurement point was estimated to be

$$t_{res} = \frac{w \cdot h \cdot L}{Q} = \frac{1.8 \text{ mm} \cdot 25\ \mu\text{m} \cdot 3.8 \text{ mm}}{280\ \mu\text{L h}^{-1}} = 2.2 \text{ s} \tag{4.7}$$

indicating that the electrolyte diffused towards the centre of the separation area by around

$$x_{diff,electrolyte\text{-}ions} \sim \sqrt{2Dt_{res}} \sim \sqrt{2 \cdot 2 \cdot 10^{-9} \text{ m}^2 \text{ s}^{-1} \cdot 2.2 \text{ s}} \sim 100\ \mu\text{m} \tag{4.8}$$

This distance is an approximation as in reality the residence time varies across the cross-section of the device and is higher closer to the edges of the channel than at the centre. Nevertheless, with the width of the electrophoresis area being 2 mm, only small sections close to its sides were filled with the electrolyte and the electric field across the majority of

the width of the electrophoretic chamber could be assumed to be uniform. This conclusion was later further confirmed by a linear relationship between the applied electric field and the deflection of the BSA molecules (Figure 4.3d).

4.2.3 Quantification of the electric field

Having demonstrated that the devised and implemented downstream electrode strategy allows for the application of strong electric fields, I next demonstrate that the devices can be used for quantitative characterisation of biomolecules, including for the determining of their electrophoretic mobilities and effective charges in solution.

To obtain this insight, I set out to devise a strategy for relating the applied voltages to the electric field strengths. For this purpose, first, simultaneously with recording the fluorescence profiles (Figure 4.3b), I acquired a current vs. voltage curve and obtained an estimate for the electrical resistance of the system ($R_{EL,device} = 398 \pm 18$ kΩ; Figure 4.3c, green circles). I further noted that the separation area can be short-circuited by filling it with a highly conductive solution, such as 3M KCl. I used this procedure to estimate the electrical resistance of the electrodes ($R_{EL,electrodes} = 250 \pm 11$ kΩ; Figure 4.3c, blue triangles), yielding the following estimate for the voltage efficiency, η_{eff}, of the device:

$$\eta_{eff} = \frac{R_{EL,chamber}}{R_{EL,device}} = 1 - \frac{R_{EL,electrodes}}{R_{EL,device}} \sim 40\% \tag{4.9}$$

and an uncertainty of around 5%. The calibration step was performed for each device separately due to the differences that can occur in fabrication or in placing the metal electrodes to the electrolyte outlet orifices, or in the solution conductivities.

I further obtained a theoretical evaluation for the electrical efficiency of the device based on the estimates of the electrical resistance of the individual channels, the dimensions of which are outlined in Table 4.1. Specifically, the total electrical resistance of the device comprises of the electrical resistance of the electrophoresis channel $R_{EL,chamber}$, the electrolyte channel $R_{EL,electrolyte}$ and the perpendicular connecting channels $R_{EL,connecting\text{-}channels}$ that link the electrolyte channel to the electrophoresis area (Figure 4.2a):

$$R_{EL,device} = 2 \cdot (R_{EL,electrolyte} + R_{EL,connecting\text{-}channels}) + R_{EL,chamber}, \tag{4.10}$$

whereas the resistance of the electrodes can be estimated from:

$$R_{EL,electrodes} = 2 \cdot (R_{EL,electrolyte} + R_{EL,connecting\text{-}channels}) \tag{4.11}$$

Table 4.1 The estimates for the electrical resistances of the electrophoresis chamber and the connecting electrodes

Component	**Electrolyte outlet**	**Connecting channel**	**Electrophoresis chamber**	**Electrophoresis chamber**
Solution	3M KCl	3M KCl	3M KCl	10 mM phosphate buffer
Conductivity (S m^{-1})	25	25	25	0.08
Length (μm)	3600	3200	1800*	1800*
Width (μm)	80	20	5600	5600
Height (μm)	25	25	25	25
Resistance (kΩ)	72	256	160	0.5

* As an approximation only this fraction of the electrophoresis chamber was used that the electrolyte ions do not reach. The edge of the channel where the electrolyte ions diffuse is significantly more conductive than the central area that they do not reach.

where the resistance of each of the individual components can be calculated from the following equation

$$R_{EL,i} = \frac{1}{\kappa_i} \frac{L_i}{w_i \cdot h_i} \tag{4.12}$$

with L_i, w_i and h_i being the length, width and height of channel i and κ_i the conductivity of the solution flowing in that channel. I noted that the resistance of the electrolyte channel, $R_{EL,electrolyte}$, can be approximated as that of the narrow section at the end of it due to its much narrower width and hence larger cross-sectional area but similar length compared to that of the rest of the channel (w = 1.2 mm for the wider section and w = 80 μm for the narrower section). From the dimension of the channels and the relevant conductivity values (Table 4.1), I estimate the resistance of the device to be (equation 4.10)

$$R_{EL,device} = 160 + 2 \cdot (72 + \frac{256}{5}) = 421 \text{ k}\Omega$$

and that of the electrodes to be (equation 4.11)

$$R_{EL,electrodes} = 2 \cdot (72 + \frac{256}{5}) = 261 \text{ k}\Omega,$$

both agreeing well with the experimentally obtained results (Figure 4.3c, equation 4.9).

4.2.4 Estimation of electrophoretic mobilities and solution charges

The electrophoretic mobility, μ_{elph}, of molecules can be estimated from their movement in a perpendicularly applied electric field, E using the following relationship:

$$\mu_{\mathrm{elph}} = \frac{\mathrm{v_{drift}}}{\mathrm{E}} = \frac{\mathrm{x_{deflection}}}{\mathrm{E} \cdot \mathrm{t_{res}}} \tag{4.13}$$

where $\mathrm{v_{drift}}$ is the speed at which the analyte molecules move in the direction of the applied field. Due to the high aspect ratio of the separation chamber ($\frac{\mathrm{w}}{\mathrm{h}} = \frac{2000\ \mu\mathrm{m}}{25\ \mu\mathrm{m}} = 80$), the fluid velocity along the majority of its width was constant and hence, the residence time of the BSA molecules in the section of the channel up to the measurement point could be estimated $\mathrm{t_{res}} = 2.2$ s as per equation 4.7.

The drift velocity $\mathrm{v_{drift}}$ of the BSA molecules was estimated from the deflected distances, $\mathrm{x_{deflection}}$ extracted from the micrographs in Figure 4.3b and was found to vary linearly with applied electric field (Figure 4.3d). From these data, I estimated the electrophoretic mobility of the BSA molecules to be:

$$\mu_{\mathrm{elph,BSA}} = \frac{\mathrm{v_{drift}}}{\mathrm{E}} = (-1.58 \pm 0.17) \cdot 10^{-8}\ \mathrm{m^2\ V^{-1}\ s^{-1}}$$

Moreover, using the Einstein electrical mobility equation

$$\mathrm{q} = \frac{\mu_{\mathrm{elph}} \cdot \mathrm{kT}}{\mathrm{D}} \tag{4.14}$$

and a literature value for the diffusion coefficient of BSA ($\mathrm{D_{BSA}} = 6.3 \cdot 10^{-11}\ \mathrm{m^2\ s^{-1}}$ [16]), I estimated the solution charge of the BSA molecules to be -7 elementray charge units. This estimate is in agreement with values obtained by previously described approaches for estimating solution charges [186, 187].

4.2.5 Separation and analysis of biological mixtures

Determining native charges of proteins in a mixture I have shown that the device described in this Chapter presents a combined ability to apply high electric fields and maintain an accurate flow profile through the device even when strong fields are applied. This opens up the further possibility of determining the electrophoretic mobilities of individual biomolecules when they are present in mixtures.

I demonstrated this possibility by applying an electric field to a mixture of BSA (pI 5) and human lysozyme (pI 9) in 10 mM sodium phosphate buffer pH 7.4. The two molecules fully separated under the electric potential (Figure 4.4) and I estimated their mobilities to be $(2.0 \pm 0.2) \cdot 10^{-8}$ m^2 V^{-1} s^{-1} for the lysozyme and $(-1.7 \pm 0.2) \cdot 10^{-8}$ m^2 V^{-1} s^{-1} for the BSA molecules (Figure 4.4b).

Detecting protein interaction native charges of proteins in a mixture. Due to its liquid-phase operation, the described platform can be used for detecting interactions between proteins and for further separating proteins and protein complexes from one another directly in the native environment. To show the power of this approach, I examined the mixture of an aggregate forming protein Amyloid-β (Aβ) and a molecular chaperone Brichos.

Aβ is a polypeptide that is prone to self-association and fibril formation, its assembly is believed to play a critical and potentially a casual role in the development of Alzheimer's disease [118]. The pathway of Aβ aggregation involves a transient heterogeneous mixture including oligomeric species of a range of different association numbers and structural forms. Molecular chaperones play a key role in aiding the folding process of newly synthesised proteins into their native states and preventing proteins from aggregating. Brichos in particular has been found to inhibit misfolding and aggregation of Aβ both *in vitro* and *in vivo* [119, 188].

To investigate whether Brichos molecules bind to aggregated forms of Aβ protein, I incubated a mixture of aggregated Aβ (24 μM) and fluorescently labelled Brichos (0.45 μM) and exposed it to electric field to examine the presence of a fibril-chaperone complex. The proteins were prepared and labelled as described in Materials and Methods (Section 2.3.1). By comparing the behaviour of the individual Brichos molecules and that of its mixture with Aβ, I concluded the formation of a complex between Brichos and Aβ fibrils (Figure 4.5a-b) and further fully separated the fibril-chaperone complex from the individual chaperone molecules. The occurrence of this interaction is in agreement with an earlier observation of Brichos molecules binding to Aβ fibrils - this interaction is believed to inhibit the potential secondary nucleation events that could otherwise occur on the fibril surfaces [189]. Non-covalent and reversible interactions between biomolecules, such as proteins are the basis of an extremely wide range of biophysical and biochemical processes and due to their modulation by solution conditions, these interactions are best studied under native conditions in aqueous environments. My developed device is ideally suited for probing interactions in biological mixtures as not only is there no interference with a support medium in contrast to more commonly used biophysical separation techniques, such as chromatography or protein gels, it also allows probing these interactions at short timescales not accessible with conventional techniques.

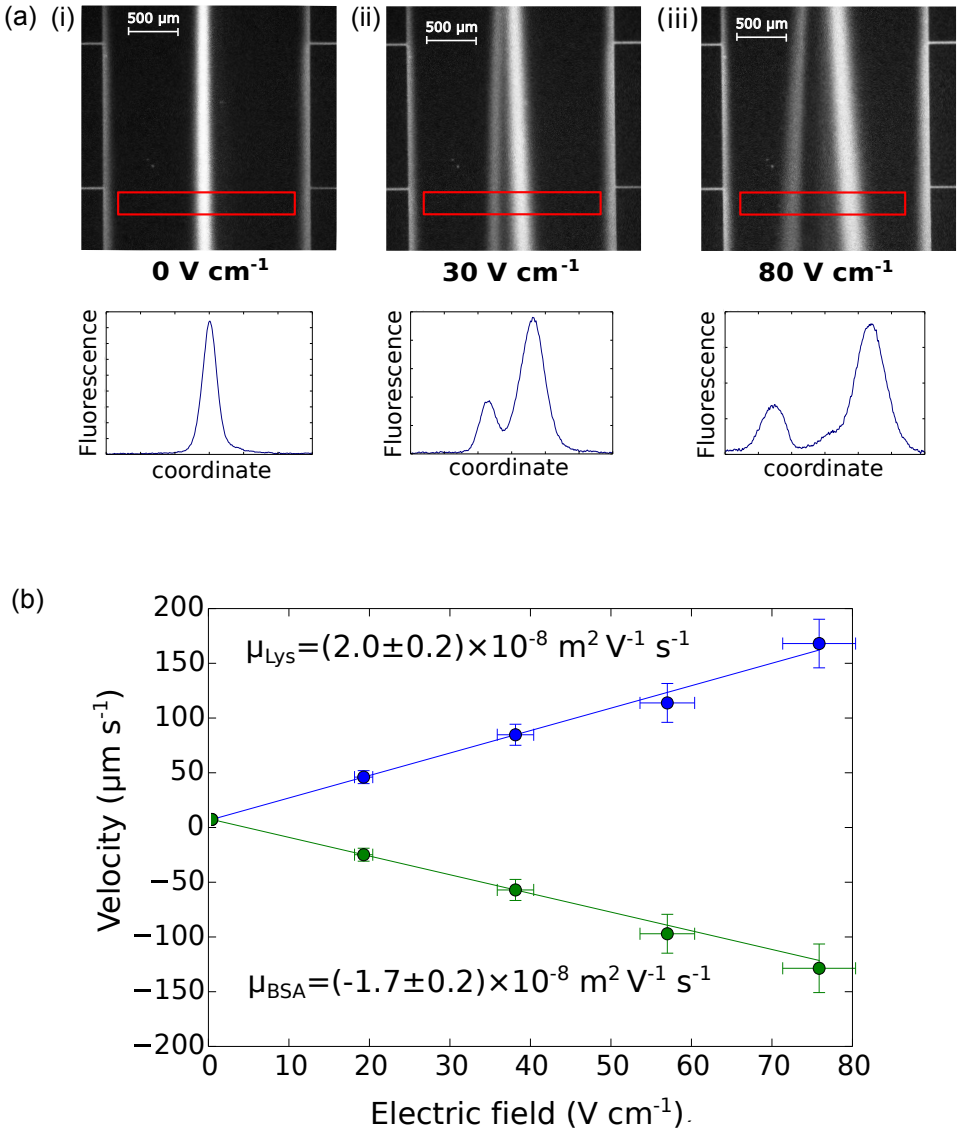

Fig. 4.4 Separation and analysis of a protein mixture. **(a)** UV fluorescent micrographs and extracted fluorescence profiles (red rectangle) of the separation of bovine serum albumin (BSA; 2.5 mg mL^{-1}; pI 5) and human lysozyme (Lys; 4.0 mg mL^{-1}; pI 9) at **(i)** 0 V cm^{-1}, **(ii)** 30 V cm^{-1}, **(iii)** 80 V cm^{-1}. **(b)** The profiles were used for the quantification of the electrophoretic mobilities of the two proteins in the mixture - $\mu_{\text{elph, lys}} = (2.0 \pm 0.2) \times 10^{-8}$ m^2 V^{-1} s^{-1} and $\mu_{\text{elph, BSA}} = (-1.7 \pm 0.2) \times 10^{-8}$ m^2 V^{-1} s^{-1} - calibrating the device as described in Figure 4.3c.

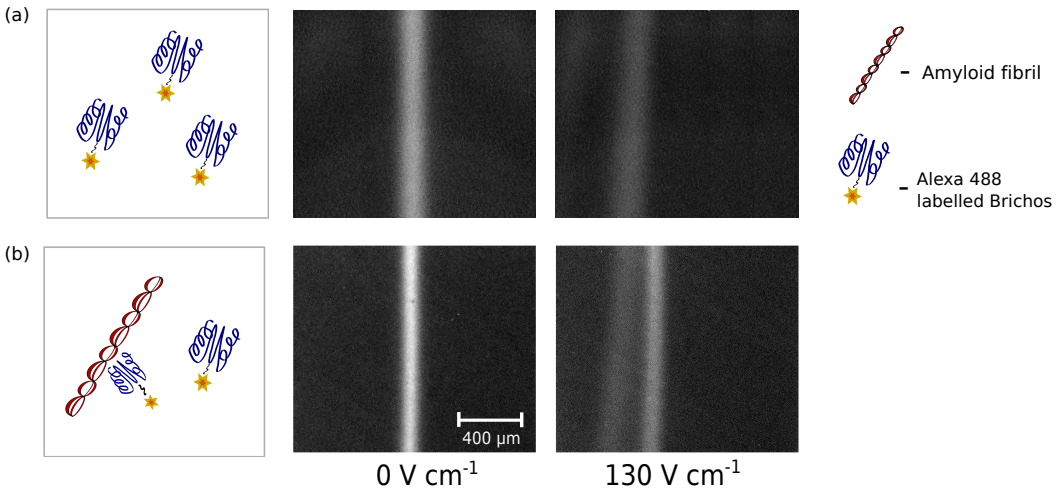

Fig. 4.5 Brichos molecules were labelled with a fluorescent dye (Alexa 488) and mixed with Amyloid-β fibrils in order to test their binding to the fibrils. By comparing the behaviour of **(a)** pure Brichos and **(b)** Brichos molecules mixed with the fibrils, I concluded the formation of Brichos-Amyloid-β fibril complex and purified this complex from the unbound Brichos molecules.

4.3 Enhancing the resolution limit of free flow electrophoresis

Despite its attractive features, micron scale separation platforms have remained limited in their ability to work with heterogeneous samples. In addition to the lack of effective and reproducible methods for the integration of electric fields with micron scale channels, an additional challenge has been the limited number of components that current electrophoretic devices can separate. In this Section, I first describe the underlying causes for this limitation and then proceed with addressing its most critical contributions with the goal to yield a strategy for advancing current resolution limits. The work is based on the patent application described in reference [157] and publication described in reference [158].

From the data in Figure 4.3a-b, I observed that when the protein sample deflects in response to the applied field, the beam broadens significantly, affecting the ability of the device to effectively separate and analyse complex mixtures. The observed variance of the analyte band, σ^2_{total}, can described as the sum of the variance contributed by several sources: the finite bandwidth of the sample stream (σ^2_{inj}), diffusion (σ^2_{D}), hydrodynamic (σ^2_{HD}) and electrodynamic (σ^2_{DE}) effects, electrohydrodynamic distortion (σ^2_{EHD}) and Joule heating (σ^2_{JH}) [190]:

$$\sigma^2_{\text{total}} = \sigma^2_{\text{inj}} + \sigma^2_{\text{D}} + \sigma^2_{\text{HD}} + \sigma^2_{\text{ED}} + \sigma^2_{\text{EHD}} + \sigma^2_{\text{JH}} \tag{4.15}$$

Effective approaches for supressing the latter three of these effects have been proposed and demonstrated previously [182, 191, 192]. Specifically, in the experiments performed in this Chapter (Section 4.2), I removed electrohydrodynamic broadening contributions by dissolving the sample in the same buffer as the carrier medium [182, 193] and concluded the absence of significant electrodynamic broadening effects from the stable position of the electrolyte with varying electric field strength (Figure 4.3b). The absence of the electrodynamic broadening contribution was further confirmed by the linear relationship between the drift velocity of the molecules, v_{drift}, and the applied field, E, (Figure 4.3d), which would not be the observed in the presence of notable electroosmotic flow involving bulk movement of the electrolyte solution within the separation chamber. Indeed, the observed variance of the beam, extracted from the data shown in Figure 4.3b, could be characterised well by the diffusive and hydrodynamic broadening effects, with the two contributions approximated as described by Fonslow et al. [181] (Figure 4.6):

$$\sigma^2_{\text{total}} \sim \sigma^2_{\text{inj}} + \sigma^2_{\text{D}} + \sigma^2_{\text{HD}} = \frac{\text{w}^2_{\text{inj}}}{12} + \frac{2\text{DL}}{\text{v}} + \frac{\text{h}^2\text{d}^2\text{v}}{105\text{DL}} \tag{4.16}$$

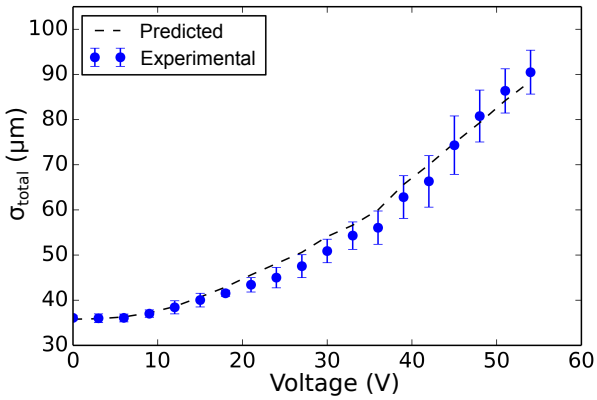

Fig. 4.6 The variance of the analyte beam at each of the applied voltages (blue circles) based on the results in Figure 4.3. The broadening can be described by equation 4.16 (black line).

where σ^2_{inj} is the variance of the injected sample band, and σ^2_{D} and σ^2_{HD} describe the its variance arising from the diffusive and hydrodynamic broadening effects, respectively.

However, strategies that would simultaneously eliminate the two factors that contribute towards the broadening of the beams as a consequence of the fluid flow - diffusive and hydrodynamic broadening - have been challenging to devise. Indeed, the former of these effects appears due to the random diffusional movement of the analyte molecules and could be in principle alleviated by increasing the fluid flow rate and thus the residence time of the analyte molecules in the separation chamber. The latter contribution, however, arises from the parabolic velocity profile along the height of the separation chamber with effectively zero flow near the walls of the chamber due to non-slip boundary condition (Figure 4.7a, inset) [181, 190] - this leads to a variation in the times that different analyte molecules spend in the separation area and hence to their differential deflection. In contrast to the diffusive broadening, this effect becomes particularly pronounced when high sample processivity is required [158, 181] - increasing the flow rates of the sample and carrier fluid leads to an elevated pressure drop between the inlet and the outlet of the device and hence, according to the Hagen-Poiseuille law, to an increased velocity gradient and elevated variations in the residence times of the analyte molecules. From equation 4.16, the relative width of the sample beam in the electrophoresis chamber, $\frac{\sigma_{\text{total}}}{\text{w}}$, can be described in terms of the relative deflection of the analyte, $\text{C} = \frac{\text{x}_{\text{deflection}}}{\text{w}}$ by which the analyte beam is deflected away from its

original position as:

$$\begin{aligned}\left(\frac{\sigma_{\text{total}}}{\text{w}}\right)^2 &= \left(\frac{\text{w}_{\text{inj}}^2}{12\text{w}^2}\right) + \frac{2\text{DL}}{\text{vw}^2} + \frac{\text{h}^2\text{d}^2\text{v}}{105\text{DLw}^2} \\ &= \left(\frac{\text{w}_{\text{inj}}^2}{12\text{w}^2}\right) + 2\text{D}\left(\frac{\text{h}}{\text{w}}\right)\left(\frac{\text{L}}{\text{Q}}\right) + \frac{\text{C}^2}{105\text{D}}\left(\frac{\text{Q}}{\text{L}}\right)\left(\frac{\text{h}}{\text{w}}\right)\end{aligned} \tag{4.17}$$

From the latter equation, I conclude that the minimum broadening for a molecule with a diffusion coefficient D at a specific relative deflection C occurs when the injection beam width $\frac{\text{w}_{\text{inj}}}{\text{w}}$ and the aspect ratio of the channel $\frac{\text{h}}{\text{w}}$ are both minimised and further when flow rate to channel length ratio, $\frac{\text{Q}}{\text{L}}$ is at its optimal value described by:

$$\frac{\text{d}}{\text{d}(\frac{\text{L}}{\text{Q}})}\left[\left(\frac{\sigma_{\text{total}}}{\text{w}}\right)^2\right] = 2\text{D}\left(\frac{\text{h}}{\text{w}}\right) - \frac{\text{C}^2}{105\text{D}}\left(\frac{\text{Q}}{\text{L}}\right)^2\left(\frac{\text{h}}{\text{w}}\right) = 0 \tag{4.18}$$

Condition 4.18 is satisfied when $\frac{Q}{L} = \frac{\sqrt{210}\ D}{C}$.

Based on this estimate, the minimum possible analyte beam broadening at a specific relative deflection C can be described to be

$$\begin{aligned}\left(\frac{\sigma_{\text{total}}}{\text{w}}\right)^2 &= \left(\frac{\text{w}_{\text{inj}}^2}{12\text{w}^2}\right) + \frac{2\text{C}}{\sqrt{210}}\left(\frac{\text{h}}{\text{w}}\right) + \frac{\text{C}\sqrt{210}}{105}\left(\frac{\text{h}}{\text{w}}\right) \\ &= \left(\frac{\text{w}_{\text{inj}}^2}{12\text{w}^2}\right) + 2\text{C}\sqrt{\frac{2}{105}}\left(\frac{\text{h}}{\text{w}}\right)\end{aligned} \tag{4.19}$$

Hence, for instance, for a relative deflection of C = 45% from the centre of the channel the minimum possible beam width - defined as the full width of the beam at its half maximum height - is over 8% of the total channel width for the case when the analyte is filling 5% of the channel at the injection and channel aspect ratio of $\frac{\text{h}}{\text{w}} = \frac{25\ \mu\text{m}}{2000\ \mu\text{m}} = 0.0125$ as was used in this work, indicating that the device could be used for separating up to 8 components depending on how optimally their electrophoretic mobility values spread. Theoretically, for a relative injection width $\frac{\text{w}_{\text{inj}}}{\text{w}}$ of 1% and channel aspect ratio of $\frac{\text{h}}{\text{w}} = \frac{10\ \mu\text{m}}{10000\ \mu\text{m}}$, which could be achieved by placing support pillars in the separation chamber, the beam width at a relative deflection of C = 45% could be reduced from 12.5% to around 2.5%, while the less deflected analytes would remain more confined to, for instance, 1.2% of the channel width at a C = 10% relative deflection.

As such, the fast flow rates that would on the one hand suppress the diffusive broadening extent, on the other hand lead to an elevated hydrodynamic broadening contribution. In

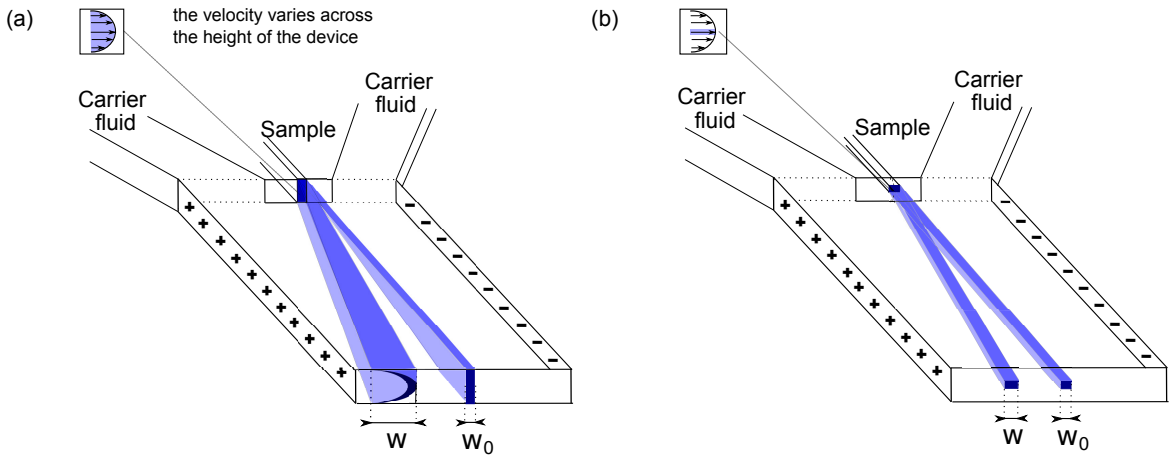

Fig. 4.7 Broadening in free flow electrophoresis devices. **(a)** Pressure difference between the inlet and the outlet of the separation chamber leads to a parabolic velocity profile along the height of the chamber with nearly zero velocity in the vicinity of its walls (inset). This leads to a variation in the times different analyte molecules spend in the device and thus to the broadening of the analyte beam from its original width at no deflection, w_0, to a larger width, w, when the molecules are deflected, substantially limiting the resolution of the separation process. **(b)** This effect can be alleviated by selectively injecting the sample to the areas where velocity gradient and hence the variations in the times that different molecules spend in the separation area are the smallest, minimising the differences in their deflections.

this Section, I describe a strategy for overcoming this limitation and suppressing the two contributions simultaneously. Specifically, I restrict the injection of the sample spatially only into those areas of the separation chamber where the variations in the velocity distribution are minimal (Figure 4.7b). I show how this strategy results in a five-fold increase in the resolution limit compared to earlier described free flow electrophoresis devices and illustrate that further enhancements in the resolution are possible when the sample is collected within the central layers only. The device design strategy and the results are based on a published article [158].

4.3.1 Simulating the broadening effect in 2D and 3D free flow electrophoresis devices

To first test the theoretical enhancement in resolution that could be achieved using a controlled sample injection strategy, I simulated the movement of individual particles - their diffusive and advective transport in combination with their movement in a simultaneously applied

electric field. To this effect, I modelled the behaviour of the particles in a 50 μm high, 1400 μm wide and 5000 μm long rectangular channel, as was later fabricated experimentally (Section 4.3.3). The movement of the particles in the micron scale channels was simulated using Langevin dynamics codes written in C^{++} [194]. The following equations were used to simulate the movement of the k^{th} particle in the separation area:

$$x_k^{(i+1)} = x_k^{(i)} + v_x(y_k^{(i)},\ z_k^{(i)}) \cdot\ \Delta t + \sqrt{2D\Delta t} \cdot \text{Random}\{-1, +1\} \tag{4.20}$$

$$y_k^{(i+1)} = y_k^{(i)} + \sqrt{2D\Delta t} \cdot \text{Random}\{-1, +1\} + \mu \cdot E \cdot \Delta t \tag{4.21}$$

$$z_k^{(i+1)} = z_k^{(i)} + \sqrt{2D\Delta t} \cdot \text{Random}\{-1, +1\}, \tag{4.22}$$

where the x-axis is in the direction of the length of the channel, y-axis in the direction of its width, z-axis along is height and v_x is the advective flux velocity in x-direction, Δt is the time internal for the simulations, D is the diffusion coefficient of the analyte, μ is its electrophoretic mobility and E the strength of the electric field in the channel. The simulations were carried out with reflective boundary conditions at the device walls using a total of $N = 2 \cdot 10^6$ molecules, which was found to be a large enough number to yield smooth profiles and for understanding the movement trends within the channels. In order to predict the profiles at a specific position along the channel the particle movement was simulated to the point of interest along the length of the channel and the distributions along the y-axis plotted by either averaging the particle distributions along the entirety of the z-axis for full collection or along a section of interest only for spatially controlled collection. Specifically, I modelled the movement of a representative protein molecule with a diffusion coefficient of $D = 7 \cdot 10^{-11}$ m^2 s^{-1} (hydrodynamic radius of $R_h = 3.0$ nm) and electrophoretic mobility of $\mu = 2\ \cdot\ 10^{-8}$ m^2 s^{-1} V^{-1}. This is typical of a protein with isoelectric point in the range of 4-6 under physiological pH - around a third of the proteins in the human proteome are predicted to have their isoelectric point values in that range [164, 165].

I first modelled the movement of the particles in the electric field at a flow rate of 800 μL h^{-1} with the sample injected over the full height of the device. I observed there to be significant variations in the distribution of the analyte molecules across the height of the chamber at the device outlet (Figure 4.8a). Specifically, the molecules were more spread in the layers that were further away from the centre (purple line - layers within 0-10% of the total height of the device away from the wall; red line - layers within 20-30% of the total height away from the wall) than in the central layers (green line - layers within 45-55% of the total height away from the wall). All profiles were normalised by the total number of molecules in that layer.

These data indicate that a significant fraction of the protein molecules does not explore the full height of the device but remain in the vicinity of the layer to which they were originally

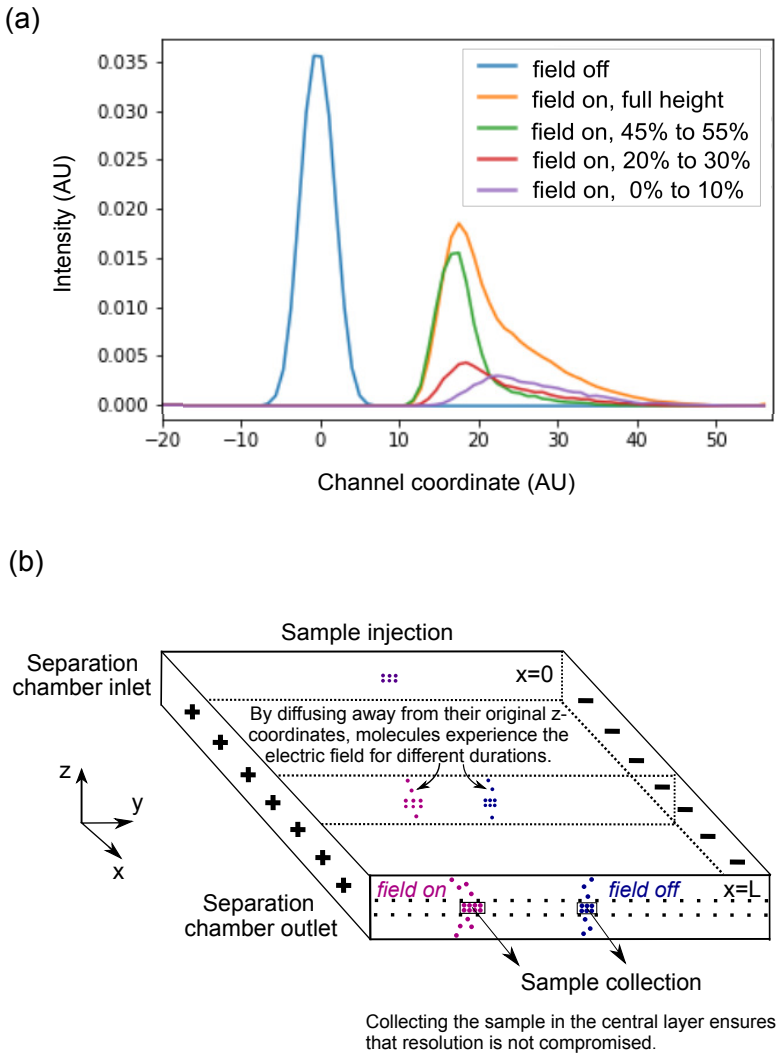

Fig. 4.8 Motivation for spatially controlled collection in free flow electrophoresis. **(a)** By simulating the movement of the analyte molecules in the electrophoresis chamber, I observed the analyte beam being substantially more spread in the layers that are further away from the centre (purple line - layers within 0-10% of the total height of the device away from the wall; red line - layers within 20-30% of the total height away from the wall) than in the central layer (green line - layers within 45-55% of the total height away from the wall). The blue line and orange lines correspond to the profiles of the analyte molecules averaged across the full height of the device with and without any electric field applied, respectively. The simulations were performed at Péclet number of $\mathrm{Pe} = 22$ with molecules injected over the full height of the devices. All the shown profiles were normalised by the total number of particles in these layers. **(b)** Based on this variation in the profiles, I propose that a further reduction in the broadening of the analyte beam could be achieved by selectively collecting the sample in the central area only.

injected to. Indeed, under these conditions, the Péclet number, describing the ratio of the diffusive time scale in the z-direction and the advective time scale in the x-direction, can be estimated to be:

$$\mathrm{Pe} = \frac{t_{\mathrm{diffusive,x}}}{t_{\mathrm{advective,y}}} = \frac{{}^{L}/_{u}}{{}^{h^2}/_{D}} = \frac{36\ \mathrm{s}}{1.6\ \mathrm{s}} = 22 \tag{4.23}$$

indicating that the diffusive time scale along the z-axis of the device is significantly longer than the advective timescale along the x-axis. Whereas the layers the furthest away from the centre of the device show the widest distribution in their deflections (Figure 4.8a, purple line), I observed a tail in the distribution even in the central layers (green line) compared to the profile with no field applied (blue line). This tail originated from the small fraction of particles that diffused away from the central layers but also diffused back to these layers.

The data in Figure 4.8a suggest that an enhancement in the resolution could be achieved by collecting the sample in the central layers only (Figure 4.8b). I explored this effect further by modelling the behaviour of the particles in the electrophoresis chamber under three different flow rates, 200, 800 and 2000 μL h^{-1}, illustrate the sample behaviour under different Péclet number conditions estimated to be Pe = 5.6, Pe = 22, Pe = 56 for the three flow rates respectively. The distribution of the molecules across the width of the chamber is shown in Figure 4.9a-c with no electric field applied (red line) and with electric field applied while injecting the sample over the full height of the device (green line), while injecting the sample into the layers within the central 10% of the height of the device (blue line) and while further collecting the centrally injected sample only in the layers within the central 10% of the device height (purple line). The applied voltage was kept indirectly proportional to flow rate to ensure identical deflection under the different flow rates.

At low Péclet number, the differences in the profiles were observed to be small (Figure 4.9a). Indeed, under these conditions the time scale for the diffusional movement along the height of the device is comparable to that of the advective movement along the channel length, meaning that a significant fraction of the centrally injected molecules can move away from the position they were injected to and experience a longer residence time. Under these conditions the broadening is predominantly arising from simple diffusive rather than hydrodynamic broadening. In contrast, at high Péclet numbers (Figure 4.9b-c), the diffusive timescale is significantly longer than the advective one and within the analysis time the molecules stay in the central area where they were injected to such that the variation in their residence times remains minimal. By combining the central injection and collection strategies, almost all the hydrodynamic broadening effect can be suppressed (Figure 4.9b-c, purple line) with the high flow rate also further suppressing diffusional broadening as can be seen when comparing the peak intensities of the distribution profiles with and without applying the field (Figure 4.9c, red and purple lines). The central injection and collection are of particular importance under

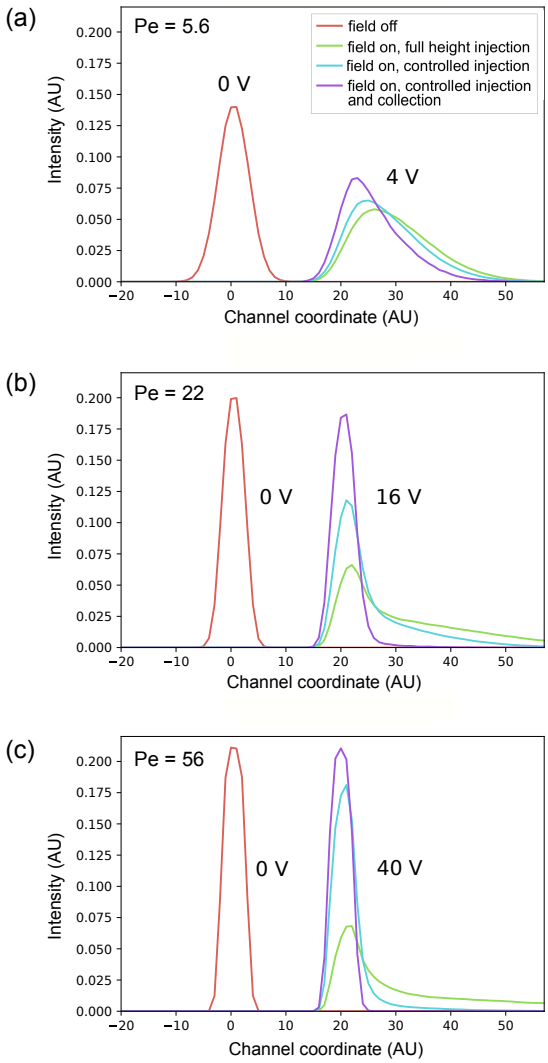

Fig. 4.9 Comparison of the beam broadening effect with spatially controlled and non-controlled sample injection and collection. The profiles were simulated at Péclet numbers of **(a)** Pe = 5.6, **(b)** Pe = 22, and **(c)** Pe = 56, with no electric field applied (red line) and with electric field applied while injecting the sample over the full height of the separation chamber (green line), while injecting the sample to the layers within the central 10% of the height of the device (blue line) and while also collecting the sample only over the layers within the central 10% of the height of the device (purple line). The applied voltage was varied inversely with the flow rate such that the analyte deflection would remain constant between the different flow rates. The simulation results indicated that the reduction in the broadening effect compared to conventional free-flow electrophoretic setups is the most pronounced at the highest Péclet numbers and when both the sample injection and collection are restricted to the central layers only - under these conditions virtually all broadening can be eliminated.

these high Péclet number conditions as the high flow rates and strongly pronounced parabolic velocity profiles lead to an extremely wide width of the analyte beam when neither the injection nor the collection is spatially controlled (Figure 4.9b-c, green line). Indeed, in conventional free flow electrophoresis devices, the diffusive broadening effect decreases with increased flow while the hydrodynamic broadening effect decreases with decreased flow and as such, there is an optimum flow rate at which the overall broadening effect can be minimised [158, 195]. In contrast, for the spatially controlled injection and collection strategy modelled here both the diffusive and the hydrodynamic broadening contributions decrease with increasing flow rate. This generates the possibility to, in principle, remove all of the broadening effect from these two sources rather than operate the devices under conditions which achieve a compromise between the two effects but do not give the option to simultaneously prevent them.

4.3.2 Fabrication of high detection limit free flow electrophoresis devices with spatially controlled sample injection

Having established the attractiveness of spatially controlling the sample injection and collection, I next set out to fabricate such devices and validate the predictions experimentally.

Spatially controlled injection of samples has been achieved in macroscale devices (total volumes order of millilitres) through the use narrow plastic capillary tubes penetrating into the chamber and bent in the direction of flow [196]. Such capillary based sample injection procedure would be challenging to achieve on micron scale, especially if more than one component is to be accurately positioned as would be desired, for instance, when the analyte is both injected and collected centrally to further increase the resolution of the separation process [158]. To overcome this limitation and implement and implement spatial control in micron scale setups in a scalable and reproducible manner, I instead used multilayer soft-photolithography fabrication strategy involving the fabrication of polymer slabs that include structures of varying heights. By bonding two such slabs to each other, it becomes possible to form an orifice at the centre of the separation chamber wall through which analyte molecules enter (Figure 4.7b) or exit the separation chamber.

With such lithographically produced devices the sheath flow regime can be established at the moment when the sample enters the separation chamber and the electric field. Furthermore, the carrier fluid could surround the sample at a range of geometries which is not the case for an inserted capillary where the fluid always surrounds the sample instantaneously in a sheath flow mode. Furthermore, whereas integrating central injection and collection simultaneously with their positions aligned with each another would be extremely challenging to achieve with strategies that rely on the accurate placement of external components such as

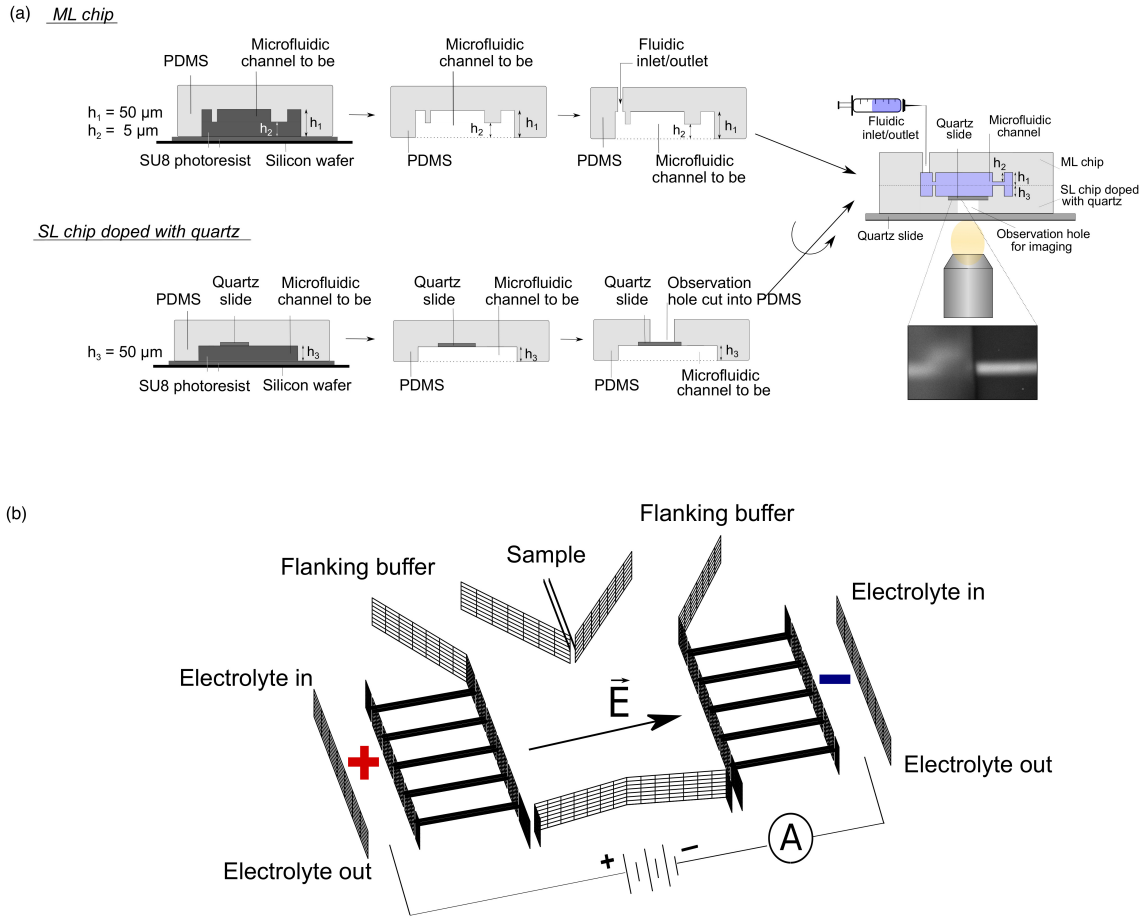

Fig. 4.10 **(a)** Fabrication of multilayer chips with integrated quartz windows for enhanced fluorescence detection. 3D microfluidic devices were fabricated by bonding a multilayer (ML; top row) and a singlelayer (SL; bottom row) chip to one another. A quartz slide was incorporated into the SL chip before curing the PDMS and the PDMS was then removed from the top of the quartz slide with a scalpel in order to introduce a non-PDMS based observation hole for imaging. Fluidic ports were introduced only to the ML chip. The two chips were plasma-bonded to one another and the hybrid 3D chip was imaged via the observation hole fabricated into the PDMS so that the LED light would not need to pass through PDMS for the excitation and the collection of the emitted light. **(b)** The architecture of spatially controlled sample injection free flow electrophoresis chip. The sample inlet and the connecting "bridges" between the electrolyte channel and the separation chamber were fabricated onto the thin layer of the ML PDMS chip mould only with the rest of the structures fabricated onto both the thicker layer of the ML PDMS chip mould and the SL PDMS chip mould.

capillaries, their simultaneous implementation involves no additional complications when the devices are produced from lithographically fabricated polymer slabs. Last but not least, this strategy ensures that the device is fabricated from a single material, which would allow their production through scalable methods, such as injection moulding.

A major obstacle in producing the devices through such previously described multilayer lithography approaches is the necessity to visualise the chip through the polymer in which the microfluidic channels are produced. This requirement substantially reduces the sensitivity of the setups as the majority of the polymers used for replicable production of micron scale devices are either optically non-transparent or exhibit some degree of autofluorescence, therefore generating noticeable background signals [197].

To circumvent this problem and effectively visualise the movement of the analyte molecules, I devised a strategy for integrating observation windows with the regions of the chip that were used for sample visualisation and analysis (Figure 4.10a). To achieve this objective, I produced the two patterned polydimethylsiloxane (PDMS) slabs using a ML replica mould for one of the slabs and a singlelayer SL mould for the other slab. I converted the former mould to a PDMS chip using standard soft-photolithography approaches and the latter by integrating a non-PDMS based observation window as illustrated in Figure 4.10a and described in detail in the next paragraphs. The mould for the SL PDMS slab was fabricated to a height of 50 μm and it included all the structures of the device with the exception of the protein inlet and the "bridges" connecting the electrolyte channels to the electrophoresis chamber. The ML replica included structures of two distinct heights: the protein inlet as well as the connecting "bridges" featured only on the shallow (5 μm) layer whereas the buffer inlet, the electrophoresis chamber and the electrolyte channels were fabricated onto the tall (50 μm) layers only identically to how they appeared on the SL mould.

To integrate non-PDMS based observation windows with the SL PDMS chip, small pieces of quartz (ca. 5 mm $\times$ 5 mm) cut out from a 1 mm thick quartz slide (Alfa Aesar) were placed on top of the SU-8 structures of the replica mould in the areas where the imaging was due to take place (Figure 4.10a, bottom) before the structures were cast in PDMS. The quartz pieces were carefully pressed against the SU-8 structures not to destroy the master mould but to ensure that as little PDMS as possible remained between the quartz and the SU-8 structures. The PDMS was then cured by heating it at 65°C for 2 hours - longer baking times were found to cause strong adhesion of the quartz to the SU-8 structures. The PDMS doped with quartz was then carefully peeled off from the SU-8 mould and the section of PDMS above the quartz slide removed with a scalpel to generate a non-PDMS based area for imaging where the excitation and emission takes place through the quartz (Figure 4.10a). Inlets for fluidic connections were introduced to the ML PDMS chip using 0.75 mm inner

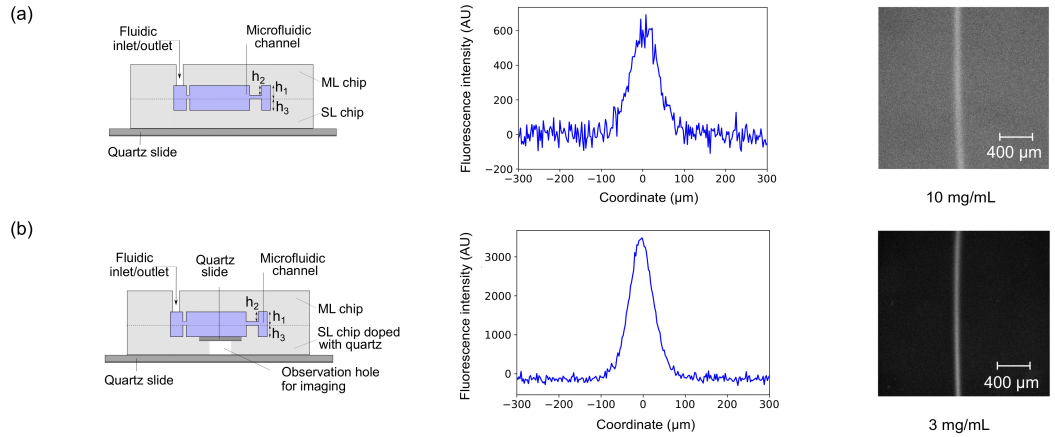

Fig. 4.11 The profile of the sample analyte beam **(a)** in conventional 3D device at 10 mg mL^{-1} and **(b)** in the hybrid 3D device at 3 mg mL^{-1}. The inclusion of the observation window was seen to substantially enhance the signal to noise ratio, opening up the possibility of optical detection in structures that are embedded in polymer matrices.

diameter reusable biopsy punch (World Precision Instruments), no ports were introduced to the SL PDMS-quartz chip as it faced downwards during the imaging.

Finally, the SL PDMS-quartz hybrid chip and the ML PDMS chip were bonded to each other to form the 3D injection orifice. To achieve an alignment accuracy of the order of micrometres between the two chips, drops of water were sprayed onto the two plasma activated chips before they were aligned under a stereomicroscope as described in Materials and Methods (Section 2.1.3). Although in principle, the role of the two chips could be reversed with the ML chip including the observation area and the SL chip including the inlets and outlets for sample injection and removal, I decided to fabricate the quartz slide into the SL chip as occasionally the SU-8 structures can come off from the silicon wafer together with the PDMS and the production of SL chips is more straightforward than that of ML chips. A sketch of the resulting device is shown in Figure 4.10b.

I compared the sensitivity of these 3D quartz-doped PDMS devices including dedicated areas for detection to the sensitivity of 3D PDMS devices through conventional multilayer soft-photolithography processes. I observed an order of magnitude enhancement in the signal to noise ratio (Figure 4.11a-b). This enhanced sensitivity opens up the possibility to image analyte molecules in structures embedded inside polymer matrices, such as the separation device with a spatially controlled injection orifice under discussion here.

4.3.3 Experimental performance of the free flow electrophoresis devices with spatially controlled sample injection

Finally, I explored the improvements in the resolution limit that can be achieved using such spatially controlled sample injection strategy. To fabricate the devices, I used the fabrication strategy described in Section 4.3.2 with strong electric fields integrated using the approach developed and described in Section 4.2, where the electric potential was applied outside and downstream of the microfluidic separation chamber and the field propagated back to the separation area through the use of a co-flowing highly conductive electrolyte solution (Figure 4.2a). While the narrow fluidic "bridges" between the electrolyte channels and the separation chamber allowed the propagation of the electric field to the separation region of the device, they simultaneously provided a high hydrodynamic resistance to prevent the electrolyte from filling the full separation area and short-circuit the device but instead permit its slow leakage into the separation chamber and the formation of a stable conductive sheet on the edges of the chamber acting as an electrode. In this 3D device architecture, in addition to the protein inlet channels, I also fabricated the connecting electrolyte bridges only in the middle layer of the three-layered device (thinner layer of the ML chip mould) where their height is low to ensure that with their lengths and widths fixed the "bridges" would have their hydrodynamic resistance maximised but electric resistance minimised (Figure 4.10b).

To test the performance of the devices, injected bovine serum albumin (BSA) molecules and carrier medium into the device via their respective inlets at 20 and 380 μL h^{-1} for the 2D devices and at 4 and 800 μL h^{-1} for the 3D devices to yield similar profiles at 0 V cm^{-1} where the beam width is determined by the original sample width and any diffusive broadening that occurs. A voltage ramp from 0 V to 120 V was applied across the devices and the deflection of the BSA molecules recorded by a home-built inverted UV-microscope (Figure 4.12a) for both chips. The field strength was determined using the calibration strategy described earlier where an independent estimate was obtained for the resistances of the electrodes by filling the electrophoretic chamber with a highly conductive fluid [156].

The profiles at different field strengths for the 2D and 3D devices are shown in Figure 4.12b. To quantify these results, the half-width of the analyte beam at its the full-height was used as the parameter to describe the broadening effect. The broadening extent, describing the difference in the half-width at a specific voltage and at 0 V, was found to be around five times smaller for the devices with restricted injection (Figure 4.12c green triangles; 160 μm) than for those with non-restricted injection (Figure 4.12c blue squares; 30 μm) at the maximum deflection studied. I further note that it is possible to reduce the initial width of the analyte beam by adjusting the relative flow rates of the sample solution and the carrier fluid. By doing so, the width of the original beam can be reduced to very small values and in these cases, it is

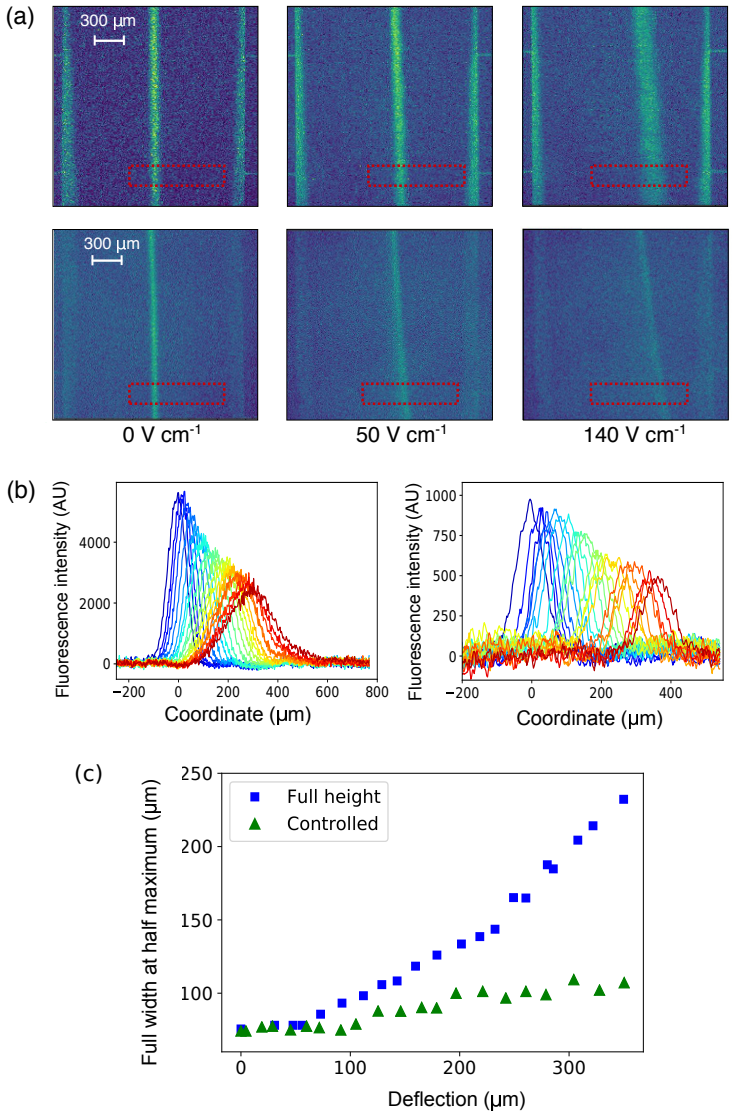

Fig. 4.12 **(a)** The profile of the analyte stream in the separation chamber with the sample (bovine serum albumin) injected across the full height of the chamber (2D chip; top row) and when its injection was restricted to the central area (3D chip; bottom row). The walls of the electrophoresis chamber are defined by the fluorescent interface on the sides which carries the conductive electrolyte solution. **(b)** The intensity profiles across the red rectangular section shown in panel **(a)** for the 2D (left) and the 3D (right) chip when increasing the field strength linearly from 0 V cm^{-1} (blue) to 140 $V\ cm^{-1}$ (red). **(c)** The broadening of the analyte stream was observed to be much less significant when the injection was restricted to central areas only - specifically, at the largest deflection studied the relative broadening was found to be around five-fold smaller $235\mu\text{m} - 75\mu\text{m} = 160\mu\text{m}$ vs $105\mu\text{m} - 75\mu\text{m} = 30\mu\text{m}$).

only the broadening extent which determines the effective resolution of the separation process. This opens up the possibility to use micron scale separation devices for both, resolving a large number of components from one another and resolving mixtures which include components with very similar electrophoretic mobility values. The strategy of controlling sample injection only to areas where the distributions in the velocity gradients are the smallest can be used to similarly increase the achievable resolutions of separation approaches using strategies other than electric field for the separation, such as magnetic, diffusive or thermal fields.

4.4 Conclusion

In this chapter, I addressed two challenges at the core of micron scale separation processes. I first developed a strategy for integrating strong electric fields with micron scale that can be applied in a stable and quantitative manner to achieve separation of individual proteins as well as protein complexes. I then developed a strategy for substantially increasing the resolution limits of micron scale separation approaches, enabling almost all of the broadening effect encountered in conventional setups to be suppressed. The latter development is expected to be of particularly great interest for the micron scale separation community due to the substantial advancement that it facilitates through a relatively straightforward design modification. Notably, the devices described in this Chapter have all their structures defined lithographically, facilitating their reproducible production through readily scalable fabrication strategies.

Chapter 5

An integrated protein separation and analysis system

This Chapter is based on the following publication:
Saar KL et al., "Rapid two-dimensional characterisation of proteins in solution", accepted.

5.1 Motivation

As described in the Introduction, microfluidic platforms are attractive for the analysis of biological samples because of their very low sample consumption and high recovery rate [94–98]. Notably, microfluidic platforms can provide unsurpassed analysis speeds both on the level of individual unit operations as well as on the level of a combined workflow as several functional units can be integrated directly without the requirement for transferring the sample between the units or for integrating connector elements or tubes - such transfer processes do not only extend the process but also introduce dispersion, thereby affecting the performance of the system.

A crucial step in any workflow that involves working with non-homogenous mixtures is the separation of components of interest, either to reduce the complexity of the mixture before it is directed to further processing or to purify it. As far as combined on-chip separation and analysis is concerned, continuous separation techniques are considered a particularly attractive route to performing the fractionation as they allow separating analytes in the direction that is perpendicular to their flow, thereby separating them spatially. This is in contrast to batch separation techniques, such as capillary electrophoresis where the analytes move in the same direction as the applied field, allowing their separation in time rather than space. Although such batch separation approaches have be integrated with further processing [100, 198, 199], their discontinuous operation limits the range and the complexity

of downstream steps that can be performed due to the limited time that each fraction spends in the analysis area before the arrival of the next fraction.

Whereas an array of methods has been developed for detecting the separated analytes on chip, including both optical and electrochemical strategies [200–206], these readings can be transferred to concentrations only in the presence of prior knowledge about the detected components. As such, the uses of these detection techniques have remained limited to applications where the analytes in each specific fraction are known or where their identities are determined subsequently with an offline technique. Integration of separation and direct on-chip analysis into a platform that in addition to detection would also characterise the separated fractions has been seldom achieved. For instance, the possibility to simultaneously determine the isoelectric points and concentrations of separated molecules has been demonstrated [206]. However, this result was achieved through the inclusion of intrinsic calibration markers rather than through the integration of an analytical step, not serving as a general strategy for combined on-chip fractionation and analysis.

Indeed, with conventional on-chip separation approaches, analytical information on the separated components is usually obtained by an offline analysis and identification strategy, most notably mass spectrometry [207–209] or SDS-PAGE analysis [192]. However, such off-line analysis approaches eliminate one of the most attractive advantages of microfluidic technologies - its fast processing speed - and hence limits the applications of the platform to systems which are either static or only slowly evolving. In this Chapter, I demonstrate a microfluidic device that overcomes this limitation of current analysis approaches and combines onto a single chip a separative and an analytical step. Specifically, I use the continuous separation strategy described and developed in Chapter 4 and a previously described on-chip sizing approach [36]. In addition to enhancing the resolution of the analytical sizing technique, the device enabled me to rapidly construct two-dimensional characteristic maps of the biomolecular mixtures directly in solution.

5.2 Integrated on-chip separation and analysis

In order to integrate onto a single platform a preparative and an analytical step that can characterise and potentially identify the separated fractions, I used a separation strategy where the fractionation occurred continuously, which unlike batch separation approaches permit a tight control over the time intervals at which new fractions interface the analysis area [210]. Of the different modes of electric field mediated continuous separation strategies [166, 182], free flow zone separation stands out in particular, as it provides an option to direct specific

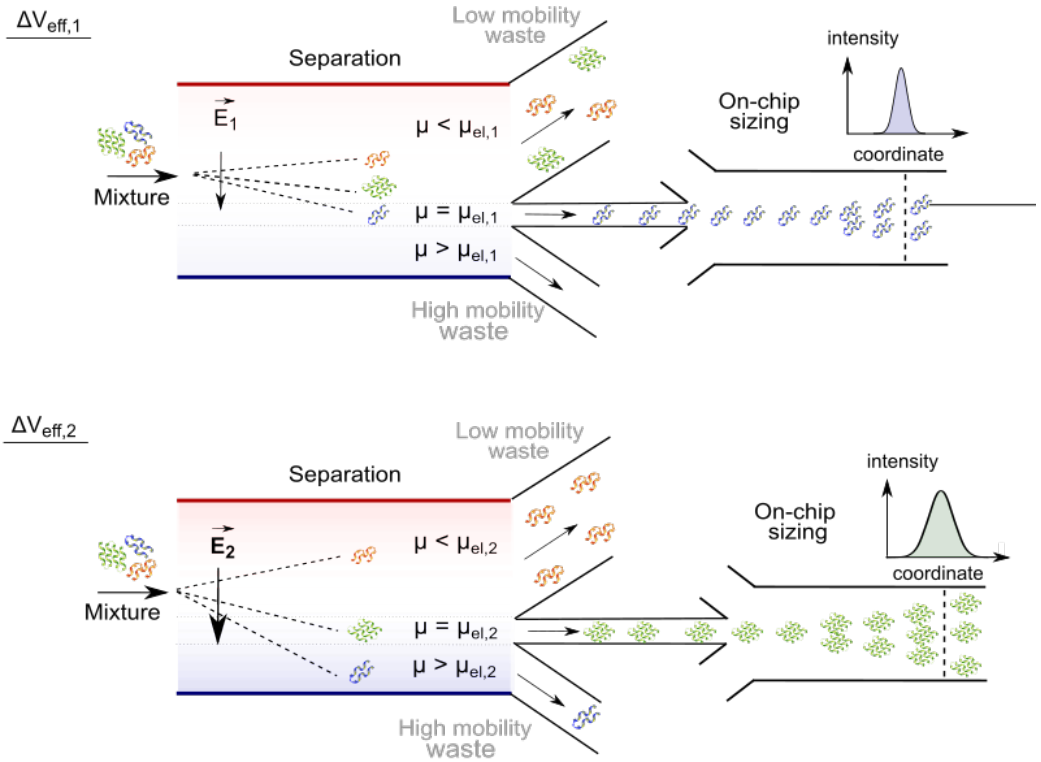

Fig. 5.1 On-chip separation and analysis of mixtures in liquid phase. By adjusting the effective voltage ΔV_{eff}, molecules of a specific electrophoretic mobility, $\mu = \mu_{\text{el}}$, and hence of a specific $\frac{q}{R_h}$ ratio can be directed to the analysis area with those of smaller ($\mu < \mu_{\text{el}}$) and larger ($\mu > \mu_{\text{el}}$) mobility values directed to the waste collection channels. As the applied voltage can be varied, only a single analysis unit is required and the width of the separation chamber can be kept constrained, allowing the device to retain a high voltage efficiency and a fast processing speed. In the analysis area, the fractions are sized through microfluidic diffusional sizing (MDS) by monitoring their spatiotemporal motion under laminar flow conditions.

fractions to analysis by simply adjusting the applied field strength. This is in contrast to operational modes where a fixed gradient, such as pH (free flow isoelectric focusing) or buffer mobility (free flow isotachophoresis) is applied across the separation channel - with these techniques, the separation can be performed continuously but in order to analyse the separated fractions, a separate processing unit is required for each fraction. Moreover, a continuous separation approach where the field strength can be varied - such as free flow zone separation as employed in this work - does not require separating the components out simultaneously. Instead, by adjusting the field strength, fractions can be directed to the analysis sequentially (Figure 5.1). This enables keeping the width of the separation channel constrained which facilitates both, narrower devices and hence faster processing speeds and the integration of stronger fields without increasing the applied potential.

Specifically, to develop a microscale device where the preparative and the analytical step occur on a single chip, I used the free flow zone electrophoresis approach described in Chapter 4 to fractionate analytes. By varying the applied voltage, ΔV, this module directed fractions of a defined electrophoretic mobility, μ_{el}, to the analysis unit (Figure 5.1) [211]. The analytical sizing step for each of the fractions was performed by monitoring the tempo-spatial movement of the molecules under flow which, due to the laminar nature of the flow, could be directly linked to their diffusion coefficients [36]. This allows to a certain degree identifying the fractions that come out from the separation module, similarly to SEC-MALS (size exclusion chromatography with multi-angle light scattering).

In addition to enhancing the resolution of the sizing technique, owing to the quantitative nature of the electrophoresis unit, this device further enabled me to construct two-dimensional characteristic maps of the native charges and the hydrodynamic radii of the analytes - much like what could be obtained with two-dimensional electrophoresis gels. However, as the electrophoretic separation step was performed in aqueous environment the devices ensured that firstly, the two-dimensional map was obtained in the order of a few minutes which is orders of magnitude faster time-scale than what could be reached with conventional and non-aqueous phase based techniques, opening up the possibility to study not only static but also dynamic systems. Secondly, the mixture was analysed in an environment where the molecules were not affected by the presence of the support medium, which unlike gel based methods permits the study of weak and non-covalent interactions that are affected by the support medium. As such, this device opens up the possibility of multidimensional characterisation of biological mixtures directly in solution and at time-scales that unlike conventional platforms, enable exploring dynamic processes.

5.3 Results

5.3.1 Device design

The device involved a native phase quantitative electrophoresis unit connected in series with a microfluidic diffusional sizing (MDS) unit (Figure 5.2) [36]. This combined platform directs a component of a specific electrophoretic mobility, μ_{el}, to on-chip downstream analysis as a function of the applied electric field strength. The device was designed such that with no field applied across the separation unit, none of the sample molecules flowed into the analysis area. This objective was achieved by designing the three channels downstream of the electrophoresis unit ("low mobility waste", "analysis", and "high mobility waste") to have different hydraulic resistances with ca. 63% of the flow directed towards the "low mobility waste" channel, around 5% to the analysis area and the rest to the "high mobility waste" channel.

In order to facilitate device operation in a stable manner and as a result allow quantitative characterisation of the samples, I set out to minimise the number of individual units that drove the flow in the device. For this purpose, the outlets from individual channels were combined such that a single syringe could be used to apply a negative pressure at its outlet (Figure 5.2) - this ensured that the flow in the individual channels was defined by the hydraulic resistances of the lithographically produced high-accuracy channels, in contrast to a system where the flows would be controlled by a number of external syringe pumps which could lead to relative fluctuations between the flows of the different fluids over time.

The outlets of the electrolyte solution, however, were kept separated from the combined device outlet to (i) allow applying electric potential across the device without generating an electrical short-circuit and (ii) enable efficient removal of any generated electrolysis products without them accumulating and causing pressure fluctuations or cavitation at the joint outlet where the negative pressure was applied. Specifically, as described in Chapter 4, the electric potential was applied on metallic connectors outside the chip - this ensured that all gaseous products were generated on the metal and fluid interface outside the chip and not inside the microfluidic channels. The flowing liquid electrolyte solution further ensured that the generated electrolysis products were flowed away from the chip while the applied field was propagated back to the chip instantaneously.

The flow of the electrolyte to the electrophoresis chamber was controlled by narrow perpendicular channels ("bridges"; Figure 5.2) connecting the electrolyte channels to the electrophoresis area. These channels provided high hydrodynamic resistivity preventing the oppositely charged electrode solutions from coming into contact with each another while still allowing

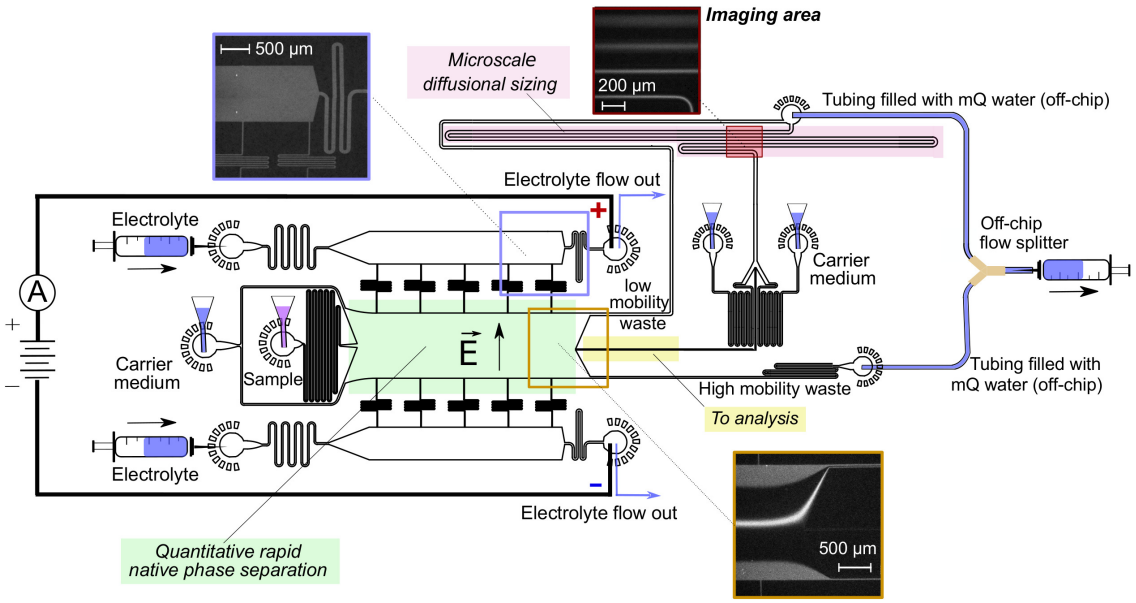

Fig. 5.2 Device design and operation. A free flow electrophoresis unit (green), allowing rapid separation of analyte molecules in their native phase and yielding quantitative information on the separation process, directed fractions of the sample (yellow) to a downstream analysis process involving microfluidic diffusional sizing (MDS; pink). The sample was characterised by monitoring a single imaging frame (top right inset) to simultaneously extract the sizes and the charges of the separated fractions. The device was operated by applying a negative pressure at its outlet with a Y-shaped off-chip flow splitter keeping the solutions from the "low mobility waste" and "high mobility waste" channels separated to avoid partial short circuiting of the device. The electric potential was applied from the electrolyte solution outlets employing a flowing electrolyte solution as described previously. The flow of the electrolyte solution, which included a fluorescent tracer of 1 mg mL^{-1} BSA for its visualisation, was chosen such that the electrolyte would reach its outlet rather than be withdrawn into the separation chamber without reaching it (top left inset), yet it would leak into the chamber by a controlled distance, leaving sufficient space for deflecting the sample beam (bottom inset).

some of the electrolyte to flow to the electrophoresis area and through this provide direct fluidic and hence electrical connectivity between the electrophoresis chamber and the electrolyte channels. To maximise the efficiency of the electric field, I required these channels to have a high hydraulic resistance $\mathrm{R_{HD}}$ per electrical resistance $\mathrm{R_{EL}}$:

$$\frac{\mathrm{R_{HD}}}{\mathrm{R_{EL}}} = \frac{\alpha(\gamma) \cdot \mathrm{R^*_{HD}}}{\rho_{\mathrm{el}} \cdot \frac{\mathrm{L}}{\mathrm{A}}} \tag{5.1}$$

where ρ_{el} is the resistivity of the electrolyte and $R^*_{HD} = \frac{\eta L}{A^2}$ is the hydraulic resistance of the channel depending on the viscosity of the fluid in it, η, its length, L, and on its cross-sectional area, A. The geometrical correction factor, $\alpha(\gamma)$, is defined as a function of the aspect ratio of the channel $\gamma = \frac{\mathrm{w}}{\mathrm{h}}$ as $\alpha = \frac{\pi^3}{8}\ \gamma^2\ \mathrm{f}(\gamma)$ with w and h being the width and the height of the channel [183]. After substitution and simplification, I obtain:

$$\frac{\mathrm{R_{HD}}}{\mathrm{R_{EL}}} = \frac{\pi^3 \eta}{8 \rho_{\mathrm{EL}}\ \mathrm{h}^2}\ \gamma\ \mathrm{f}(\gamma) \tag{5.2}$$

With the height of the channel being fixed by the requirement for collecting a sufficient amount of signal for imaging (it was set to $\mathrm{h} = 50\ \mu\mathrm{m}$), equation 5.2 is maximised when $\gamma\ \mathrm{f}(\gamma)$ is maximised. Specifically, for a rectangular channel, the correction factor $\mathrm{f}(\gamma)$ has been approximated as [183]

$$\mathrm{f}(\gamma) = \left[\sum_{\mathrm{n}=1,3,5\ldots}^{\infty} \frac{\mathrm{n}\gamma}{\pi \mathrm{n}^5} - \frac{2}{\pi^2 \mathrm{n}^5} \tanh(\mathrm{n}\gamma\pi) \right]^{-1} \tag{5.3}$$

Thus, from equations (5.2) and (5.3), I realised that the bridges achieve a maximal hydraulic per electrical resistance value in the limit of $\gamma \to 0$. Due to fabrication of lithographic channels becoming challenging at aspect ratios greater than around 4-5, I fixed the width of the connecting channels to $\mathrm{w} = 18\ \mu\mathrm{m}$.

I noted that during the operation of the device, the small amount of electrolyte solution that was designed to flow to the electrophoresis channel and generate a wall at the edges of the chamber (Figure 5.2, bottom inset) ultimately reached the combined outlet, bringing the two oppositely charged electrolyte solutions into contact with one another, thereby reducing the potential across the electrophoresis chamber. In order to circumvent such partial short circuiting, I used a Y-shaped flow splitter to prevent the oppositely charged electrolyte streams coming into contact with each other at the device outlet but only further downstream where they reached the splitter (Figure 5.2). Crucially, the tubing connecting the two streams

was filled with distilled water (18 MΩ cm^{-1}). Its length on each side of the Y-shaped splitter was L = 40 cm and internal diameter d_{ID} = 0.86 mm. With the flow rates of the solutions into the two sides being around 320 μL h^{-1} and 80 μL h^{-1} as estimated in Section 5.3.2, it would therefore take around

$$t = \frac{\pi \cdot (\frac{d_{ID}}{2})^2}{Q} \tag{5.4}$$

t_1 = 43 min and t_2 = 170 min for the fluid to reach the flow splitter from the two sides. Even when accounting for Taylor dispersion in the tubing, this time scale is significantly longer than the imaging period ($\sim$ 5 minutes) and as such the voltage efficiency of the device can be assumed to remain unaffected throughout its operation.

5.3.2 Fluid flow in the device

The device was designed such that at the end of the electrophoresis chamber the fluids would split in a 1:12:2 ratio (63%, 5%, 32%) ensuring that no sample molecules flowed to the analysis area when no electric potential was applied across the separation chamber. Furthermore, the sample flow to the electrophoresis unit was designed to be in around 1:25 ratio with the carrier medium and in around 1:10 ratio in the diffusional sizing unit. The "bridges" between the electrophoresis area and the electrolyte channels were designed such that the device would retain as high voltage efficiency as possible while the flow of the electrolyte into the separation area would be minimised, leaving as much area as possible available for the separation process (equation 5.1).

The flow rates in each of the individual channels were estimated by solving a set of simultaneous equations:

$$Q_{cm} + Q_s + 2 \cdot Q_d + 2 \cdot Q_{el,in} = Q_{out} + 2 \cdot Q_{el,out} \tag{5.5}$$

$$2 \cdot Q_d + Q_{lm} + Q_a + Q_{hm} = Q_{out} \tag{5.6}$$

$$2 \cdot Q_d + Q_a = Q_{sizing} \tag{5.7}$$

$$R_{cm} \cdot Q_{cm} = R_s \cdot Q_s \tag{5.8}$$

$$R_{bridge} \cdot \frac{(Q_{el,in} - Q_{el,out})}{N} = R_{el,out} \cdot Q_{el,out} + R_{cm} \cdot Q_{cm} \tag{5.9}$$

$$R_{lm} \cdot Q_{lm} = R_{hm} \cdot Q_{h,} \tag{5.10}$$

$$R_{lm} \cdot Q_{lm} = R_a \cdot Q_a + R_{sizing} \cdot Q_{sizing} \tag{5.11}$$

$$R_{cm} \cdot Q_{cm} + R_a \cdot Q_a = \frac{1}{2} R_d \cdot Q_d \tag{5.12}$$

where Q_i and R_i correspond to the flow rate in channel i and to the hydraulic resistance of that channel, respectively, as indicated in Figure 5.3a. Equations 5.5 - 5.7 describe the

mass balances for the total device, for the analysis area downstream of the separation unit and for the diffusional sizing unit, respectively; equations 5.8 - 5.9 equate the pressure drop between points A and B; equations 5.10 - 5.11 the pressure drop between points B and D and equation 5.12 the pressure drop between points A and C. With the total withdrawal flow rate from the device outlet set to $Q_{out} = 500$ μL h^{-1} and the electrolyte infusion rate to $Q_{el,in} = 80$ μL h^{-1}), the corresponding flow rates in each of the channels estimated by solving the system of equations 5.5 - 5.12 are summarised in Table 5.1.

The microfabrication process that I used for producing the devices (Section 2.1.1) can be estimated to be accurate to within a few micrometres with uncertainties originating from printing of the acetate film transparencies as well as the fabrication process itself due to effects such as the crosslinking reaction proceeding further than the UV illuminated area and some of the cross-linked photoresist being edged away during the development step (Figure 2.1b,c). As such, the dominant sources of errors in the calculations (equations 5.5 - 5.12) were the uncertainties in the width of the electrolyte bridges and in the width of the channel that transferred the sample to analysis (Table 5.1). I assumed there to be a 2 μm error in the widths of these two channels. Using these estimates, I calculated the flow rates in each of the channels for all the individual scenarios by similarly solving the system of equations 5.5 - 5.12. The two critical flow rates that affect the quantitative analysis in the following sections of this Chapter are the flow rate in the diffusional sizing channel (Section 5.3.4) and in the electrophoresis chamber (Section 5.3.5). In particular, the calculations predicted the combined flow of the carrier medium and the sample to vary between 184 and 204 μL h^{-1} in the electrophoresis chamber and between 142 and 145 μL h^{-1} in the diffusional sizing channel to vary, indicating around 5% and 1.3% relative errors in these flow rates.

I observed that the flow rate of the electrolyte into the device had a notable effect on the device performance. On the one hand, when the electrolyte infusion rate was low, the electrolyte solution gets withdrawn into the main chamber without reaching its outlet (Figure 5.3b), which can generate a reversed flow from the electrolyte outlet back to the electrolyte channel, ultimately resulting in some of the electrolysis products entering the chip. Indeed, at electrolyte infusion rate of $Q_{el,in} = 30$ μL h^{-1}, by solving the system of equations 5.5 - 5.12, I estimated the flow at the electrolyte outlet channel to be $Q_{el,out} = -10$ μL h^{-1}. On the other hand, when the electrolyte flow into the system was high, the electrolyte solution leaks far into the separation channel. Specifically, at the infusion rate of $Q_{el,in} = 200$ μL h^{-1}, again by solving the system of equations, I estimated that the electrolyte leaks in from all the bridges at a rate of $Q_{bridge} = 25$ μL h^{-1} or at a total rate of around 250 μL h^{-1}. Under these conditions the combined flow of the carrier medium and the sample into the electrophoresis chamber is $Q_{cm} + Q_s = (201 + 8)$ μL h^{-1} = 209 μL h^{-1}, indicating that over half of the separation chamber is filled with the electrolyte (Figure 5.3c). At sufficiently high

Table 5.1 The flow rates of the solutions in the channels of the device with the withdrawal flow rate from the device outlet being $Q_{out} = 500$ μL h^{-1} and the electrolyte infusion rate into the device being $Q_{el,in} = 80$ μL h^{-1}.

Channel	**Symbol**	**Width** (μm)	**Length** (mm)	**Pressure drop** (Pa)	**Flow rate** (μL h^{-1})
Carrier medium to the electrophoresis unit	Q_{cm}	50	5.1*	603	188*
Sample	Q_s	40	40.5	603	7.4
Carrier medium to the sizing unit	Q_d	50	8.6*	730	135
Low mobility waste	Q_{lm}	60	10.2	1561	172
High mobility waste	Q_{hm}	50	15.5	1561	80
To analysis	Q_a	30	2.5	128	13
Diffusional sizing channel	Q_{sizing}	100	25.0	1432	148
Electrolyte out	$Q_{el,out}$	60	4.5	101	25
Bridge	Q_{bridge}	18	6.9	704	7

* Two parallel channels of that length. The flow rate is given as the combined flow rate from the two channels.

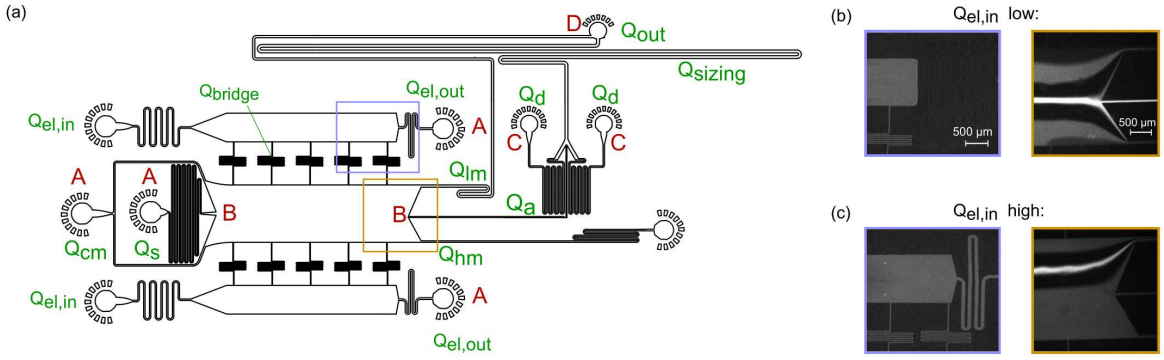

Fig. 5.3 Flow in the combined separation and analysis device. **(a)** The flow rates in each of the channels were estimated by solving the system of simultaneous equations 5.5 - 5.12. **(b)** At low relative electrolyte flows (Q_{out} = 500 μL h^{-1}, $Q_{el,in}$ = 30 μL h^{-1}) the electrolyte solution was observed not to reach the electrolyte outlet (left) but to get withdrawn into the separation chamber, not enabling the propagation of the electric potential from the electrolyte outlet back to the device (right). **(c)** At high relative electrolyte flows (Q_{out} = 500 μL h^{-1}, $Q_{el,in}$ = 200 μL h^{-1}) the electrolyte reached its outlet (left) but leaked too far into the separation chamber to permit directing the sample molecules into the analysis area (right). The individual flows are summarised in Table 5.1.

flows, however, the electrolyte reached its outlet (Figure 5.2, top inset) and generated thin stable walls at the electrophoresis chamber walls (bottom inset) as desired. This infusion rate was chosen for all further experiments.

5.3.3 On-chip microfluidic diffusional sizing (MDS)

The separation unit directed a fraction of the fluid flow to a microfluidic diffusional sizing unit (MDS) which similarly to analytical light scattering setups connected to size exclusion columns (SEC-MALS) allowed to a certain extent the identification of the fractions leaving the separation module. The diffusional sizing process relied on surrounding the analyte molecules with carrier medium and monitoring their diffusion into the medium in space and in time as described earlier [36]. As the sizing measurement had to performed for all applied voltages separately (Figure 5.4a-b), I adjusted the strategy from recording the profiles at 12 different locations to recording them at 4 locations, and reduced the channel width to ensure that only a single image would be sufficient for performing the sizing analysis (Figure 5.2, red highlighted area). Moreover, to analyse the data and obtain the average molecular size for each of the voltages, I replaced the Langevin dynamics based code used to model the movement of individual particles in the microfluidic channels [194] with a numerical

solver that enabled the predicted particle distributions to be generated significantly faster. These predicted distributions were then, as before, compared to the experimental data to extract the hydrodynamic radii of the particles in each of the fractions.

The positions of the four locations used for imaging (Figure 5.4b) were chosen such that the first one would be as close as possible to the nozzle where the sample meets the carrier medium - this placement allowed its usage as a reference point from which the movement of the particles was propagated. The position of the furthest away point was chosen such that for a representative protein with $R_h = 3$ nm ($D = 7 \cdot 10^{-11}$ m^2 s^{-1}), the molecules would have diffused away from the centre of the channel but would have not yet become uniformly distributed across it - such placement enabled maximising the amount of information that could be extracted from the profiles. To enable accurate sizing of analyte molecules that are orders of magnitudes larger or smaller in size, the length of the diffusional sizing channel or the flow rate can be adjusted accordingly. Last but not least, in order to eliminate any effect from the autofluorescence of the PDMS in the UV-wavelength, a background image with no sample flowing in the device was also recorded and subtracted from the data before the images were analysed.

5.3.4 Analysis of a binary protein mixture

I used the device to analyse a binary mixture of two sample proteins - bovine serum albumin (BSA) and human lysozyme. In order to preserve the protein molecules in their native states and enable a label-free analysis of the sample, the imaging was performed with a home-built UV-wavelength based microscope that relied on recording the intrinsic fluorescence of the sample by exciting their tryptophan and tyrosine residues (Materials and Methods). I first confirmed the ability to separate the mixture into its components by applying a set of voltages and recording the fluorescent profiles (Figure 5.4). I then operated the device by applying a voltage ramp from -75 V to 75 V and instead of the separation area, recorded the profiles downstream at the diffusional sizing area containing four sections of the channel as described in Section 3.3. To precisely locate the imaging position the images were recorded at a position where the corner of the first channel would be visible (Figure 5.2, top right inset; Figure 5.4b) but only the part of the frame where the channels appeared straight was used for the sizing analysis. The best fits to the individual profiles were used to extract the hydrodynamic radii at each of the voltages (Figure 5.4c) and were found to be around 1.9 nm (at -20 V) and 3.6 nm (at 30 V). By noting that the obtained diffusion coefficient depends on the diffused distance, the fluid flow rate and the channel dimensions as $D \sim \frac{x_{diff}^2}{t_{res}} = x_{diff}^2 \frac{Q}{w \cdot h \cdot L}$, the relative error in the diffusion coefficient and, hence, also in the hydrodynamic radii can be estimated as:

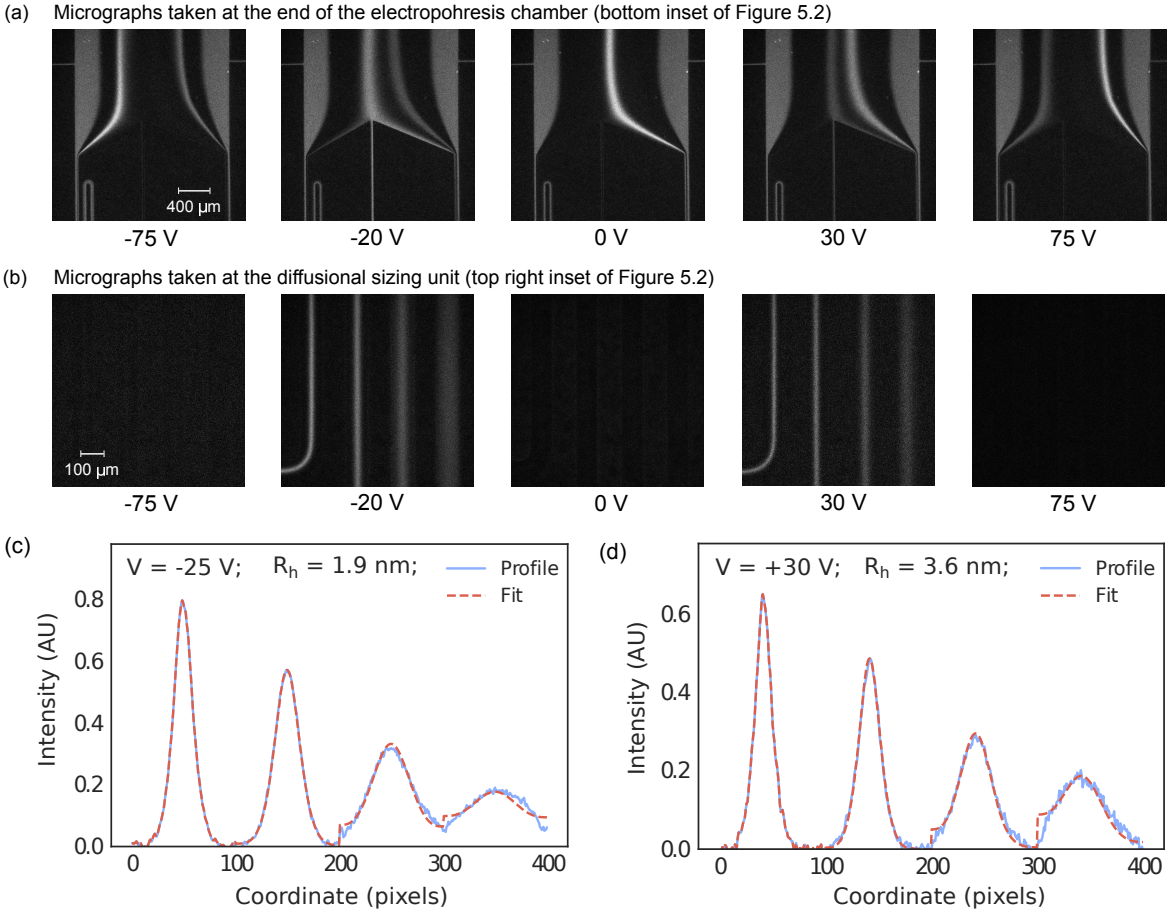

Fig. 5.4 Operation of the combined separation and analysis device. **(a)** The voltage applied across the electrophoresis chamber (Figure 5.2, bottom inset) was adjusted in linear steps to direct specific fractions to the analysis area. **(b)** The fractions were then sized by imaging the diffusional sizing unit (Figure 5.2, top right inset) consisting of four channels in which the extent of the diffusion of the analyte molecules into their surrounding carrier buffer was monitored. **(c)** The latter images were used to find the average size of the analyte molecules in each of the fractions by fitting the observed fluorescent profiles for different hydrodynamic radii (R_h) and minimising the least mean square error between the fit (red dotted line) and the data (blue continuous line).

$$\begin{aligned}\left(\frac{\Delta D}{D}\right)^2 &= 2\left(\frac{\Delta x_{diff}}{x_{diff}}\right)^2 + \left(\frac{\Delta w}{w}\right)^2 + \left(\frac{\Delta h}{h}\right)^2 + \left(\frac{\Delta L}{L}\right)^2 + \left(\frac{\Delta Q}{Q}\right)^2 \\ &\approx \left(\frac{2\ \mu m}{100\ \mu m}\right)^2 + \left(\frac{2\ \mu m}{100\ \mu m}\right)^2 + 0.014^2 = 0.031^2\end{aligned} \tag{5.13}$$

where the error in measuring the diffused distance from the micrographs was assumed to be minimal, the height (determined by a profilometer; Section 2.1.1), the width of the channel were estimated to have an error of 2 μm and the uncertainty in the flow rate was derived from the uncertainties in the channel dimensions (Section 5.3.2). The obtained values are in agreement with the values obtained by using dynamic lights scattering (DLS). The total fluorescent intensities across the imaging area and the recorded hydrodynamic radii as a function of the applied electric potential across the separation channel are shown in Figure 5.5a. Crucially, the extracted size was robust and was not affected by the intensity and the concentration of the molecules in the analysis area.

The characterisation of mixtures which include molecules of similar properties is known to be challenging because it requires deconvolution of an average signal, which is a difficult inverse problem [36, 212]. As such, polydisperse mixtures are commonly analysed by first physically separating the individual components within a mixture, for instance, by gel filtration or another chromatographic method, and only then detecting and sizing the individual fractionated species, for example, by absorbance or by light scattering. Indeed, when examining the mixture of bovine serum albumin and lysozyme using DLS, the presence of averagely sized molecules rather than that of the individual species was observed (Figure 5.5b, light blue dashed line). Microfluidic diffusional sizing has been shown to improve on the deconvolution capability of signals and through this enhance the resolution at which mixtures can be characterised because it acquires data both in space and in time and thus increases the accessible information content [36]. Its performance, however, has been shown to also become limited when the analytes do not exhibit a few fold difference in their sizes [36], which in biological mixtures occurs only for specifically chosen samples but not for mixtures that include similarly sized proteins [16, 37, 38].

Mixtures of nanoscale molecules where the individual analytes are of similar size but exhibit differences in their electrophoretic properties, can be rapidly characterised using the device described here (Figure 5.5b, dark blue continuous line). Whereas a similar result could have been obtained using an off-chip separation approach, the latter strategy would have introduced the requirement for transferring the sample from one analytical tool to another or required the integration of connector elements or tubes and could have thus been performed

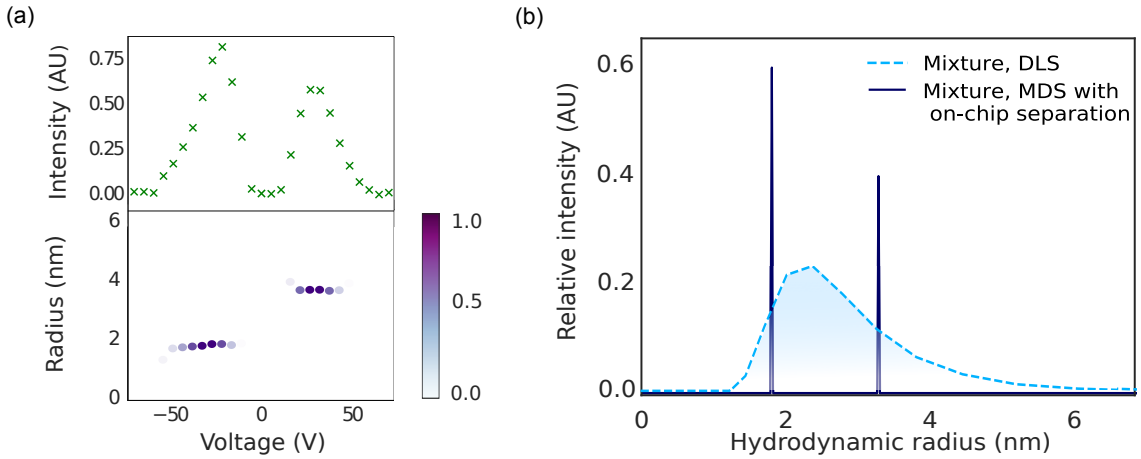

Fig. 5.5 Sizing of a mixture that could not be deconvoluted using standard sizing techniques. **(a)** The sizes of the components in a binary mixture of lysozyme and bovine serum albumin were found to be $R_h = 1.9$ nm and $R_h = 3.6$ nm. The obtained sizes were robust and not affected by the fluorescence intensity and the concentration of the molecules in the analysis area. **(b)** This binary mixture could not be characterised using sizing techniques that do not involve pre-fractionation steps, such as dynamic light scattering (DLS; light blue dotted line). Accurate size resolution became possible using the combined microfluidic diffusional sizing and free flow fractionation platform described here (dark blue continuous line).

only over a significantly longer timescale.

5.3.5 Two-dimensional characteristic maps of protein mixtures

In order to extract quantitative information from the separation step and specifically, to relate the applied potentials to the electrophoretic mobilities of the species that were directed to the analysis area at this voltage, I set out to estimate the voltage efficiency of the device. Concurrently with the imaging, I recorded the current flowing in the device at each of the voltages (Materials and Methods) and from these data, I estimated the resistance of the device to be $R_{device} = 644$ kΩ. I then short-circuited the separation chamber by flowing a highly conductive media in it and found the resistance of the electrodes to be $R_{electrodes} = 521$ kΩ, indicating a 14% voltage efficiency.

The movement of a particle in electric field can be related to its electrophoretic mobility though $\mu_{el} = \frac{v_{drift}}{E}$, where v_{drift} is the drift velocity of the analyte in the electrophoresis chamber and E the strength of the electric field across the chamber. I noted that the electric field applied here across the channel varied slightly as a function of the distance along the electrophoresis chamber due to the additional amount of electrolyte that flowed in from the

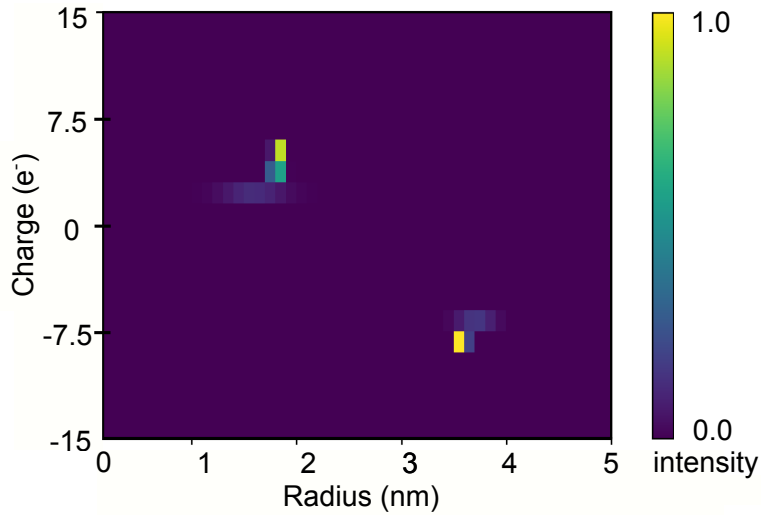

Fig. 5.6 Rapid two-dimensional characterisation of a mixture of bovine serum albumin and human lysozyme. The quantitative nature of the electrophoretic separation unit allowed the applied potential to be related to the electrophoretic mobility μ_{el} of each of the fractions. These data were used in combination with the extracted hydrodynamic radii (R_h) to estimate the effective charges (q) of the molecules in each of the fractions and to construct a two-dimensional q vs R_h map of the mixture over a few minute timescale by monitoring the device only at a single imaging frame.

side channels, slightly decreasing the effective separation between the two electrodes. Under these circumstances the electrophoretic mobility can be expressed as

$$\mu_{el} = \frac{v_{drift}}{E} = \frac{\frac{\delta}{t_{res}}}{\frac{V_{eff}}{w}} = \frac{\delta \cdot Q \cdot w}{(w \cdot h \cdot L) \cdot V_{eff}} = \frac{\delta \cdot Q}{h \cdot L \cdot V_{eff}} \tag{5.14}$$

where V_{eff} is the effective voltage across the separation chamber, δ is the observed deflection and Q is the flow rate in the separation area (the sum of the carrier medium flow Q_{cm} and the sample flow Q_s). As described, the device used in this work was designed such that the molecules observed in the analysis area were those deflected away from their original position by around 15% of the total width of the separation chamber or by around 300 μm. The dominant contributors to the error in the electrophoretic mobility were the uncertainties in the flow rate and in the voltage efficiency, which I estimated to be around 5% (Section 5.3.2) and 9% (Section 4.2.3), respectively, leading to around $0.09^2 + 0.05^2 = 0.103^2$ or around 10% error in the electrophoretic mobility value.

Using equation 5.14 to estimate the electrophoretic mobilities of each of the fractions and by combining these data with the estimates that I had previously obtained for the diffusion

coefficients for these fractions (Figure 5.4c-d), the electrophoretic mobilities of each of the fractions could be directly converted to the native charges of the molecules in this fraction using the Einstein relation $\mu_{\mathrm{el}} = \frac{\mathrm{q}}{\mathrm{kT}}\mathrm{D}$.

Based on these data, I constructed a two-dimensional characteristic map of the effective charge (q) and hydrodynamic radius ($\mathrm{R_h}$) of the mixture (Figure 5.6). The native charges of the bovine serum albumin and the lysozyme molecules can be seen to be around -9 and $+6$ elementary charge units, respectively, which are in agreement with the values estimated using other techniques [186, 187, 213, 214]. The uncertainties in these obtained charge values can be estimated from the Einstein relationship as around 11%:

$$\left(\frac{\Delta \mathrm{q}}{\mathrm{q}}\right)^2 = \left(\frac{\Delta \mu_{\mathrm{elph}}}{\mu_{\mathrm{elph}}}\right)^2 + \left(\frac{\Delta R_h}{R_h}\right)^2 = 0.031^2 + 0.103^2 = 0.108^2 \tag{5.15}$$

Crucially, the full two-dimensional map was obtained from monitoring only a single imaging frame, using only 4 μL sample. Depending on the desired resolution, such map can be constructed in a time period of around a few minutes, generating the basis for performing rapid two-dimensional characterisation of mixtures directly in their native phase - this time scale is orders of magnitude faster than what is required for running conventional two-dimensional protein gels.

5.4 Conclusion

Current microscale on-chip separation approaches commonly rely on collecting the separated fractions and sending these to offline processing rather than analysing them directly on chip. This undermines one of the key advantages of microscale platforms - their fast analysis speed - and may also introduce the requirement for additional fluid handling steps. I demonstrated a microfluidic device that combines on-chip separation with direct on-chip analysis - spatiotemporal diffusional sizing. By sizing a binary mixture of proteins that cannot be characterised by existing solution sizing approaches, I showed that the device extensively enhances the analytical power of the downstream analytical technique. Moreover, due to the quantitative nature of the separation process, the device further allowed me to construct a two-dimensional characteristic map of a heterogeneous mixture on a few minute timescale, opening up the possibility of rapidly characterising mixtures directly in solution and at time resolutions not accessible with current biophysical techniques.

Chapter 6

A high throughput platform for detecting protein inside individual cells

6.1 Motivation

Cells are fundamental units of life with each unit being unique. Conventional bulk scale biophysical and biochemical analysis techniques allow accessing only population averaged parameters, which give a fundamentally incomplete picture for describing what is happening on the level of an individual cell, especially because functionally key cells are often present in small numbers [83–85]. Although a range of experimental techniques has been developed to describe the content and behaviour of individual cells, until recently, the majority of these approaches have not permitted performing measurements at throughputs where they would yield statistically significant system wide data [215].

Microdroplets platform [106–108] - involving the formation and manipulation of microscale compartments - has opened up the possibility to increase extensively the throughput of biochemical analysis and of single cell studies in particular. Indeed, analysing the transcriptomes of individual cells has enabled innovative discoveries in areas ranging from developmental biology to immunotherapy and cancer biology [86–91]. Such approaches have largely relied on the use of DNA sequences that encode the cellular identities of molecules into oligonucleotide codes, so that after the contents of individual cells have been barcoded inside compartmentalised microdroplets, the proceeding analysis could be performed on a bulk scale [215–217].

The applications of such DNA barcoding strategies to date have predominantly been centred around analysing the transcriptomic content of cells. Here I aim to extend these approaches

and develop a platform that can instead describe the heterogeneity in protein expression between cells. Indeed, as described in the Introduction to this thesis, proteins are the chief acting molecules of biology and involved in the execution of almost every biochemical process occurring in cells. Whereas the synthesis of proteins is governed by messenger RNA (mRNA) molecules that are the transcripts for protein production, previous work has shown that mRNA and protein levels are correlated only in some cells due to factors, such as modulations in translational efficiency and in protein half-lives [218] and that mRNA abundance can, thus, not be used for the prediction of protein levels [219–222]. Moreover, tracking the protein content opens up the possibility to further gain insight into the post-translational modifications, including their signalling cascade activities as well as the into interactions between proteins - these phenomena cannot be trivially predicted from measuring the mRNA content only [221–223].

Profiling proteins in individual cells in a high throughput manner requires fast and sensitive analytical tools. Currently used tools for analysing proteins inside individual cells are limited in either their throughput, allowing only a small number of cells to be analysed in parallel, or in the multiplexing extent, limiting the number of targets that can be simultaneously monitored. Indeed, a widely popular cytometry based technique, fluorescence activated cell sorting, involving the use of differently coloured dyes allows sensitive fluorescence based detection to profile up to ten targets at a time [224, 225]. A more recently emerged cytometry time-of-flight technique, which replaces the fluorescent tags on antibodies with heavy metals and uses mass-spectrometer as the readout, can extend the multiplexing extent to a few hundred targets [226, 227]. While both of these approaches can, in principle, at least to some extent improve in their sensitivity and multiplexing capability, they are currently orders of magnitude away from reaching the characterisation of full cellular proteome, estimated be above 20,000 targets for human cells [228, 229].

6.2 High throughput single cell platform for analysing intracellular proteins

To overcome these limitations of current approaches for detecting and analysing proteins inside cells in a high throughput manner and develop an approach that would be virtually unlimited in its multiplexing extent, I used DNA sequences as a means to barcode the molecular identity of each protein. Crucially, using such a strategy, the devising of an effective barcoding strategy was no longer the limiting factor to detecting a large number of proteins simultaneously. For example, it can be estimated that only a ten bases long DNA sequence provides over $4^{10} \sim 10^6$ unique sequences, which is sufficient to barcode an antibody against

every epitope in the human proteome. Moreover, the number of each specific type of protein molecules inside individual cells is inherently small. Whereas no tools exist for amplifying the protein content of cells, oligonucleotide content can be rapidly increased by conventional molecular biology tools, such as polymerase chain reaction (PCR). Thus, such a strategy, relying on the use of DNA barcodes for detecting and quantifying the presence of proteins, ensures that even proteins that are present only at low concentrations can be detected. This possibility is in contrast with using dyes or heavy metal molecules for barcoding, which cannot be similarly amplified to achieve enhanced sensitivities.

The possibility to use DNA sequences for barcoding both the cellular and molecular identity of protein molecules has been demonstrated for cellular surface markers [228]. However, some of the very key proteins central to the onset of neurodegeneration in particular, are located inside the cells and could thereby not be accessed with these previously described approaches. The platform described in this Chapter provides a strategy that can facilitate simultaneous profiling of intracellular targets as well as surface markers at an essentially limitless multiplexing extent.

6.3 Results and Discussion

6.3.1 Preparation of oligonucleotide tagged affinity reagent tagged library

As described in Section 6.2, tagging the affinity reagent library with oligonucleotides provides an effective strategy to a reach high degree of multiplexing and analyse a virtually unlimited number of protein targets in parallel. To generate such oligonucleotide tagged antibodies, I used copper-free click reaction based on strain promoted alkyne-azide cycloaddition following the protocol by Click Chemistry Tools [230]. I would like to thank Marie Synakewicz (Department of Biochemistry, University of Cambridge) together with whom the first conjugation experiments were performed. In contrast to more commonly used copper catalysed alkyne-azidecyclo addition reaction, which has been reported to be detrimental to biomolecules, by causing their denaturation, for example [231], the strain induced version of this reaction allows the reaction to be performed in a copper-free environment.

Central to this conjugation reaction was DBCO-PEG5-NHS ester, a bifunctional molecule, which first reacts through its NHS-ester functional group with the lysine residues of the antibodies, following which the DBCO group on the antibody reacts with the azide group on the DNA (Figure 6.1a). Due to the reaction being non-specific, I would expect it to result in a

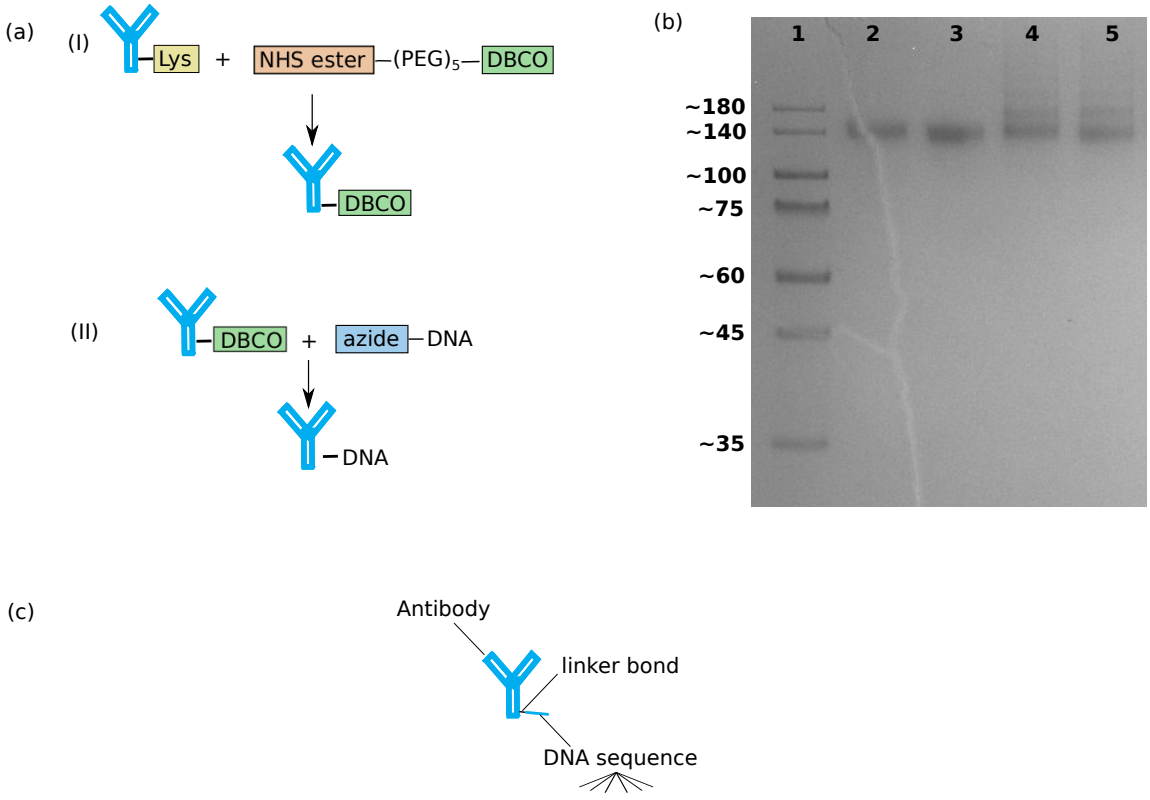

Fig. 6.1 Preparing antibody-DNA conjugates. **(a)** The antibody is conjugated to DNA by (I) activating it with DBCO using a bifunctional DBCO-PEG5-NHS ester molecule that reacts with the lysine residues of the antibody and (ii) reacting the DBCO-activated antibody with azide-modified DNA though copper free strain promoted alkyne-azide cycloaddition click reaction. **(b)** Polyacrylamide electrophoresis gel confirmed successful conjugation between the antibody and the DNA sequence. Each line included around 2 μg of protein. Lane 1 - protein ladder; lane 2 - unconjugated (control) antibody; lane 3 - DBCO activated antibody, lanes 4-5 - antibody-DNA conjugate. The reaction yields a mixture including antibodies with a different number of DNA oligonucleotide sequences. **(c)** The oligonucleotide sequence included a 7 nucleotide (nt) spacer sequence, 25 nt priming region, 12 nt protein identification barcode and 24 nt hybridisation region.

polydisperse product. A detailed protocol for the conjugation reaction is outlined in Materials and Methods (Section 2.4.1). After performing the conjugation, its extent was examined by analysing the reaction mixture on a polyacrylamide gel (Section 2.4.1). The reaction was found to result in only minimal amounts of the conjugated product formed when it was performed in the original storage buffer of the antibody (PBS, pH 7.36). This low reaction yield is likely to be a result of a small protonation extent and, thus, low chemical reactivity of the lysine groups at this pH. To increase their reactivity, I exchanged the buffer before performing the conjugation reaction. Indeed, the reaction in 100 mM PBS at pH 8.0 was found to result in successful conjugation with the product including a mixture of antibodies with a different number of oligonucleotide sequences attached to it (Figure 6.1b; the molecular weights of the antibody and the DNA were around 150 kDa and 22 kDa, respectively). The polyacrylamide data show that the reaction mixture still included a significant fraction of non-conjugated antibody. Although a further increase in the pH of the reaction environment could potentially result in even higher reaction yields due to the increased protonation rate of the lysine residues (pKa 9) at elevated pHs, such conditions may be unfavourable for the antibody and were, thus, not investigated.

The DNA sequence that was attached to the antibody is shown in Table 6.1. The sequences included regions serving different functional purposes (Figure 6.1c) - a spacer sequence (7 nt) in the 5' end, followed by a priming region (25 nt), protein identifier (12 nt) and a hybridisation region (24 nt) through which the DNA sequence becomes linked to the oligonucleotides carrying cell identifiers as part of the barcoding step (Section 6.3.2).

Here, we proceeded by directly using the conjugated antibody for the experiments described in the following sections. In the future, it may be beneficial to perform separate experiments confirming the functionality of the antibody before its further use. Such examination could be performed, for instance, through an SPR experiment or a conventional enzyme-linked immunosorbent assay (ELISA).

6.3.2 Cell encapsulation and barcoding

Figure 6.2 describes the general strategy for barcoding the proteomic material of the cells. Briefly, cells are co-encapsulated into individual droplets with the barcoded antibodies and barcoding beads. This co-encapsulation process is performed using a microfluidic device where two aqueous streams - one containing the cells and the other containing lysis buffer together with the barcoding beads and the antibodies - are mixed on chip and individual droplets pinched off by surfactant supplemented immiscible oil (Figure 6.2a). Each of the barcoding hydrogels usually contains a large number of DNA sequences each carrying (i) a

cell identification region (cell ID) that is identical between all the sequences within the same hydrogel but differ between the hydrogels and (ii) so-called unique molecular identifier (UMI) that is unique on every sequence, thereby allowing accounting for any potential bias introduced in the amplification step. These sequences are linked to the hydrogel bead through a (photo)cleavable linker and are cleaved off to initiate the barcoding process once the cells and the beads have been co-encapsulated (Figure 6.2b). Such barcoding beads could be bought or produced following the protocol described by Klein et al. [217]. For the proof-of-concept experiments performed in this Chapter, instead of the barcoded hydrogel beads, I used DNA sequences carrying placeholders for both the cell ID and the UMI (Table 6.1).

To illustrate the possibility of using such a strategy for detecting intracellular proteins inside cells, I set out to detect the presence of protein kinase B (PKB) in SH-SY5Y cells using Human AKT1 Matched Antibody Pair Kit (Materials and Methods, Section 2.4.1). The barcoding process was performed by injecting the two aqueous streams - the cells and the lysis buffer together with the barcoding beads and barcoded antibodies - into a microfluidic droplet maker device at a flow rate of 150 μL h^{-1} and the FC-40 oil supplemented with 2% surfactant at a flow rate of 800 μL h^{-1} (Figure 6.2a) as described in Materials and Methods (Section 6.3.2). The lysis buffer included the barcoding DNA sequences at a concentration of 50 nM and protein kinase B detector antibody at a concentration of 12.5 nM. These concentrations ensured that there is sufficient cell identifier sequences available for every antibody molecule. Moreover, with the size of the generated droplets being around d = 100μm, there are

$$\begin{aligned} \mathrm{N_{molecules}} &= \frac{1}{2} \cdot \mathrm{N_A} \cdot \mathrm{c} \cdot \mathrm{V} \\ &= \frac{1}{2} \cdot (6 \cdot 10^{23} \ \frac{\text{molecules}}{\text{mol}}) \cdot (12.5 \cdot 10^{-6} \ \frac{\text{mol}}{\text{m}^3}) \cdot [\frac{\pi}{6}(100 \cdot 10^{-6})^3 \ \text{m}^3] \\ &= 4 \cdot 10^6 \ \text{molecules} \end{aligned} \tag{6.1}$$

of antibody in each droplet, where the factor $\frac{1}{2}$ described the on-chip dilution. If proteins on very high abundance are to be detected (with mammalian cells containing around 100 million proteins in total, only a small number of proteins are present at concentrations higher than a few million [232, 233]), higher concentration of antibody can be used.

Once a stable droplet formation had been established, around 150 μL of the emulsification product was collected into a PCR tube with n = 3 tubes formed in total. Additionally, control droplets were formed using an identical process with the aqueous inlet for the cell suspension replaced with blank PBS with no cells (Figure 6.2). Inside the droplets, the cells lysed and the DNA-tagged antibodies bound to the PKB molecules released from the cells and the DNA sequences on these antibodies hybridised to the barcoding sequences (Figure 6.2b, Table 6.1). This ensured that the cellular identify of each protein molecule (cell ID), the digital counting

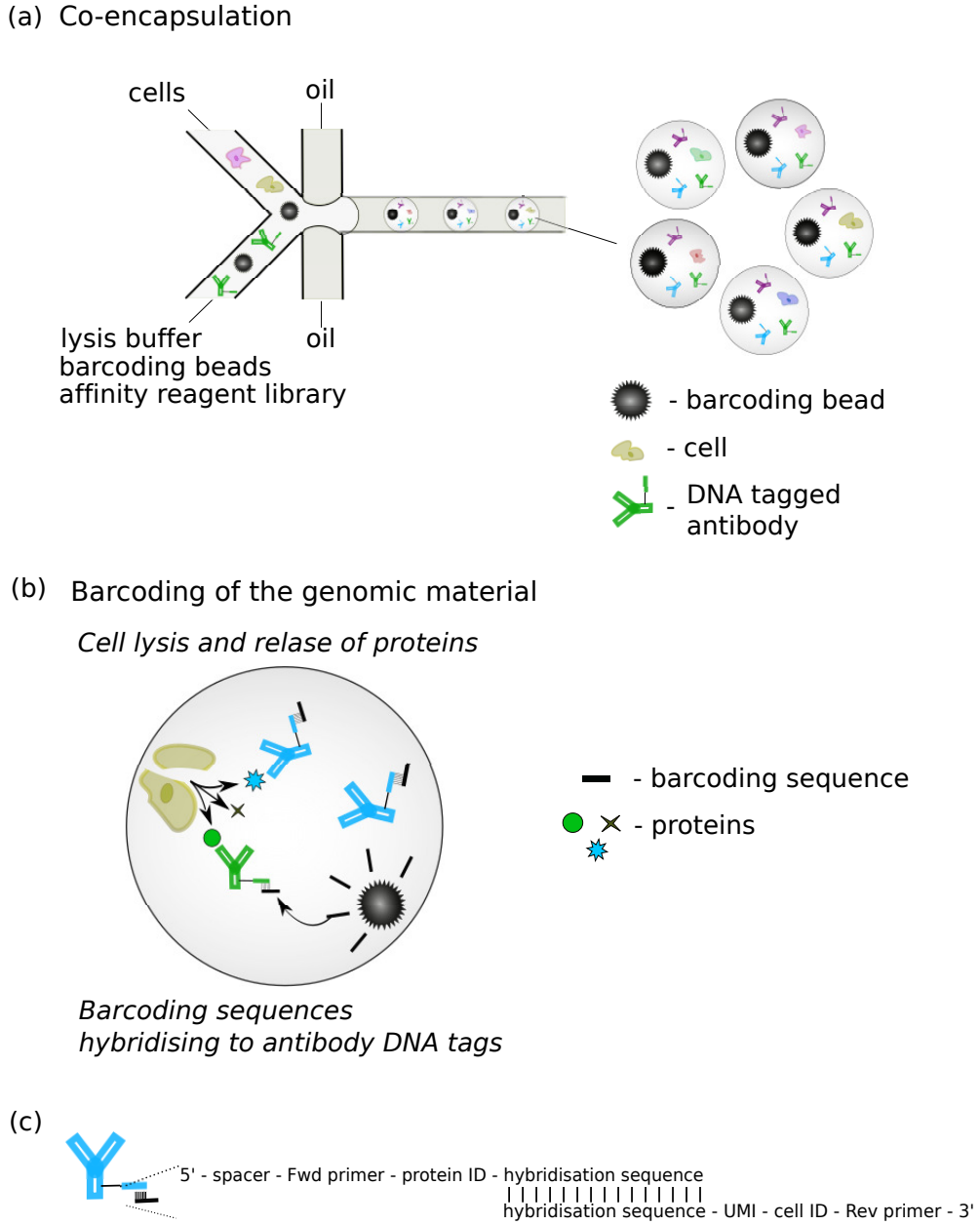

Fig. 6.2 Schema for barcoding the proteomic material of cells. **(a)** Cells are co-encapsulated with barcoding beads carrying barcoding sequences and with barcoded antibodies library into individual microdroplets. **(b)** Inside the compartmentalised environment the cells lyse and the proteins bind to their corresponding antibodies. Simultaneously, barcoding oligonucleotide sequences hybridise to their complementary regions on the 3' ends of the antibody conjugated DNA **(c)** to bring together the cell ID and the protein ID.

Table 6.1 Summary of the DNA sequences used for the barcoding process.

	Sequence
Antibody tag	Azide - Spacer [7 nt] - Priming region [25 nt] - Protein ID placeholder [12 nt] - Hybridisation region [24 nt] 5' Azide - TTT TTT TGT CTC GTG GGC TCG GAG ATG TGT ATA AGA GAC AGA CTT CAG CCT TAT CGT CGT CAT CCT TGT AAT C 3'
Cell barcode	spacer[7 nt] - Priming region [25 nt] - Cell ID placeholder [12 nt] - UMI placeholder [8 nt] - Hybridisation region [24 nt] 5' Acrydite - TTT TTT T AAG CAG TGG TAT CAA CGC AGA GTA CAC GTT GCA TAG CNN NNN NNN GAT TAC AAG GAT GAC GAC GAT AAG 3'
Fwd primer	5' GTC TCG TGG GCT CGG AGA TGT GTA TAA GAG 3'*
Rev primer	5' AAG CAG TGG TAT CAA CGC AGA GTA C 3' *

sequence (UMI) and the type of each protein (protein ID) were incorporated into a single entity (Figure 6.2c). The droplets were then de-emulsified using perfluorooctanol (PFO) as described in Materials and Methods (Section 6.3.2) to form a continuous aqueous phase, of which around 20 μL was carefully transferred into a clean PCR tube for further processing and analysis as described in the following sections (purification and sequencing).

6.3.3 Purification of protein bound DNA-antibodies and information amplification

I noted that aqueous product produced after the emulsion was broken (Section 6.3.2), included both, these DNA-conjugated capture antibody molecules that were bound a PKB molecule and these that were not. To purify the product for it to include only those antibodies that were bound to a PKB molecule, I used the detector antibody in the antibody pair and conjugated it to a streptavidin magnetic bead as described in Materials and Methods (Section 2.4.3). The magnetic bead conjugated detector antibody was mixed with the aqueous product and only protein bound capture antibodies with their corresponding DNA sequences pulled down (Figure 6.3a). The DNA sequences and antibodies were then released from the beads (Figure 6.3b) by boiling the product in 0.1% sodium dodecyl sulphate (SDS; Materials and Methods, Section 2.4.3) and 20 μL supernatant including only the DNA sequences of interest transferred into a fresh PCR tube (Figure 6.3c). I estimate that this 20 μL of aqueous

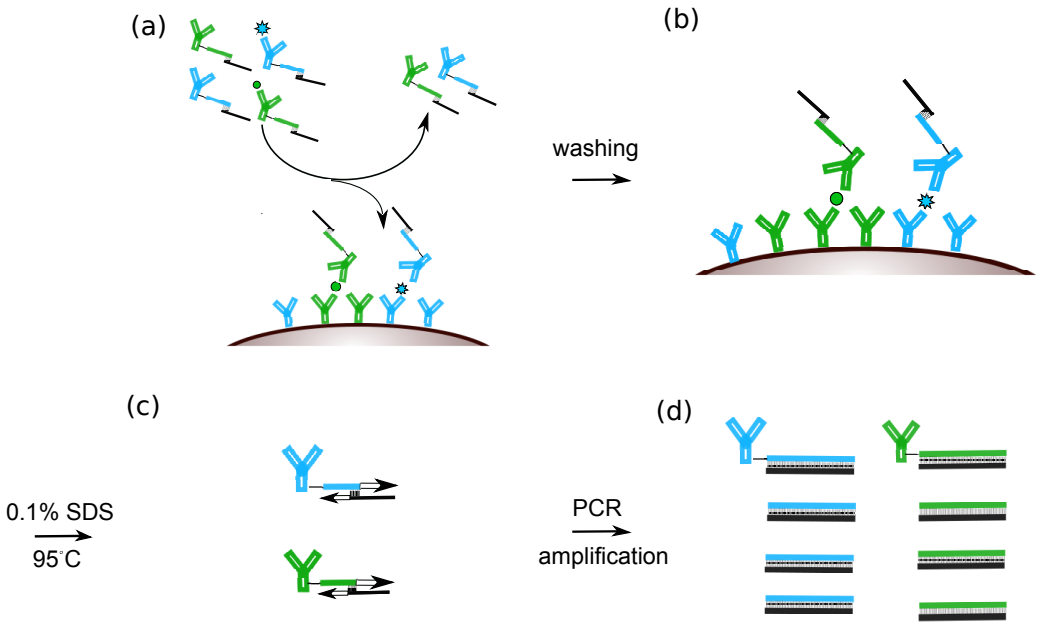

Fig. 6.3 Purifying the DNA-antibody product and preparing the DNA library. **(a)** After breaking the magnetic bead conjugated detector antibodies are used to the capture antibodies that are bound to the protein molecules. **(a)** The unbound affinity reagents are washed off, **(c)**the oligonucleotide sequences released from the beads and the 3' ends of the sequences extended to encode the cellular and the molecular identity of each protein molecule into one oligonucleotide sequence. **(d)** Finally, the product is amplified through polymerase chain reaction (PCR).

phase included around

$$N_{\text{cells}} = \frac{V_{\text{total}}}{V_{\text{droplet}}} = \frac{20\ \mu\text{L}}{\frac{\pi}{6}\ \cdot\ (75\ \mu\text{m})^3} = \frac{20\ 000\ \text{nL}}{0.5\ \text{nL}} = 38\ 000\ \text{cells} \tag{6.2}$$

To examine the presence of PKB, I amplified the product through polymerase chain reaction as described in Materials and Methods (Section 2.4.4). Specifically, 6 μL of the DNA library was collected and divided equally between three PCR tubes each involving 2 μL of the DNA product diluted into a 20 μL PCR mix. This corresponded to around $\frac{2\ \mu\text{L}}{20\ \mu\text{L}} \cdot 38000$ cells $= 3,200$ cells in each PCR assay.

The samples were amplified on a qPCR for 35 cycles as described in Materials and Methods (Section 2.4.4). Three independent replicates of the same experiment (cyan, red and blue lines; the experiments involved cells that were cultured together but were run on separate microfluidic devices (Figure 6.2) and through a separate purification process (Figure 6.3)) were performed and the amplification data indicated the presence of PKB molecules in all

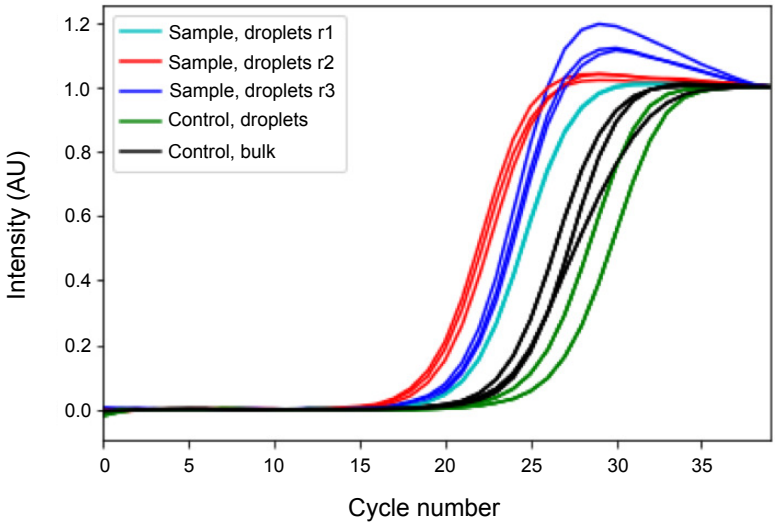

Fig. 6.4 Detecting the presence of protein kinase B in individual SH-SY5Y neuroblastoma cells. The presence of the protein in the cells was confirmed by amplifying the DNA library by polymerase chain reaction and comparing the amplification process to a sample with no cells. Each of the amplification curves (cyan, red, blue) involved to around 3200 cells with the different colours corresponding to different experiments and identical colours corresponding to parallel PCR assays of the same experiment. The distribution of the protein in each of the cells could be obtained by sequencing the DNA oligonucleotide pool.

the three samples (Figure 6.4). Double-stranded amplification products were also detected in the control sample both when the experiments were performed in droplets (green) and when they were performed in bulk (black). These products are likely to be a result of non-specific amplification during the PCR reaction, non-ideal purification of the product with the magnetic beads due to binding of the DNA sequences through non-specific interactions or non-specific binding of the antibody as will be discussed in more detail in Section 6.4. Crucially, the double-stranded product appeared at a smaller cycle number in all the cell samples and from the fluorescent intensity was estimated to be around five times as abundant as the non-specific product. Nevertheless, further optimisation of the protocol is required to reduce the non-specific binding events and yield a library that would be even more dominated by the product of interest.

6.4 Conclusion and next steps

I have described and implemented an approach for detecting intracellular proteins inside individual cells using a microfluidic DNA-based barcoding strategy. In addition to analysing a large number of cells in parallel, this DNA-based barcoding strategy allows the analysis to be performed on a virtually unlimited number of targets simultaneously, overcoming one of the key disadvantages of current state-of-the-art single cell protein profiling approaches, such as cytometry approaches that rely on fluorescence or mass spectrometry based readouts.

I demonstrated on the example of protein kinase B molecules in SHSY-5Y neuroblastoma cells that the developed platform allowed successfully detecting the presence of intracellular proteins in single cells. However, I observed that the strategy resulted in a higher than desired amount of amplification products in the control samples that did not include any protein molecules. This could be caused by at least two distinct factors. First, it is possible that the magnetic bead based purification step (Figure 6.3) designed to remove unbound capture antibody molecules did not result in their complete removal, thus, giving raise to a false positive signal. This incomplete removal could have occurred, for instance, due to non-specific binding of the DNA sequences to purification beads through electrostatic interactions. A potential strategy for overcoming such non-specific binding could involve supplementing the purification medium with a high concentration of an orthogonal DNA sequence (e.g. poly-T), which would not get amplified in the proceeding PCR reaction but would decrease the amount of non-specific binding of the sequences that are amplified by the PCR. Secondly, non-specific primer annealing events could have occurred within the PCR reaction. Indeed, it is not uncommon to observe non-specific amplification products after 25 PCR cycles. Their occurrence could be reduced by further optimising the PCR protocol, most notably the annealing temperature and the design of the primer sequence. It is a subject to further experiments to validate the sources of these non-specific amplification products and to devise strategies for suppressing their occurrence, as such an insight would enable preparing a better optimised library for sequencing.

I noted that whereas the protocol here could be effectively used for detecting the presence of protein molecules, in its current form, it does not allow cell specific quantification. Indeed, during the step that involved a release of the DNA sequences from the magnetic beads (Figure 6.3b-d), the reaction mixture was heated to 95°C, which resulted in deannealing of the two DNA sequences carrying the cell and the protein identifier sequences. In order to overcome this limitation and allow preserving cell specific information, in the future, the DNA extension reaction would have to be performed directly on the bead before the biotin-streptavidin bond is cleaved.

In conclusion, I have demonstrated an approach for detecting intracellular proteins inside cells on the example of protein kinase B molecules inside SHSY-5Y neuroblastoma cells. This approach sets the basis for a platform that enables a high throughput characterisation of a large number of intracellular protein targets inside cells, far exceeding the multiplexing extent of any previously described approach. Further optimisation of the protocol as outlined in the previous paragraph is suggested to increase the sensitivity limit of the technique.

Chapter 7

High power density biological photovoltaic devices (BPVs)

This Chapter is based on the following publication:
*Saar KL et al., Nature Energy, 3**(1)**, 75-81, 2018.*

7.1 Motivation

Effective manipulation of cells has shown to set the basis for a diverse set of interesting applications ranging from medicine and material science to energy generation [234–237]. In the realm of energy generation, biological photovoltaics (BPVs; also known as biophotovoltaics and biological solar cells) are emerging as an environmentally friendly and a low-cost approach for harvesting solar energy and converting it into electrical current [238, 239]. Indeed, energy demand driven by a rising global population must increasingly be satisfied from renewable alternatives to fossil fuels, as the latter release extensive amounts of greenhouse gases with potentially devastating consequences on our ecosystem. Solar power is considered to be a particularly attractive source as on average the Earth receives around 10,000 times more energy from the sun in a given time than is required by human consumption [240, 241]. Although a number of technologies exist to convert this extensively available sunlight into electrical current [242, 243], factors such as scarcity of production materials, high cost per delivered quantity of electricity, and lack of equally efficient storage technologies have limited their adoption [243–247].

In the heart of the emerging technology of biological solar cells rely photosynthetic cells that convert light into high-energy electron-hole pairs. The resultant excited electrons are transferred through a number of intracellular electron carriers with a fraction eventually exported across the cell membrane [248, 249] (Figure 7.1). These secreted electrons are

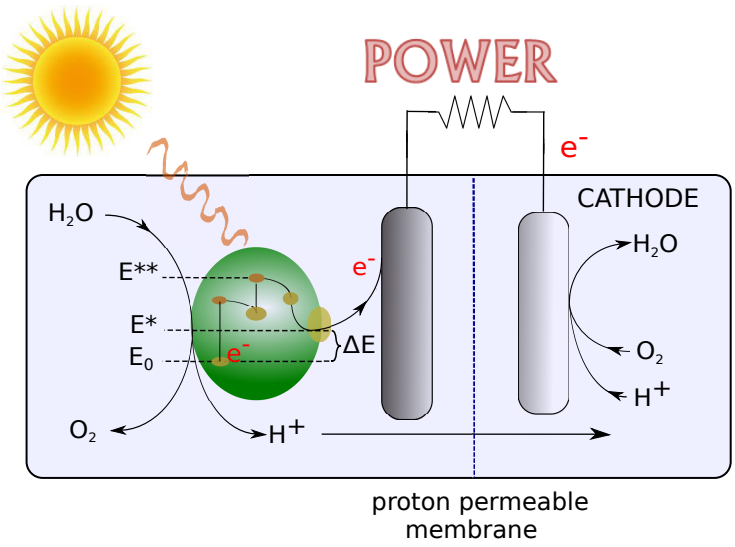

Fig. 7.1 In a BPV, high energy electrons (e^-) are generated by the photosynthetic cells in response to sunlight and some of these electrons are secreted to the external environment through the exoelectrogenic activity of the cells. These electrons can be brought into contact with the anode from where they flow to a lower potential electrode, the cathode. Protons (H^+) move to the cathodic chamber through a proton permeable membrane where water is catalytically re-generated while the electrons reach the cathode only via the external circuit.

directed to an electrode from where they are allowed to flow to a more positive potential electrode, thus generating current. A proton permeable membrane separates the anodic chamber from the cathodic one, ensuring that electrons travel between the two electrodes only via the external load. Simultaneously, the protons released by the cells diffuse from the anodic area to the cathodic one where water is re-formed. This process leads to the generation of current without release of any chemical side products.

BPVs demonstrated to date rely either on suspending photosynthetic cells in solution or immobilising them directly onto an anode [250]. In these designs, electron generation and transfer to the electrical circuit occur in a single compartment, and the electrons reach the anode and generate current as soon as they have been secreted (Figure 7.1). In this Chapter, I propose, build and demonstrate two-chamber BPV devices, where the two key processes involved in the operation of a BPV - generation of high energy electrons and their conversion to current - are spatially decoupled from one another. With these devices, I improved on the power densities of previously demonstrated biophotovoltaic systems around two and a half fold using wild-type photosynthetic organisms and by fivefold using specifically generated mutants [251].

7.2 A two-chamber flow-BPV

I describe and demonstrate a two-chamber system where the two key process occurring in a BPV - charging (reduction of the electron carrier molecules by exoelectrogenic electrons) and power generation (electron transfer to the external electrical circuit) - are spatially decoupled from one another (Figure 7.2). Such decoupling allows the geometrical configurations and operating conditions for the two processes to be chosen independently, which in turn opens up the possibility to optimise their performance simultaneously.

In particular, for the BPV system described and demonstrated here, I exploited miniaturised geometries in the power generation unit. Operation at small length scales suppresses convective mixing [252], enabling the omission of the semipermeable membrane normally required to separate the unit into anodic and cathodic compartments. In addition to decreasing the internal resistance of the device, omitting the membrane reduces the cost of the system and makes the operation easier as membranes have been reported to dry out, degrade, foul and clog [253, 152, 254]. More generally, the use of small length scales has the potential to decrease the resistive electrical losses of the system due to elevated surface-to-volume ratios, enhanced mass transfer coefficients and small electrode separation [152, 254–256]. Such small channels, however, are likely not to be the optimal geometrical configuration for the charging unit, where instead a balance between the surface area and the depth of the vessel needs to be found to facilitate the generation of the largest amount of charge carriers per illuminated area.

7.3 Results

7.3.1 Flow-BPV design

The power delivery unit of the BPV was fabricated in PDMS via soft photolithography (Materials and Methods, Section 2.1.2) as a rectangular channel of a width of w = 250 μm, length of L = 6000 μm and height of h = 25 μm with one inlet for the anodic and one for the cathodic fluid (Figure 7.3). The anolyte and catholyte were injected into device through their respective inlets with the former including photosynthetic cells suspended in their growth medium (BG-11) together with electron carrier (EC) ions that facilitate the transfer of the electrons released by the photosynthetic cells to the electrical circuit, and the latter comprising of only the growth medium. Due to the similar viscosities of the two solutions, the boundary between the two areas at the start of the chamber was determined by the relative flow rates of the two fluids [257, 258].

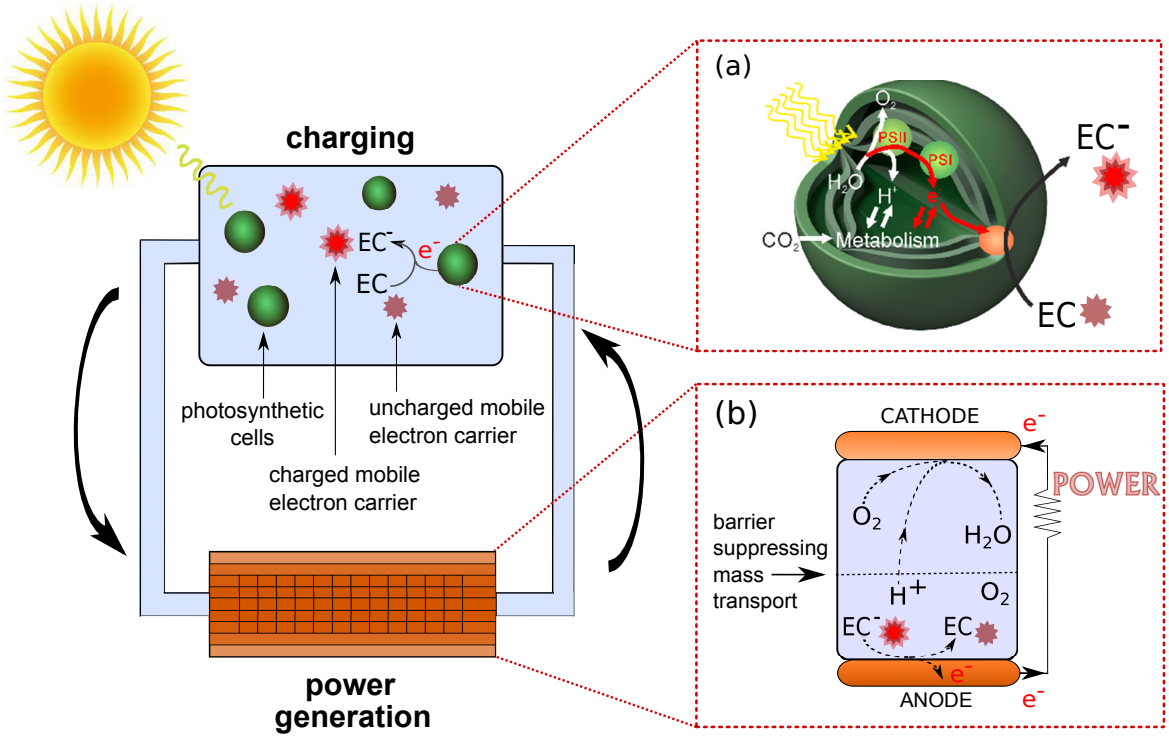

Fig. 7.2 In a flow-BPV, the charging process can be spatially decoupled from power generation providing temporal flexibility over power generation and enabling independent optimisation of the two processes. Inset **(a)**: In the charging unit high energy electrons (e^-) are generated by the photosynthetic cells, some of which are released to the external environment via the exoelectrogenic activity of the cells to reduce the charge carriers ($EC \rightarrow EC^-$). Inset **(b)**: In the power generation unit the reduced charge carriers (EC^-) are brought into contact an anode. In our devices, proton permeable membranes were generated by controlled mass transport at small length scales as described in detail in Section 7.3.1.

Specifically, the fluids were injected into the device at flow rates of $Q_{catholyte} = 16\ \mu L\ h^{-1}$ and $Q_{anolyte} = 4\ \mu L\ h^{-1}$, setting the interface a distance of 20% of the total width of the device away from the anode (Figure 7.3, inset a). Such placement ensured that due to the limited residence time of the fluids in the device, a significantly larger fraction of the electron carrier ions would reach the anode than the cathode by molecular diffusion. Moreover, the dimensions of the system were chosen such that protons, which have over an order of magnitude higher diffusion coefficient than the electron carrier ions, could diffuse to the cathode within the limited residence time of the fluids in the device while the electron carrier molecules would remain in the vicinity of the anode. Indeed, under our chosen operating conditions the protons diffuse on average by

$$x_{diff,H^+} = \sqrt{2D_{H^+}t_{res}} = \sqrt{2 \cdot 9.8 \cdot 10^{-9}\ m^2\ s^{-1} \cdot \frac{(16+4)\frac{mm^3}{h}\frac{1\ h}{3600\ s}}{0.025 \cdot 0.25 \cdot 6.5 \cdot mm^3}} = 270\ \mu m \quad (7.1)$$

whereas the electron carrier (ferrocyanide was used for this purpose throughout the experiments - Section 7.3.2) ions move by

$$x_{diff,EC} = \sqrt{2D_{EC}}t_{res} = \sqrt{2 \cdot 7.5 \cdot 10^{-10}\ m^2\ s^{-1} \cdot \frac{(16+4)\frac{mm^3}{h}\frac{1\ h}{3600\ s}}{0.025 \cdot 0.25 \cdot 6.5 \cdot mm^3}} = 74\ \mu m, \quad (7.2)$$

indicating that the majority of the protons reach the cathode whereas the majority of the electron carrier ions do not.

To confirm that the flow profile under these conditions is indeed laminar, I estimated the Reynolds number, Re, to be

$$Re = \frac{\rho\ u\ d_H}{\mu} = 0.04 < 2000 \quad (7.3)$$

where the fluid velocity, u, was estimated from

$$u = \frac{Q}{A} = \frac{20\ \frac{mm^3}{h} \times \frac{1h}{3600\ s}}{0.025\ mm \times 0.25\ mm} = 0.9\ mm\ s^{-1} \quad (7.4)$$

and the hydraulic diameter, d_H, from

$$d_H = \frac{4A}{P} = \frac{4 \times 0.025\ mm \times 0.250\ mm}{2 \times (0.025\ mm + 0.250\ mm)} = 45\ \mu m \quad (7.5)$$

Hence, under these operation conditions, an effective diffusion-controlled proton permeable barrier between the cathodic and anodic areas is generated (Figure 7.4, insets b-c), permitting the power harvesting unit to be fabricated without the inclusion of a membrane.

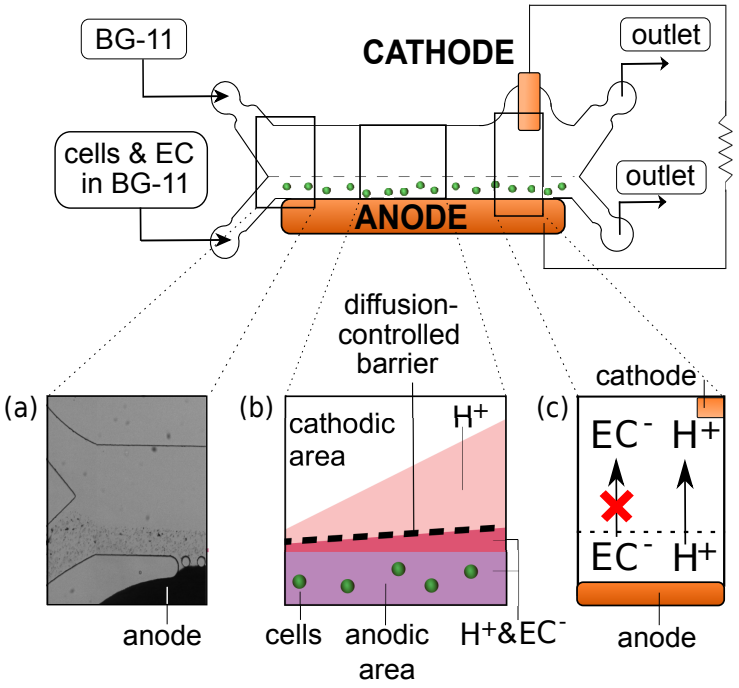

Fig. 7.3 Schematic diagram (not to scale) of the power generation unit of the flow-BPV. Cells and electron carrier (EC) in growth medium BG-11 were inserted into the anodic area and the growth medium BG-11 into the cathodic one. Insets: **(a)** The flow rate of the anodic fluid was set to be 20% of the total flow rate, so that the electron carrier ions would remain in the vicinity of the anode. **(b)** The absence of inertial forces at small length scales allowed generating a diffusion-controlled barrier **(c)** that can be crossed only by fast diffusing species, in this case protons but not the electron carrier or the cells.

7.3.2 Flow-BPV performance

Throughout the experiments performed in this Chapter, *Synechocystis* sp. PCC6803 cells were used as the biological catalyst, motivated by their previously demonstrated exoelectrogenic activity [259, 260] and the availability of genetic tools for the generation of multiple mutations in the genes encoding for electron transfer components [123]. $K_3[Fe(CN)_6]$ was used as an electron carrier and it was pre-mixed with the cells at a concentration of 30 mM at which $K_3[Fe(CN)_6]$ had previously been shown to be physiologically well tolerated by *Synechocystis* sp. PCC6803 cells over extended time periods [260].

The performance of the power generation unit of the BPV was characterised while injecting a mixture of the electron carrier and cyanobacterial cells in their growth medium (BG-11) from the anodic inlet and the growth medium from the cathodic inlet (Figure 7.3). Before injection, 1 mL of the anodic solution was illuminated for 3 hours under red light at a constant output of 30 μmol photons m^{-2} s^{-1} as described in Materials and Methods (Section 2.5.3) to reduce the $K_3[Fe(CN)_6]$ by the exoelectrogenic electrons released by the photosynthesising cells. During this process the solution was spread over a circular area of a diameter of 1.0 cm.

The current-voltage (polarisation) curves for the devices were acquired by varying the applied voltage and recording the respective current at each voltage using a potentiometer as described in Materials and Methods (Section 2.5.3). The resulting polarisation curves for three independently fabricated devices are shown in Figure 7.4a. Unlike approaches that change the resistor connected to the system and hence vary the voltage and the current simultaneously, potentiometric measurements alter only one parameter at a time and have become a commonly used method for BPV characterisation [261, 262].

From these measured polarisation curves, I deduced the internal resistance of the BPV to be approximately 3 MΩ and its resistivity to be around 500 Ω m. Due to the varying area between the anode (spanning the full length of the device) and the cathode (a point electrode) the latter value is an approximation and was for the purpose of this estimate obtained by using the average of the two areas. This resistivity value is substantially smaller than for our previously built devices of larger scale - 19 kΩ m [260] and 69 kΩ m [239], both of which had similarly used BG-11 as the carrier medium. This decrease is most likely to originate from the reduced resistive losses at the smaller length scales and from the absence of a semipermeable membrane in the design [152, 254–256]. Additionally, I did not observe a tendency for the polarisation curves to show higher gradients, even at high currents. This finding indicates that the performance of the device was not limited by diffusion or mass transfer [255, 261].

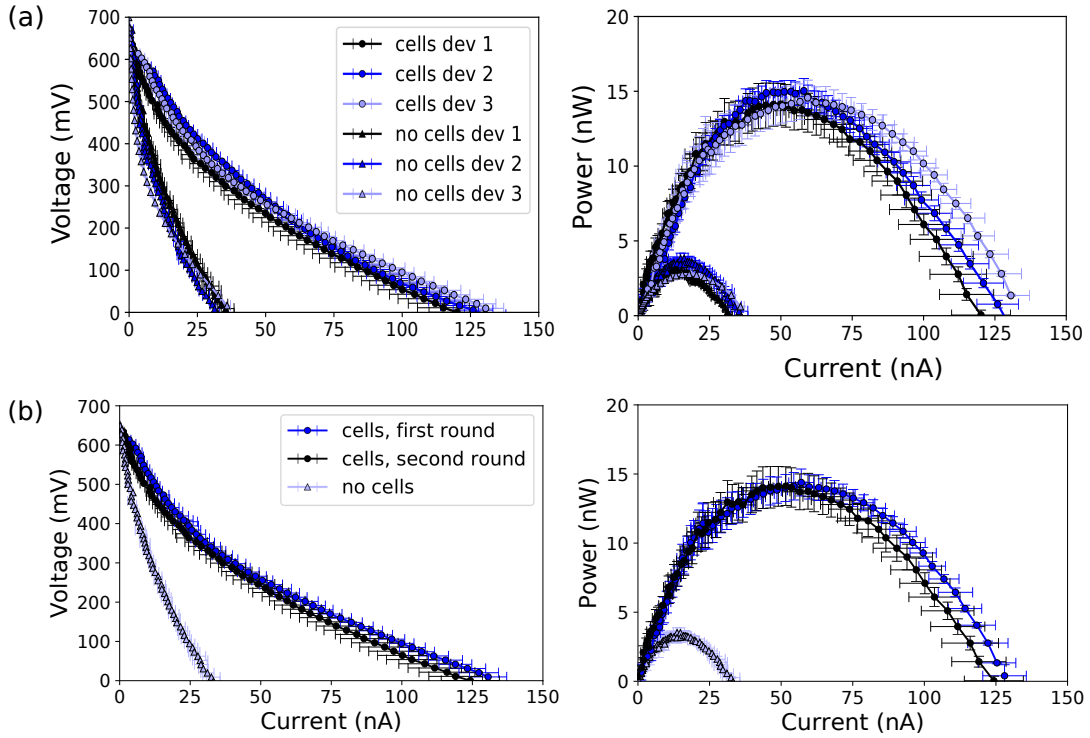

Fig. 7.4 **(a)** The polarisation (left) and power (right) curves for the fabricated μ-BPV devices (average of n = 3 repeats in three independently fabricated devices dev 1-3; error bars correspond to standard deviations) with cells (circles; chlorophyll concentration of $c_{chl} = 8$ μM) and without cells (triangles). **(b)** The polarisation (left) and power (right) curves on the first (blue circles) and second injection (black circles) and without cells (light blue triangles) to verify that the cells can be recycled and the device reused.

Small background currents were recorded when the device was operated with the anolyte including only the growth medium and the electron carrier with no cyanobacterial cells (Figure 7.4a, triangles). Such background currents have been reported previously and attributed to the ionic concentration of the medium and slow formation of electrolysis products at the anode [263, 264]. This background current was similar between all the devices used (Figure 7.4a, triangles).

The power curves for all the devices were constructed using the relationship

$$P = U \cdot I \tag{7.6}$$

and as in previous studies, the peak biotic power of each device was quoted as the difference between the peak power of the device operated with cyanobacterial cells and the device operated without the cells at the same current [250, 264]. From our data, the average peak biotic power output for the μ-BPVs was estimated to be 13.9±0.9 nW (Figure 7.4a; average of n = 3 repeats in the three independently fabricated devices) occurring at a current of 60 nA.

To analyse the possibility of operating the system in a recirculating mode (Figure 7.2), I further collected the anolyte and catholyte solutions at the device outlets to test whether the solutions and the device can be reused. After illuminating the anodic fluid for an additional 3 hours to recharge the electron carrier molecules, I re-injected the solutions to the device. Crucially, the device performance was unaffected between the two rounds of recirculation (Figure 7.4b), indicating the pressure drops inherent in the device operation did not damage the device or the cells or affect their exoelectrogenic ability.

7.3.3 Optimal flow rate for the BPV performance

I expect the performance of the flow μ-BPV to depend critically on the flow rates of the fluids into the anodic and the cathodic half-cells. On the one hand, at higher flow rates, not all the charged electron carriers can diffuse to the anode within their residence time in the device. On the other hand, at low flow rates, the reduced electron carrier ions can cross the channel and lead to short-circuiting in the device. Indeed, such behaviour has been reported for microbial fuel cells as the fuel cross-over concept [265, 266] where the termination of flow has been observed to cease power outputs entirely [267].

The effect of the flow rate of the BPV performance was investigated by keeping the ratio of the catholyte and anolyte flow rates fixed ($\frac{Q_{cathodic}}{Q_{anodic}} = 4$) and recording the power curves at a range of total flow rates. The peak biotic power outputs were then normalised by the number

of charge carriers that entered the device in a given time. This normalised power output was observed to decrease with the flow rate (Figure 7.5a, blue circles; average of n = 3 repeats). This decrease can be accounted to less efficient conversion of the charged electron carrier ions to current due to not all the charged carriers coming into contact with the anode at these high flow rates. The disappearance of this trend at small flow rates, O(10 μL h^{-1}) is likely due to the effect of a more significant cross-over of the charged carrier, complete reduction of the electron carrier or both.

I further simulated [194] the movement of the electron carrier ions in the channel to estimate the fraction of ions that can diffuse to the two electrodes as a function of flow rate. The experimental data for the normalised power was observed to follow a similar trend to the simulations but the experimentally recorded power output was observed to decline faster than the fraction of electron carriers that reach the anode according to the simulations (Figure 7.5a; black line). Potentially other factors not accounted for in this simple model start to limit the performance of the device, such as the availability of protons on the cathode or mass transfer limitations at the surface of the anode.

One disadvantage of a flow-based system in comparison to those that rely on biofilm growth on the anode is the viscous losses experienced by the fluids. For recirculation the fluids have to be pumped back to higher pressures before they re-enter the device (Figure 7.2). The energy dissipation in this process can be estimated to be:

$$\begin{aligned} P_{friction} &= [\Delta P \times A] \times u \\ &= R_h \times Q_{total} \times (w \times h) \times \frac{Q_{total}}{w \times h} \\ &= R_h \times {Q_{total}}^2 \end{aligned} \tag{7.7}$$

where ΔP is the pressure drop across the channel, A, w and h are its cross-sectional area, width and height, respectively, and u and Q the velocity and the flow rate of the fluid. The hydrodynamic resistance of the channel, R_h, was estimated as described by Mortensen et al. [183].

Specifically, at a flow rate $Q_{total} = 20$ μL h^{-1} the pressure drop can be estimated to be $\Delta P = 110$ Pa and the associated frictional loss, $P_{friction} \approx$ 0.5 nW, which is a small fraction of the power generated by the device at this flow rate (14 nW; Figure 7.4a). The resulting temperature increase from this dissipated power is negligible.

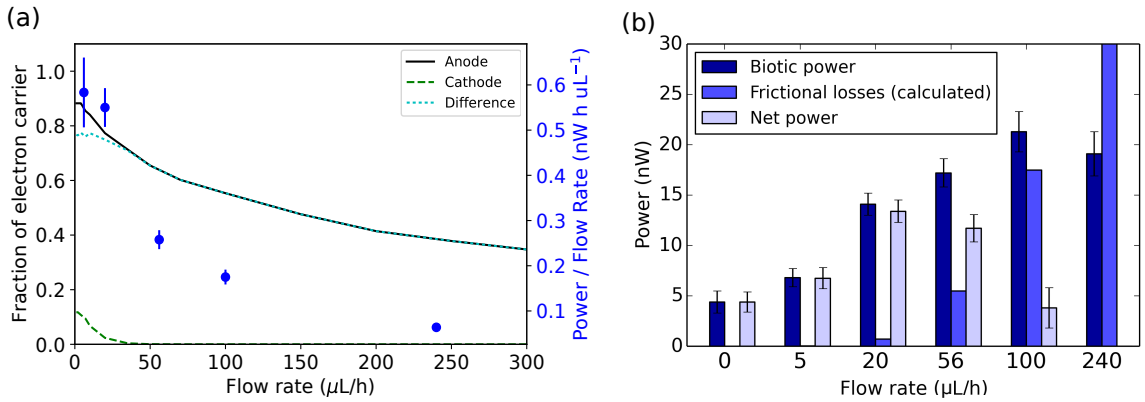

Fig. 7.5 **(a)** The biotic power outputs normalised by flow rate (blue circles, average of $n = 3$ repeats; $\frac{Q_{cathodic}}{Q_{anodic}} = 4$ for all) decreased with flow rate. One of the factors contributing towards this decrease is the reduced amount of electron carrier ions reaching the anode (solid line). **(b)** The generated biotic power, power loss due to friction and the net power output at different flow rates. $Q_{total} = 20\ \mu L\ h^{-1}$ was chosen for further experiments due to the net power output being at its highest at this flow rate.

Similar estimates for the dissipated energy were obtained when the pressure drop, ΔP, was instead approximated using the Darcy-Weisbach equation:

$$\Delta P = L \cdot \frac{f_D}{d_H} \cdot \frac{\rho \cdot u^2}{2} \tag{7.8}$$

where L is the length of the channel and ρ the density of the fluid in it. The hydraulic diameter, d_h, was estimated from equation 7.5 and the friction factor, f_D, in a laminar flow regime from:

$$f_D = \frac{64}{Re} \tag{7.9}$$

I further note that the actual required power input could be up to 50% higher due to non-ideal operation of pumps (typical efficiencies range from 65% to 90%). This is nevertheless a small fraction of the total generated power for all the experiments performed in this section and the following ones.

Overall, I conclude that higher flow rates do not only lead to a more inefficient use of the fuel (Figure 7.5a) but also to increased frictional losses (equation 7.7). In our demonstrated devices, at low flow rates the power output more than compensated for the energy losses from the viscous drag (Figure 7.5b). However, by comparing the performance of the device at various flow rates, I concluded that the increase in the biotic power output at higher flow

rates is eventually counterbalanced by the elevated power consumption needed to overcome the frictional losses. The optimal flow rate maximising the overall power output was found to be around 20 μL h^{-1} and was as such used in all the following experiments.

7.3.4 Multiparameter optimisation of the BPV power output

Unlike devices, where photosynthetic cells transfer their electrons directly to the anode, I used a design strategy where the charging and the power generation processes are spatially decoupled. Combined with the use of mobile electron carriers that are free to move and collect electrons from all the cells, this strategy has the potential to lead to elevated current outputs when increasing the concentration of cells under otherwise identical conditions, for as long as there is sufficient free electron carrier available in the system. I set out to test this hypothesis by characterising the performance of the device at two different concentrations of cells. I found that the peak power output increased with the cell concentration reaching (22.2 $\pm$ 1.5) nW (average of n = 3 repeats) at chlorophyll concentration of 40 μM (Figure 7.6a). I observed that the device yielded even larger power outputs at higher cell concentrations and in particular, recorded the peak power output to be 65 nW at $c_{chl} =$ 80 μM. However, adhesion of cells to the microfluidic channels was observed at the latter concentration which could start to limit the performance of the device. As such, I restricted all the data presented in this work to $c_{chl} =$ 40 μM where no difficulties with the operation were noted over a several hour operation period. Different strategies can be implemented for circumventing the problem of cell adhesion, such as treatment of the device surfaces. The increasing power output with the cell concentration suggests that flow-based operation can provide a simple approach to increase the power output of the devices, resulting in an advantage over systems where the generated power is limited to the monolayer of the cells on the electrode.

Exoelectrogenic activity in wild-type photosynthetic organisms is not optimal for production of photocurrent, since some of the electrons generated are subsequently consumed by a series of electron sinks [250]. This is likely to reduce the power production. To overcome this limitation, I generated a *Synechocystis* mutant deficient in the main photosynthetic and respiratory electron sinks, the terminal oxidases (cytochrome *c* oxidase, quinol oxidase and the alternative respiratory terminal oxidase), and the flavodiiron complexes, Flv1/3 and Flv2/4 (Appendix A)[268, 269]. I predicted that the absence of these electron sinks would lead to elevated exoelectrogenic activity and hence also to increased BPV power outputs. Indeed, the characterisation of the BPV devices with mutant cells as the exoelectrogenic catalyst yielded around twice as high power output than when the wild-type cells at the same chlorophyll concentration were used ($c_{chl} =$ 40 μM), reaching a peak biotic power output of

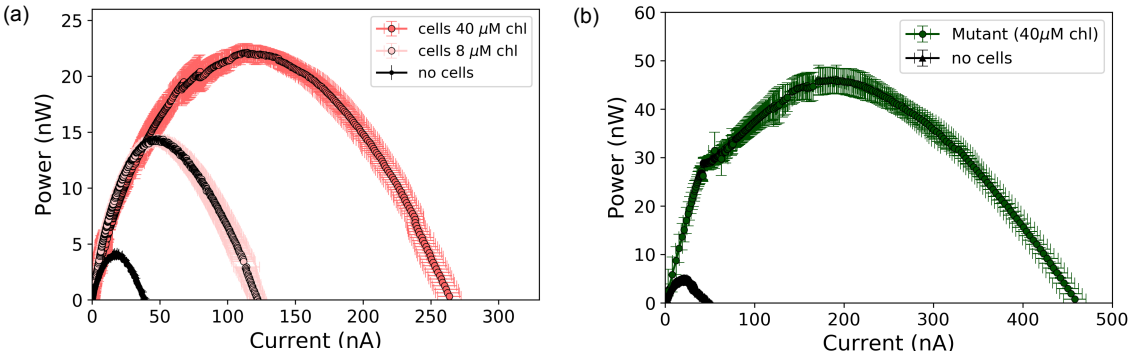

Fig. 7.6 Enhanced performance of the μ-BPV. **(a)** An increase in the cell concentration yields higher current and power outputs. **(b)** Using a mutant cells deficient in the main photosynthetic and respiratory electron sinks, the anodic power density of the BPVs doubled compared to using wild-type cells at the same cell concentration (c_{chl} = 40 μM).

(44.6 ± 1.6) nW (Figure 7.6a,b).

Continuous operation

We have shown that while flowing through the device, the cells and their exoelectrogenic performance remains unaffected (Figure 7.4b). However, during every cycle some fraction of the electron carrier molecules diffuses from the anodic area to the cathodic one, eventually leading to a decrease in its overall concentration in the anolyte. To show that this diffusion process does not affect the possibility to operate the devices continuously, I studied the device performance by also including the electron carrier molecules $[Fe(CN)_6]^{3-}$ in the catholyte such that there would be no net movement of the $[Fe(CN)_6]^{3-}$ ions from one side to another. Crucially, this addition did not affect the device performance (Figure 7.7a). With the reduced electron carrier molecule $[Fe(CN)_6]^{4-}$ eventually oxidising back to $[Fe(CN)_6]^{3-}$ (Figure 7.7b), the system never runs short of the oxidised electron carrier $[Fe(CN)_6]^{3-}$, setting the basis for continuous operation.

I further note that whereas the $[Fe(CN)_6]^{4-}$ produced by the electrons released by the photosynthetic cells oxidises slowly back to $[Fe(CN)_6]^{3-}$, the rate of this oxidation reaction - measured to be around 5 nM s^{-1} (Figure 7.7b,c) - is significantly lower than that of the $[Fe(CN)_6]^{-4}$ generation by the electrons released by the cells (280 nM s^{-1} - value determined in Section 7.3.5). Although the elimination of oxygen could potentially prevent any back-oxidation, the challenges associated with its removal are unlikely to outweigh the potential

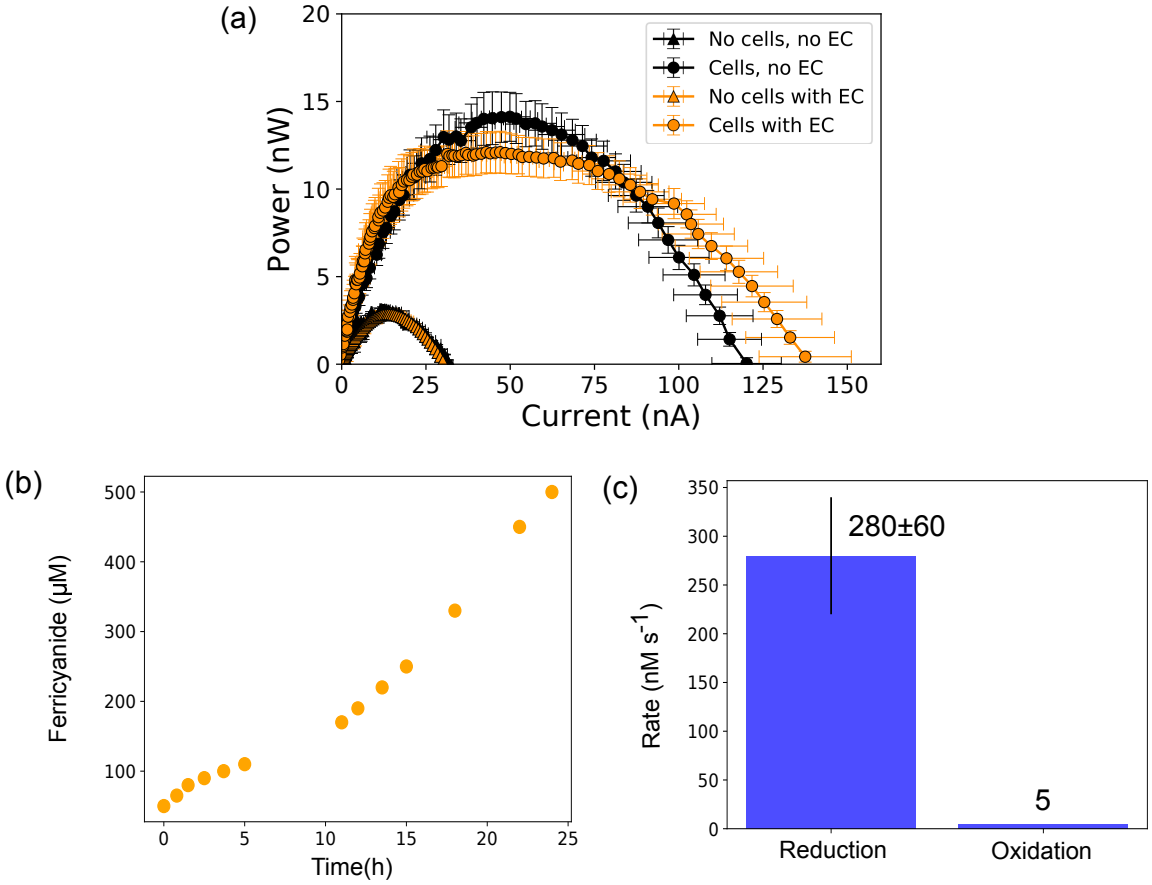

Fig. 7.7 Factors facilitating recirculating operation of the device. **(a)** The performance of the device was similar when ferricyanide ions ($[Fe(CN)_6]^{3-}$) were included (orange data points) and not included (black data points) in the cathodic fluid (both data obtained with wild type cells at $c_{chl} = 8\ \mu M$). **(b)** Ferrocyanide ($[Fe(CN)_6]^{4-}$) oxidation to ferricyanide ($[Fe(CN)_6]^{3-}$) in air over time. **(c)** The rate of this oxidation reaction can be seen to be significantly slower than the rate of ferricyanide ($[Fe(CN)_6]^{3-}$) reduction to ferrocyanide ($[Fe(CN)_6]^{4-}$) by the exoelectrogenic electrons released by the wild type photosynthetic cells.

gain, especially as oxygen removal could also affect the viability of the cells.

7.3.5 System scalability

I note that as opposed to previously described BPVs and conventional PVs, where the charging and power generation process occur in a single compartment, for the spatially decoupled design and operation described in this work, there is an additional area involved in the charging process which can in general be different from the area used for the power generation step. To allow for an effective comparison of our fabricated flow-BPVs with existing systems, I set out to compare the areas involved in the illumination and the power harvesting processes.

For this purpose, I illuminated V = 3 mL of wild type cell suspension under a fixed area of $A_{illumination} = 1$ cm^2 and under typical light conditions of 2000 μE m^{-2} s^{-1} [270]. I recorded spectroscopically that under these conditions, ferrocyanide was produced at a rate of $r_{total} = 280 \pm 60$ nM s^{-1} (Figure 7.7c). The current flowing in our μ-BPV at its peak power output (50 nA; Figure 7.4a) corresponds to ferrocyanide reduction rate of $r_{single\text{-}channel} = 1.3$ pmol s^{-1}. I can therefore estimate the total number of channels required for converting all the charged-up electron carrier into current, N, as

$$N = \frac{r_{total}}{r_{single\text{-}channel}} = \frac{0.28\ \mu M\ s^{-1}\ \cdot\ 3\ mL}{1.3\ pmol\ s^{-1}} = 1620 \tag{7.10}$$

With the area of a single electrode being $A_{anode} = 0.08$ mm^2, the total area required for harvesting the power is $A_{power\text{-}delivery} = 1.3$ cm^2, indicating that in the current work the area required for illumination was of a similar size to the area required for power generation.

As there is no requirement for the power generation area to be exposed to sunlight, the illumination unit can be for instance be positioned above the power generation unit as illustrated in Figure 7.8. I further note that in our experiments the geometry of the illumination unit was not optimised; generation of larger quantities of the reduced electron carrier molecules is possible (e.g. by using a deeper vessel), and the illumination area is thus not the limiting area in the scalability consideration. As such, comparison of power densities normalised by the power delivery area is an effective measure for understanding the scalability of the system.

The current system used a platinum wire as cathode, given its previously proven catalytic activity for the re-generation of water. I tested whether a platinum plated wire could be used instead of a platinum wire and found that whilst reducing the total cost of the system the maximum power output of the system was indeed unaffected. Platinum plated steel wires are available at a price of \$0.02 per hundred metres (\$35/kg). Using a conservative

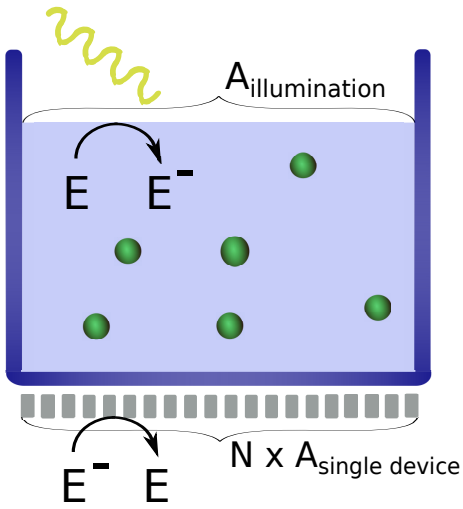

Fig. 7.8 By measuring the rate of ferrocyanide generation by the exoelectrogenic electrons released by *Synechocystis* cells, the area required for this process was found to be of the same size as the area required for converting these charged carriers to current. As there is no requirement to expose the power generation unit to light, I propose placing it underneath the charging unit.

estimate of a few centimetres of wire per chip, the cost of the amount of wire needed for a thousand microfluidic chips is below a cent which is significantly smaller than the cost of a microfluidic chip itself. Hence the use of platinum plated wires provides a promising approach for reducing the cost of the system. Additionally, non-platinum based materials have been shown to function effectively as the cathodic catalysts in microbial fuel cells [271, 272] and in BPVs [273], providing an alternative strategy for reducing the cost of the system.

7.4 Discussion

In order to compare devices of different dimensions, current and power outputs are commonly normalised to the active surface area of the anode where the phototrophic cells are located [250, 264]. As described in Section 7.3.5, for the two-chambered devices used in this study, the areas involved in the power generation and the charging processes are of similar sizes. As there is no requirement for the power generation area to be exposed to the sunlight, I can use the former as the larger one of the two areas as a measure for estimating the power density of the system and comparing the power outputs of the devices to previously described systems. Using this approach, the peak power density for the described BPVs can be estimated to be around (0.27 ± 0.03) W m^{-2} with the wild-type and (0.53 ± 0.05) W m^{-2} with the mutant cells, both at chlorophyll concentrations of $c_{chl} = 40$ μM. To the best of

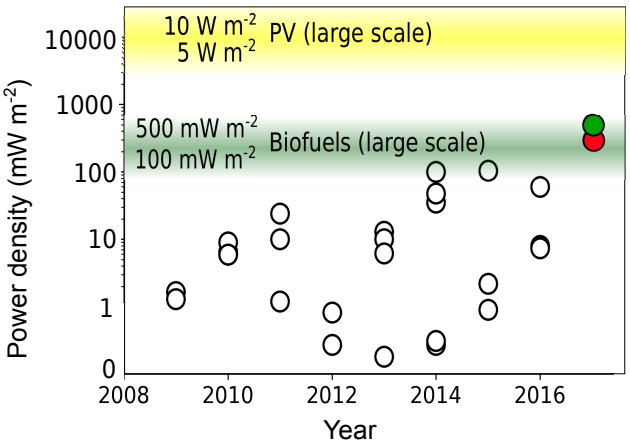

Fig. 7.9 Comparison of the devices demonstrated in this work to previous BPV and other power generation systems. The obtained power outputs are the highest BPV power densities recorded to date - white markers correspond to previously described devices [251] and the red and green marker to the device described in this work with wild-type ((0.27 ± 0.03) W m^{-2}) and mutant cells (0.53 ± 0.05) W m^{-2}, respectively. These values are similar to the power outputs of large scale biofuels and a factor of 10 to 20 lower than for large scale PVs [275–277].

our knowledge these values exceed that of previously demonstrated BPVs by two and a half fold and by fivefold, respectively (Figure 7.9; [251]).

The several-fold improvement over previously described devices achieved in this work combined with the advantages of BPVs, such as potentially cheap manufacturing and use of self-replicating catalysts, indicate that when scaled up via parallelisation, flow-BPVs could be a promising strategy for producing competitive analogues to synthetic photovoltaics (Figure 7.9). Moreover, even without parallelisation, the power outputs an individual device is sufficient for operating ultra-low power nanoelectronics, such as nanowire biosensors and their small size could allow them to be used to build self-sustaining ystems via on-chip integration [263, 274]. The decoupling “division-of-unit-processes” strategy described here could potentially also be applied to non-biological photovoltaics or to hybrid devices where conventional synthetic photovoltaic materials are employed in the charging process and an independently optimised electrocatalytic process in the electrochemical conversion unit.

7.5 Conclusion

In conclusion, I described and demonstrated a flow-based BPV system where the charging and the power generation units are spatially decoupled from another. In contrast to previously described devices, such decoupling provides temporal flexibility in power generation and the opportunity to independently optimise the geometry and the conditions needed for the light harvesting and the power generation processes. In particular, the use of microscale channels in the power generation unit enabled me to separate the anolyte and catholyte streams and dispense with the membranes, simplifying fabrication. Using this device, I achieved a two and a half fold improvement over the highest power outputs recorded in any BPV using wild-type cells and a fivefold improvement using a novel strain deficient in several electron sinks. I envisage microscale devices to be a promising approach to optimise BPVs, thus opening a path towards fulfilling their potential as a cheap and environmentally friendly complement to non-biological photovoltaics.

Chapter 8

Conclusions and future directions

In this thesis, I demonstrated a range of micron scale devices and used them for analysing the behaviour of biological systems, mostly proteins, both *in vitro* and *in vivo*. Specifically, I made use of the diffusion controlled behaviour of molecules in confined environments to build devices that allowed quantitative analysis of proteins, protein interactions and complexes, and protein self-assembly directly in solution and at previously unprecedented timescales and resolutions.

The self-assembly of proteins is a process that has been associated with the onset of a number of disorders and it has also been employed actively for controlling the nanoscale structure and properties of new materials. By exploiting the possibility to spatially decouple processes while keeping them fluidically integrated, I built a microscale device for monitoring the progression of aggregation in real time. In contrast to previously described high throughput approaches, in these devices the aggregation process was tracked without the presence of probe molecules in the reaction environment, which eliminated any potential interactions between the probe molecules and the aggregation process. This principle of spatially decoupling chemical reactions from measurements could also be applied to other biochemical and biophysical characterisation, where it is desirable to avoid interactions between the process and measurement probes.

These devices enabled effective tracking of the total amount of aggregated protein species, which can provide useful information on the aggregation process and kinetics. To gain further insight into this process, it is highly desirable to have access to platforms that provide size-resolved information about the compositions of self-assembling mixtures of proteins. However, there is currently a lack of experimental tools that permit effective characterisation self-assembling protein mixtures or, in fact, heterogeneous mixtures of biomolecules more generally. Indeed, existing platforms do not operate in liquid phase, which prevents their use

for analysing self-assembled protein complexes, as such larger species can obstruct the pores of the matrices that conventional separation platforms employ for keeping analyte bands confined.

To overcome these limitations and provide a strategy for separating biomolecules directly in liquid, I used micron scale separation devices where mixing can be prevented and orderly separation achieved without the involvement of matrices. Specifically, I addressed two limitations at the core of engineering such platforms. First, I devised and implemented a strategy for integrating strong electric fields with micron scale channels. I achieved this objective by the use of liquid electrodes that effectively transported away all electrolysis products from the microfluidic chip before they came into contact with the micron scale channels and perturbed the flow profiles in these channels. Secondly, I investigated the main factors that contribute to the limited resolution limit of micron scale platforms and demonstrated a strategy to increase several times the resolution of micron scale separation platforms. This result was achieved by spatially controlling sample injection and thereby enabling simultaneous suppression of the factors otherwise responsible for the limited resolution. Moreover, I combined this separation platform with a direct on chip protein sizing. This combined platform allowed me to increase substantially the resolution limit of the downstream analytical technique and to measure the sizes of proteins in mixtures that to the best of my knowledge cannot be characterised with any existing sizing approach. Additionally, due to the quantitative nature of the separation process, the strategy enabled me to obtain multidimensional data on mixtures of proteins directly in solution on a second to minute timescale.

In addition to *in vitro* biomolecular systems, I also used micron scale flow engineering approaches for analysing protein behaviour inside cells. Specifically, I demonstrated a platform for detecting intracellular proteins inside individual cells across a large number of cells. The presented work was concerned with detecting only a single target but the barcoding strategy that I described can be extended straightforwardly to analysing a virtually unlimited number of targets in parallel, overcoming the central limitation of existing single cell protein analysis tools. The specific purification strategies that I used, enabled me to access intracellular protein targets, which have not been previously detected in single cells in a highly multiplexed and a high throughput manner.

Finally, I used the ability to tightly control fluid movement and molecular motion in micron scale channels to build a conceptually new type of biological solar cell. This system relied on photosynthetic cells for generating excited electrons that could be converted into electrical current. By spatially decoupling the two key processes involved in the operation of a solar cell - the generation of excited charge carriers and their conversion into current - I was able to optimise the performance of these two processes independently. In so doing, I achieved

an enhancement which many times exceeded the power densities of previously described biophotovoltaic systems. The strategy to decouple charge generation and power delivery spatially additionally equipped the system with a temporal flexibility in power generation, which has been viewed as one of the key drawbacks of previous photovoltaic devices.

I envisage a broad range of applications for the microfluidic strategies described in this thesis. In particular, I am continuing to use the rapid in-solution separation approach for probing highly dynamic and heterogeneous biological systems. I have been delighted to see the interest that this work has generated both academically among my collaborators and commercially. The multidimensional protein characterisation strategy forms the basis of an explorative protein analysis and identification platform that I am hoping to have demonstrated soon. I am very interested in using the latter approach for further analysing protein behaviour and interactions inside a complex cellular environment, providing an orthogonal strategy for single cell proteomic analysis to the one that I described in this thesis that could be performed in a sequencing-free and in a probe-free manner.

Appendix A

Generation of electron transport chain mutants

A.1 Plasmid construction

The primers used in this study are listed in Table A.1. PCR was performed by standard procedures using Phusion high fidelity DNA polymerase (NEB). The genome sequence of *Synechocystis* sp. PCC6803 was consulted via Cyanobase (http://genome.kazusa.or.jp/cyanobase) for primer design [278]. Gene deletion of *flv2* was performed by amplifying a 912bp fragment upstream of *flv2* using primers Flv2leftfor and Flv2leftrev and a 972bp fragment downstream of *flv2* using primers Flv2rightfor and Flv2rightrev, followed by insertion of the respective fragments into the *Sac*I/*Eco*RI and *Xba*I/*Bam*HI sites of pUC19 to generate pFlv2-1. Gene deletion of *flv3* was performed by amplifying a 918bp fragment upstream of *flv3* using primers Flv3leftfor and Flv3leftrev and a 964bp fragment downstream of *flv3* using primers Flv3rightfor and Flv3rightrev, followed by insertion of the respective fragments into the *Sac*I/*Eco*RI and *Xba*I/*Bam*HI sites of pUC19 to generate Flv3-1. The *Bam*HI digested *npt*1/*sac*RB cassette from pUM24Cm was inserted into the *Bam*HI site between the upstream and downstream fragments in pFlv2-1 and pFlv3-1 to generate pFlv2-2 and pFlv3-2 respectively [279].

A.2 Generation of recombinant strains of *Synechocystis* sp. PCC 6803

Unmarked mutants of *Synechocystis* lacking Flv2 and Flv3 were constructed by disruption of *flv2* and *flv3*, respectively, in the terminal oxidase mutant deficient strain via a two step

Table A.1 Sequence of primers used in this study.*

Primer name	Sequence (5' to 3')
Flv2leftfor	GATCGAATTCGCGTTGCTGGTTATCCAAGT
Flv2leftrev	GATCGAGCTCGGAGTGTACGGCGTCATTTT
Flv2rightfor	GATCGGATCCAAGCTGGGCTAAATCCAAA
Flv2leftrev	GCATTCTAGAGCACCATACAAACTGGACGA
Flv3leftf	GATCGAATTCGGTGTTCAGCGGTTACTTA
Flv3leftr	GATCGGATCCGCGCTAGCCTATTTGGAGTG
Flv3rightf	GATCGGATCCCAGTCCAAAGAACGGATA
Flv3leftr	GCATTCTAGAGGGAAAAGGGTGGGATGTAT
Flv2for	GCCGTTGGGTTGTAACACTT
Flv2rev	GTTTCCATCGGAGTTGCAGT
Flv3for	GCGGTTTGATTGCAGTTTTT
Flv3rev	GGGGAAAGCATCATGTATCG

homologous recombination protocol [123]. To generate marked mutants approximately 1 μg of plasmids pFlv2-2 and pFlv3-2 were mixed with *Synechocystis* cells for 6 hours in liquid medium, followed by incubation on BG-11 agar plates for approximately 24 hours. An additional 3 mL of agar containing kanamycin was added to the surface of the plate followed by further incubation for approximately 1-2 weeks. Transformants were subcultured to allow segregation of mutant alleles. Segregation was confirmed by PCR using primers Flv2f/Flv2r, or Flv3f/Flv3r, which flank the deleted region. Generation of unmarked mutants was carried out according to Lea-Smith et al. [269]. To remove the *npt1/sac*RB cassette, mutant lines were transformed with 1 μg of the markerless pFlv2-1 and pFlv3-1 constructs. Following incubation in BG-11 liquid medium for 4 days and on agar plates containing sucrose (5% w/v) for a further 1-2 weeks, transformants were patched on kanamycin and sucrose plates. Sucrose resistant, kanamycin sensitive strains containing the unmarked deletion were confirmed by PCR using primers flanking the deleted region (Fig. A.1).

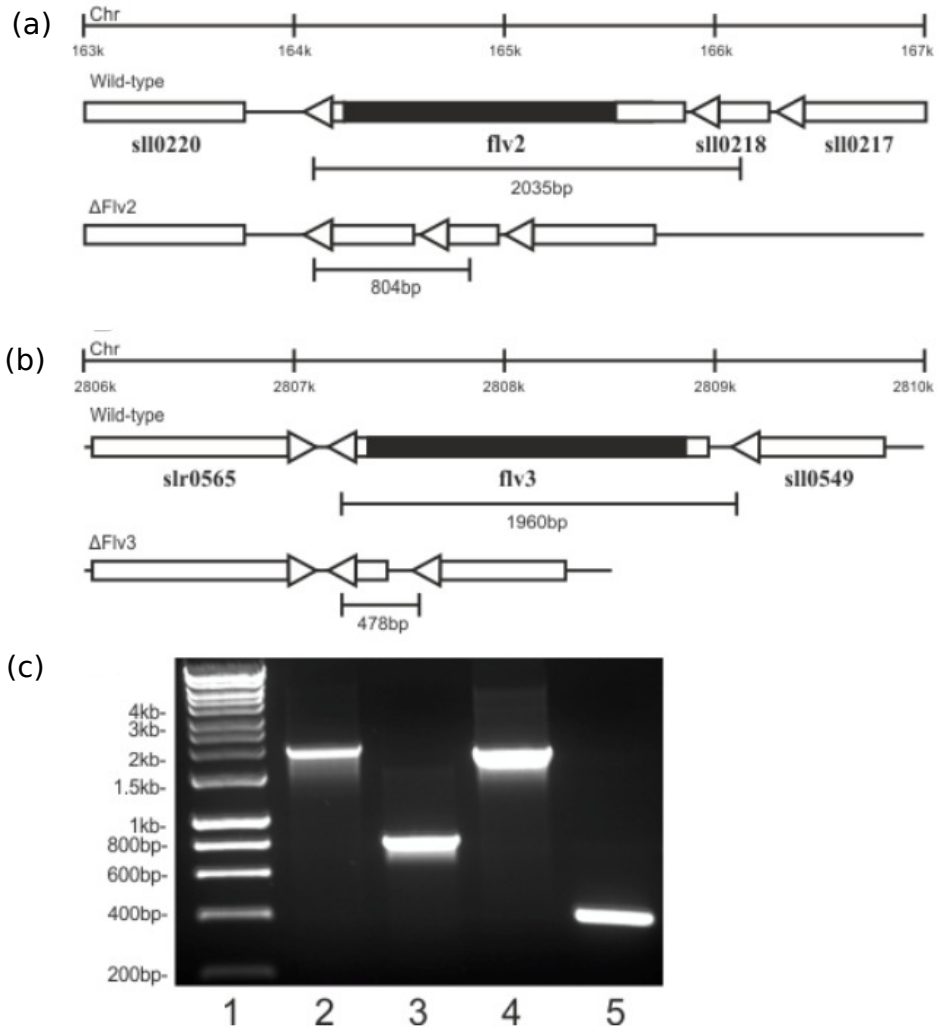

Fig. A.1 Schematic representations of locus location in the *Synechocystis* sp. PCC6803 genome (top) and the wild type (middle) and unmarked knockouts (bottom) profiles expected in **(a)** ΔFlv2 and **(b)** ΔFlv3 strains following amplification with primers flanking the deleted sequence. Regions deleted in the mutant strains are shaded in black. **(c)** Amplification of genomic DNA in wild type cells (lane 2) and Δ*Flv2* (lane 3) using Flv2f and Flv2r primers; in wild type (lane 4) and *Flv3* (lane 5) using Flv3f and Flv3r primers. DNA marker ladder is in Lane 1.

References

[1] B. Alberts, "The cell as a collection of protein machines: preparing the next generation of molecular biologists," Cell, vol. 92, no. 3, pp. 291–294, 1998.

[2] J. M. Berg, J. L. Tymoczko, and L. Stryer, "Biochemistry, ; w. h," 2002.

[3] B. Alberts, "The cell as a collection of protein machines: preparing the next generation of molecular biologists," Cell, vol. 92, no. 3, pp. 291–294, 1998.

[4] C. M. Dobson, "Protein folding and misfolding," Nature, vol. 426, no. 6968, p. 884, 2003.

[5] F. Chiti and C. M. Dobson, "Protein misfolding, functional amyloid, and human disease," Annu. Rev. Biochem., vol. 75, pp. 333–366, 2006.

[6] S. B. Prusiner, "Molecular biology of prion diseases," Science, vol. 252, no. 5012, pp. 1515–1522, 1991.

[7] T. P. Knowles, M. Vendruscolo, and C. M. Dobson, "The amyloid state and its association with protein misfolding diseases," Nature reviews Molecular cell biology, vol. 15, no. 6, p. 384, 2014.

[8] R. J. Ellis, "Macromolecular crowding: an important but neglected aspect of the intracellular environment," Current opinion in structural biology, vol. 11, no. 1, pp. 114–119, 2001.

[9] S. Mittal, R. K. Chowhan, and L. R. Singh, "Macromolecular crowding: Macromolecules friend or foe," Biochimica et Biophysica Acta (BBA)-General Subjects, vol. 1850, no. 9, pp. 1822–1831, 2015.

[10] G. Rivas and A. P. Minton, "Macromolecular crowding in vitro, in vivo, and in between," Trends in biochemical sciences, vol. 41, no. 11, pp. 970–981, 2016.

[11] A. F. Neuwald, L. Aravind, J. L. Spouge, and E. V. Koonin, "Aaa+: A class of chaperone-like atpases associated with the assembly, operation, and disassembly of protein complexes," Genome research, vol. 9, no. 1, pp. 27–43, 1999.

[12] L. T. Bergendahl and J. A. Marsh, "Functional determinants of protein assembly into homomeric complexes," Scientific reports, vol. 7, no. 1, p. 4932, 2017.

[13] I. S. Moreira, P. A. Fernandes, and M. J. Ramos, "Hot spots?a review of the protein–protein interface determinant amino-acid residues," Proteins: Structure, Function, and Bioinformatics, vol. 68, no. 4, pp. 803–812, 2007.

[14] C. V. Robinson, A. Sali, and W. Baumeister, "The molecular sociology of the cell," Nature, vol. 450, no. 7172, p. 973, 2007.

[15] W. E. Balch, R. I. Morimoto, A. Dillin, and J. W. Kelly, "Adapting proteostasis for disease intervention," science, vol. 319, no. 5865, pp. 916–919, 2008.

[16] E. V. Yates, T. Müller, L. Rajah, E. J. De Genst, P. Arosio, S. Linse, M. Vendruscolo, C. M. Dobson, and T. P. Knowles, "Latent analysis of unmodified biomolecules and their complexes in solution with attomole detection sensitivity," Nature chemistry, vol. 7, no. 10, p. 802, 2015.

[17] T. Berggård, S. Linse, and P. James, "Methods for the detection and analysis of protein–protein interactions," Proteomics, vol. 7, no. 16, pp. 2833–2842, 2007.

[18] L. Ou-Yang, D.-Q. Dai, X.-L. Li, M. Wu, X.-F. Zhang, and P. Yang, "Detecting temporal protein complexes from dynamic protein-protein interaction networks," BMC bioinformatics, vol. 15, no. 1, p. 335, 2014.

[19] C. Schmidt and C. V. Robinson, "Dynamic protein ligand interactions–insights from ms," The FEBS journal, vol. 281, no. 8, pp. 1950–1964, 2014.

[20] V. Csizmok, A. V. Follis, R. W. Kriwacki, and J. D. Forman-Kay, "Dynamic protein interaction networks and new structural paradigms in signaling," Chemical reviews, vol. 116, no. 11, pp. 6424–6462, 2016.

[21] J. C. Kendrew, G. Bodo, H. M. Dintzis, R. Parrish, H. Wyckoff, and D. C. Phillips, "A three-dimensional model of the myoglobin molecule obtained by x-ray analysis," Nature, vol. 181, no. 4610, pp. 662–666, 1958.

[22] J. L. Jiménez, E. J. Nettleton, M. Bouchard, C. V. Robinson, C. M. Dobson, and H. R. Saibil, "The protofilament structure of insulin amyloid fibrils," Proceedings of the National Academy of Sciences, vol. 99, no. 14, pp. 9196–9201, 2002.

[23] A. Ben-Shem, N. G. de Loubresse, S. Melnikov, L. Jenner, G. Yusupova, and M. Yusupov, "The structure of the eukaryotic ribosome at 3.0 å resolution," Science, vol. 334, no. 6062, pp. 1524–1529, 2011.

[24] A. W. Fitzpatrick, G. T. Debelouchina, M. J. Bayro, D. K. Clare, M. A. Caporini, V. S. Bajaj, C. P. Jaroniec, L. Wang, V. Ladizhansky, S. A. Müller, et al., "Atomic structure and hierarchical assembly of a cross-β amyloid fibril," Proceedings of the National Academy of Sciences, p. 201219476, 2013.

[25] H. Khatter, A. G. Myasnikov, S. K. Natchiar, and B. P. Klaholz, "Structure of the human 80s ribosome," Nature, vol. 520, no. 7549, p. 640, 2015.

[26] X.-C. Bai, G. McMullan, and S. H. Scheres, "How cryo-em is revolutionizing structural biology," Trends in biochemical sciences, vol. 40, no. 1, pp. 49–57, 2015.

[27] A. Yonath, "X-ray crystallography at the heart of life science," Current Opinion in Structural Biology, vol. 21, no. 5, pp. 622–626, 2011.

[28] A. Amunts, A. Brown, X.-c. Bai, J. L. Llácer, T. Hussain, P. Emsley, F. Long, G. Murshudov, S. H. Scheres, and V. Ramakrishnan, "Structure of the yeast mitochondrial large ribosomal subunit," Science, vol. 343, no. 6178, pp. 1485–1489, 2014.

[29] B. Berne and R. Pecora, "Dynamic light scattering with applications to chemistry, biology and physics. willey-interscience," 1976.

[30] E. L. Elson and D. Magde, "Fluorescence correlation spectroscopy. i. conceptual basis and theory," Biopolymers: Original Research on Biomolecules, vol. 13, no. 1, pp. 1–27, 1974.

[31] R. Rigler and E. S. Elson, Fluorescence correlation spectroscopy: theory and applications, vol. 65. Springer Science & Business Media, 2012.

[32] D. K. Wilkins, S. B. Grimshaw, V. Receveur, C. M. Dobson, J. A. Jones, and L. J. Smith, "Hydrodynamic radii of native and denatured proteins measured by pulse field gradient nmr techniques," Biochemistry, vol. 38, no. 50, pp. 16424–16431, 1999.

[33] P. Sengupta, K. Garai, J. Balaji, N. Periasamy, and S. Maiti, "Measuring size distribution in highly heterogeneous systems with fluorescence correlation spectroscopy," Biophysical journal, vol. 84, no. 3, pp. 1977–1984, 2003.

[34] M. Chakraborty, A. M. Kuriata, J. N. Henderson, M. E. Salvucci, R. M. Wachter, and M. Levitus, "Protein oligomerization monitored by fluorescence fluctuation spectroscopy: self-assembly of rubisco activase," Biophysical journal, vol. 103, no. 5, pp. 949–958, 2012.

[35] T. Scheibel and L. C. Serpell, "Structural analysis of fibrous proteins," Protein Science Encyclopedia: online, pp. 197–253, 2008.

[36] P. Arosio, T. Mueller, L. Rajah, E. V. Yates, F. A. Aprile, Y. Zhang, S. I. Cohen, D. A. White, T. W. Herling, E. J. De Genst, et al., "Microfluidic diffusion analysis of the sizes and interactions of proteins under native solution conditions," ACS nano, vol. 10, no. 1, pp. 333–341, 2015.

[37] Y. Zhang, A. K. Buell, T. Müller, E. De Genst, J. Benesch, C. M. Dobson, and T. P. Knowles, "Protein aggregate-ligand binding assays based on microfluidic diffusional separation," ChemBioChem, vol. 17, no. 20, pp. 1920–1924, 2016.

[38] Y. Zhang, E. V. Yates, L. Hong, K. L. Saar, G. Meisl, C. M. Dobson, and T. P. Knowles, "On-chip measurements of protein unfolding from direct observations of micron-scale diffusion," Chemical Science, 2018.

[39] W. S. Price, "Pulsed-field gradient nuclear magnetic resonance as a tool for studying translational diffusion: Part 1. basic theory," Concepts in Magnetic Resonance: An Educational Journal, vol. 9, no. 5, pp. 299–336, 1997.

[40] L. E. Kay, "Nmr studies of protein structure and dynamics," Journal of Magnetic Resonance, vol. 213, no. 2, pp. 477–491, 2011.

[41] M. Calero and M. Gasset, "Fourier transform infrared and circular dichroism spectroscopies for amyloid studies," in Amyloid Proteins, pp. 129–151, Springer, 2005.

[42] A. Barth, "Infrared spectroscopy of proteins," Biochimica et Biophysica Acta (BBA)-Bioenergetics, vol. 1767, no. 9, pp. 1073–1101, 2007.

[43] S. M. Kelly, T. J. Jess, and N. C. Price, "How to study proteins by circular dichroism," Biochimica et Biophysica Acta (BBA)-Proteins and Proteomics, vol. 1751, no. 2, pp. 119–139, 2005.

[44] J. A. Aquilina, J. L. Benesch, L. L. Ding, O. Yaron, J. Horwitz, and C. V. Robinson, "Subunit exchange of polydisperse proteins: mass spectrometry reveals consequences of αa-crystallin truncation," Journal of Biological Chemistry, 2005.

[45] H. Ecroyd, S. Meehan, J. Horwitz, J. A. Aquilina, J. L. Benesch, C. V. Robinson, C. E. Macphee, and J. A. Carver, "Mimicking phosphorylation of αb-crystallin affects its chaperone activity," Biochemical Journal, vol. 401, no. 1, pp. 129–141, 2007.

[46] R. Aebersold and M. Mann, "Mass-spectrometric exploration of proteome structure and function," Nature, vol. 537, no. 7620, p. 347, 2016.

[47] S. Mehmood, T. M. Allison, and C. V. Robinson, "Mass spectrometry of protein complexes: from origins to applications," Annual review of physical chemistry, vol. 66, pp. 453–474, 2015.

[48] J. L. Benesch, J. A. Aquilina, B. T. Ruotolo, F. Sobott, and C. V. Robinson, "Tandem mass spectrometry reveals the quaternary organization of macromolecular assemblies," Chemistry & biology, vol. 13, no. 6, pp. 597–605, 2006.

[49] F. Stengel, A. J. Baldwin, A. J. Painter, N. Jaya, E. Basha, L. E. Kay, E. Vierling, C. V. Robinson, and J. L. Benesch, "Quaternary dynamics and plasticity underlie small heat shock protein chaperone function," Proceedings of the National Academy of Sciences, vol. 107, no. 5, pp. 2007–2012, 2010.

[50] K. Contrepois, L. Jiang, and M. Snyder, "Optimized analytical procedures for the untargeted metabolomic profiling of human urine and plasma by combining hydrophilic interaction and reverse-phase liquid chromatography-mass spectrometry," Molecular & Cellular Proteomics, pp. mcp–M114, 2015.

[51] Y.-A. Song, M. Chan, C. Celio, S. R. Tannenbaum, J. S. Wishnok, and J. Han, "Free-flow zone electrophoresis of peptides and proteins in pdms microchip for narrow pi range sample prefractionation coupled with mass spectrometry," Analytical chemistry, vol. 82, no. 6, pp. 2317–2325, 2010.

[52] J. L. Benesch, B. T. Ruotolo, D. A. Simmons, and C. V. Robinson, "Protein complexes in the gas phase: technology for structural genomics and proteomics," Chemical reviews, vol. 107, no. 8, pp. 3544–3567, 2007.

[53] A. J. Baldwin, H. Lioe, C. V. Robinson, L. E. Kay, and J. L. Benesch, "αb-crystallin polydispersity is a consequence of unbiased quaternary dynamics," Journal of molecular biology, vol. 413, no. 2, pp. 297–309, 2011.

[54] A. C. Leney and A. J. Heck, "Native mass spectrometry: what is in the name?," Journal of the American Society for Mass Spectrometry, vol. 28, no. 1, pp. 5–13, 2017.

[55] S. Scarano, M. Mascini, A. P. Turner, and M. Minunni, "Surface plasmon resonance imaging for affinity-based biosensors," Biosensors and bioelectronics, vol. 25, no. 5, pp. 957–966, 2010.

[56] S. G. Patching, "Surface plasmon resonance spectroscopy for characterisation of membrane protein–ligand interactions and its potential for drug discovery," Biochimica et Biophysica Acta (BBA)-Biomembranes, vol. 1838, no. 1, pp. 43–55, 2014.

[57] M. C. Jecklin, S. Schauer, C. E. Dumelin, and R. Zenobi, "Label-free determination of protein–ligand binding constants using mass spectrometry and validation using surface plasmon resonance and isothermal titration calorimetry," Journal of Molecular Recognition, vol. 22, no. 4, pp. 319–329, 2009.

[58] M. Jiao, H.-T. Li, J. Chen, A. P. Minton, and Y. Liang, "Attractive protein-polymer interactions markedly alter the effect of macromolecular crowding on protein association equilibria," Biophysical journal, vol. 99, no. 3, pp. 914–923, 2010.

[59] J. Concepcion, K. Witte, C. Wartchow, S. Choo, D. Yao, H. Persson, J. Wei, P. Li, B. Heidecker, W. Ma, et al., "Label-free detection of biomolecular interactions using biolayer interferometry for kinetic characterization," Combinatorial chemistry & high throughput screening, vol. 12, no. 8, pp. 791–800, 2009.

[60] T. Sun, F. Reid, Y. Liu, Y. Cao, P. Estep, C. Nauman, and Y. Xu, "High throughput detection of antibody self-interaction by bio-layer interferometry," in MAbs, vol. 5, pp. 838–841, Taylor & Francis, 2013.

[61] D. Frenzel and D. Willbold, "Kinetic titration series with biolayer interferometry," PloS one, vol. 9, no. 9, p. e106882, 2014.

[62] L. Nevola and E. Giralt, "Modulating protein–protein interactions: the potential of peptides," Chemical Communications, vol. 51, no. 16, pp. 3302–3315, 2015.

[63] C. J. Wienken, P. Baaske, U. Rothbauer, D. Braun, and S. Duhr, "Protein-binding assays in biological liquids using microscale thermophoresis," Nature communications, vol. 1, p. ncomms1093, 2010.

[64] T. Huxford, "Measuring equilibrium binding affinity of biological macromolecules in solution by thermophoresis," tech. rep., San Diego State University Foundation San Diego United States, 2015.

[65] T. Bartoschik, S. Galinec, C. Kleusch, K. Walkiewicz, D. Breitsprecher, S. Weigert, Y. A. Muller, C. You, J. Piehler, T. Vercruysse, et al., "Near-native, site-specific and purification-free protein labeling for quantitative protein interaction analysis by microscale thermophoresis," Scientific reports, vol. 8, no. 1, p. 4977, 2018.

[66] A. Voller, D. Bidwell, et al., The enzyme linked immunosorbent assay (ELISA). Vol. 2. A review of recent developments with abstracts of microplate applications. MicroSystems Ltd, Summerfield House, Vale, Guernsey, Channel Islands, 1980.

[67] R. M. Lequin, "Enzyme immunoassay (eia)/enzyme-linked immunosorbent assay (elisa)," Clinical chemistry, vol. 51, no. 12, pp. 2415–2418, 2005.

[68] W. N. Burnette, "?western blotting?: electrophoretic transfer of proteins from sodium dodecyl sulfate-polyacrylamide gels to unmodified nitrocellulose and radiographic detection with antibody and radioiodinated protein a," Analytical biochemistry, vol. 112, no. 2, pp. 195–203, 1981.

[69] D. J. MacPhee, "Methodological considerations for improving western blot analysis," Journal of pharmacological and toxicological methods, vol. 61, no. 2, pp. 171–177, 2010.

[70] T. Mahmood and P.-C. Yang, "Western blot: technique, theory, and trouble shooting," North American journal of medical sciences, vol. 4, no. 9, p. 429, 2012.

[71] S. Fredriksson, M. Gullberg, J. Jarvius, C. Olsson, K. Pietras, S. M. Gústafsdóttir, A. Östman, and U. Landegren, "Protein detection using proximity-dependent dna ligation assays," Nature biotechnology, vol. 20, no. 5, p. 473, 2002.

[72] C. Greenwood, D. Ruff, S. Kirvell, G. Johnson, H. S. Dhillon, and S. A. Bustin, "Proximity assays for sensitive quantification of proteins," Biomolecular detection and quantification, vol. 4, pp. 10–16, 2015.

[73] W. E. Arter, J. Charmet, J. Kong, K. L. Saar, T. W. Herling, T. Müller, U. F. Keyser, and T. P. Knowles, "Combining affinity selection and specific ion mobility for microchip protein sensing," Analytical Chemistry, vol. 90, no. 17, pp. 10302–10310, 2018.

[74] M. A. Wright, F. A. Aprile, P. Arosio, M. Vendruscolo, C. M. Dobson, and T. P. Knowles, "Biophysical approaches for the study of interactions between molecular chaperones and protein aggregates," Chemical Communications, vol. 51, no. 77, pp. 14425–14434, 2015.

[75] J. El-Ali, P. K. Sorger, and K. F. Jensen, "Cells on chips," Nature, vol. 442, no. 7101, p. 403, 2006.

[76] M. Rothbauer, H. Zirath, and P. Ertl, "Recent advances in microfluidic technologies for cell-to-cell interaction studies," Lab on a Chip, vol. 18, no. 2, pp. 249–270, 2018.

[77] E. W. Esch, A. Bahinski, and D. Huh, "Organs-on-chips at the frontiers of drug discovery," Nature reviews Drug discovery, vol. 14, no. 4, p. 248, 2015.

[78] M. Baker, "Tissue models: a living system on a chip," Nature, vol. 471, no. 7340, p. 661, 2011.

[79] N. S. Bhise, J. Ribas, V. Manoharan, Y. S. Zhang, A. Polini, S. Massa, M. R. Dokmeci, and A. Khademhosseini, "Organ-on-a-chip platforms for studying drug delivery systems," Journal of Controlled Release, vol. 190, pp. 82–93, 2014.

[80] T. Q. Vu, R. M. B. de Castro, and L. Qin, "Bridging the gap: microfluidic devices for short and long distance cell–cell communication," Lab on a Chip, vol. 17, no. 6, pp. 1009–1023, 2017.

[81] H. Lu, S. Gaudet, M. A. Schmidt, and K. F. Jensen, "A microfabricated device for subcellular organelle sorting," Analytical Chemistry, vol. 76, no. 19, pp. 5705–5712, 2004.

[82] G. Velve-Casquillas, M. Le Berre, M. Piel, and P. T. Tran, "Microfluidic tools for cell biological research," Nano today, vol. 5, no. 1, pp. 28–47, 2010.

[83] A. P. Patel, I. Tirosh, J. J. Trombetta, A. K. Shalek, S. M. Gillespie, H. Wakimoto, D. P. Cahill, B. V. Nahed, W. T. Curry, R. L. Martuza, et al., "Single-cell rna-seq highlights intratumoral heterogeneity in primary glioblastoma," Science, vol. 344, no. 6190, pp. 1396–1401, 2014.

[84] F. Buettner, K. N. Natarajan, F. P. Casale, V. Proserpio, A. Scialdone, F. J. Theis, S. A. Teichmann, J. C. Marioni, and O. Stegle, "Computational analysis of cell-to-cell heterogeneity in single-cell rna-sequencing data reveals hidden subpopulations of cells," Nature biotechnology, vol. 33, no. 2, p. 155, 2015.

[85] Y. Sasagawa, I. Nikaido, T. Hayashi, H. Danno, K. D. Uno, T. Imai, and H. R. Ueda, "Quartz-seq: a highly reproducible and sensitive single-cell rna sequencing method, reveals non-genetic gene-expression heterogeneity," Genome biology, vol. 14, no. 4, p. 3097, 2013.

[86] T. S. Watkins and J. J. Miles, "Tracking the t-cell repertoire after adoptive therapy," Clinical & translational immunology, vol. 6, no. 5, p. e140, 2017.

[87] A. K. Shalek and M. Benson, "Single-cell analyses to tailor treatments," Science translational medicine, vol. 9, no. 408, 2017.

[88] P. Oh, K. Hockemeyer, R. Satija, and I. Aifantis, "Characterization of treatment effects on the tumor microenvironment using single cell rna sequencing," International Journal of Radiation Oncology? Biology? Physics, vol. 99, no. 2, p. S203, 2017.

[89] M. Yamaji, M. Jishage, C. Meyer, H. Suryawanshi, E. Der, M. Yamaji, A. Garzia, P. Morozov, S. Manickavel, H. L. McFarland, et al., "Dnd1 maintains germline stem cells via recruitment of the ccr4–not complex to target mrnas," Nature, vol. 543, no. 7646, p. 568, 2017.

[90] W. Stephenson, L. T. Donlin, A. Butler, C. Rozo, B. Bracken, A. Rashidfarrokhi, S. M. Goodman, L. B. Ivashkiv, V. P. Bykerk, D. E. Orange, et al., "Single-cell rna-seq of rheumatoid arthritis synovial tissue using low-cost microfluidic instrumentation," Nature communications, vol. 9, no. 1, p. 791, 2018.

[91] K. D. Birnbaum, "Power in numbers: Single-cell rna-seq strategies to dissect complex tissues," Annual review of genetics, no. 0, 2018.

[92] H. A. Stone and S. Kim, "Microfluidics: basic issues, applications, and challenges," AIChE Journal, vol. 47, no. 6, pp. 1250–1254, 2001.

[93] T. W. Herling, A. Levin, K. L. Saar, C. M. Dobson, and T. P. Knowles, "Microfluidic approaches for probing amyloid assembly and behaviour," Lab on a Chip, vol. 18, no. 7, pp. 999–1016, 2018.

[94] D. R. Reyes, D. Iossifidis, P.-A. Auroux, and A. Manz, "Micro total analysis systems. 1. introduction, theory, and technology," Analytical chemistry, vol. 74, no. 12, pp. 2623–2636, 2002.

[95] P.-A. Auroux, D. Iossifidis, D. R. Reyes, and A. Manz, "Micro total analysis systems. 2. analytical standard operations and applications," Analytical chemistry, vol. 74, no. 12, pp. 2637–2652, 2002.

[96] G. M. Whitesides, "The origins and the future of microfluidics," Nature, vol. 442, no. 7101, p. 368, 2006.

[97] M. L. Kovarik, D. M. Ornoff, A. T. Melvin, N. C. Dobes, Y. Wang, A. J. Dickinson, P. C. Gach, P. K. Shah, and N. L. Allbritton, "Micro total analysis systems: fundamental advances and applications in the laboratory, clinic, and field," Analytical chemistry, vol. 85, no. 2, pp. 451–472, 2012.

[98] Á. Ríos, M. Zougagh, and M. Avila, "Miniaturization through lab-on-a-chip: Utopia or reality for routine laboratories? a review," Analytica Chimica Acta, vol. 740, pp. 1–11, 2012.

[99] S. Zilberzwige-Tal and E. Gazit, "Go with the flow-microfluidics approaches for amyloids research," Chemistry–An Asian Journal, 2018.

[100] S. Tia and A. E. Herr, "On-chip technologies for multidimensional separations," Lab on a Chip, vol. 9, no. 17, pp. 2524–2536, 2009.

[101] E. R. Castro and A. Manz, "Present state of microchip electrophoresis: state of the art and routine applications," Journal of Chromatography A, vol. 1382, pp. 66–85, 2015.

[102] D. J. Harrison, A. Manz, Z. Fan, H. Luedi, and H. M. Widmer, "Capillary electrophoresis and sample injection systems integrated on a planar glass chip," Analytical chemistry, vol. 64, no. 17, pp. 1926–1932, 1992.

[103] D. C. Duffy, J. C. McDonald, O. J. Schueller, and G. M. Whitesides, "Rapid prototyping of microfluidic systems in poly (dimethylsiloxane)," Analytical chemistry, vol. 70, no. 23, pp. 4974–4984, 1998.

[104] J. C. McDonald and G. M. Whitesides, "Poly (dimethylsiloxane) as a material for fabricating microfluidic devices," Accounts of chemical research, vol. 35, no. 7, pp. 491–499, 2002.

[105] E. K. Sackmann, A. L. Fulton, and D. J. Beebe, "The present and future role of microfluidics in biomedical research," Nature, vol. 507, no. 7491, p. 181, 2014.

[106] E. Brouzes, M. Medkova, N. Savenelli, D. Marran, M. Twardowski, J. B. Hutchison, J. M. Rothberg, D. R. Link, N. Perrimon, and M. L. Samuels, "Droplet microfluidic technology for single-cell high-throughput screening," Proceedings of the National Academy of Sciences, vol. 106, no. 34, pp. 14195–14200, 2009.

[107] V. Taly, B. T. Kelly, and A. D. Griffiths, "Droplets as microreactors for high-throughput biology," ChemBioChem, vol. 8, no. 3, pp. 263–272, 2007.

[108] M. T. Guo, A. Rotem, J. A. Heyman, and D. A. Weitz, "Droplet microfluidics for high-throughput biological assays," Lab on a Chip, vol. 12, no. 12, pp. 2146–2155, 2012.

[109] T. C. Michaels, A. J. Dear, J. B. Kirkegaard, K. L. Saar, D. A. Weitz, and T. P. Knowles, "Fluctuations in the kinetics of linear protein self-assembly," Physical review letters, vol. 116, no. 25, p. 258103, 2016.

[110] J. Charmet, P. Arosio, and T. P. Knowles, "Microfluidics for protein biophysics," Journal of molecular biology, 2017.

[111] T. P. Knowles, D. A. White, A. R. Abate, J. J. Agresti, S. I. Cohen, R. A. Sperling, E. J. De Genst, C. M. Dobson, and D. A. Weitz, "Observation of spatial propagation of amyloid assembly from single nuclei," Proceedings of the National Academy of Sciences, vol. 108, no. 36, pp. 14746–14751, 2011.

[112] M. Pfammatter, M. Andreasen, G. Meisl, C. G. Taylor, J. Adamcik, S. Bolisetty, A. Sánchez-Ferrer, D. Klenerman, C. M. Dobson, R. Mezzenga, et al., "Absolute quantification of amyloid propagons by digital microfluidics," Analytical chemistry, vol. 89, no. 22, pp. 12306–12313, 2017.

[113] D. Qin, Y. Xia, and G. M. Whitesides, "Soft lithography for micro- and nanoscale patterning," Nat. Protoc., vol. 5, no. 3, pp. 491–502, 2010.

[114] P. K. Challa, T. Kartanas, J. Charmet, and T. P. Knowles, "Microfluidic devices fabricated using fast wafer-scale led-lithography patterning," Biomicrofluidics, vol. 11, no. 1, p. 014113, 2017.

[115] S. H. Tan, N. T. Nguyen, Y. C. Chua, and T. G. Kang, "Oxygen plasma treatment for reducing hydrophobicity of a sealed polydimethylsiloxane microchannel," Biomicrofluidics, vol. 4, no. 3, pp. 1–8, 2010.

[116] Y. Y. Huang, T. P. J. Knowles, and E. M. Terentjev, "Strength of nanotubes, filaments, and nanowiresfrom sonication-induced scission," Adv. Mater., vol. 21, no. 38-39, pp. 3945–3948, 2009.

[117] D. M. Walsh, E. Thulin, A. M. Minogue, N. Gustavsson, E. Pang, D. B. Teplow, and S. Linse, "A facile method for expression and purification of the alzheimer's disease-associated amyloid β-peptide," The FEBS journal, vol. 276, no. 5, pp. 1266–1281, 2009.

[118] E. Hellstrand, B. Boland, D. M. Walsh, and S. Linse, "Amyloid β-protein aggregation produces highly reproducible kinetic data and occurs by a two-phase process," ACS chemical neuroscience, vol. 1, no. 1, pp. 13–18, 2009.

[119] H. Willander, J. Presto, G. Askarieh, H. Biverstål, B. Frohm, S. D. Knight, J. Johansson, and S. Linse, "Brichos domains efficiently delay fibrillation of amyloid β-peptide," Journal of Biological Chemistry, vol. 287, no. 37, pp. 31608–31617, 2012.

[120] M. Perni, C. Galvagnion, A. Maltsev, G. Meisl, M. B. Müller, P. K. Challa, J. B. Kirkegaard, P. Flagmeier, S. I. Cohen, R. Cascella, et al., "A natural product inhibits the initiation of α-synuclein aggregation and suppresses its toxicity," Proceedings of the National Academy of Sciences, vol. 114, no. 6, pp. E1009–E1017, 2017.

[121] J. G. Williams, "Construction of specific mutations in photosystem II photosynthetic reaction center by genetic engineering methods in Synechocystis 6803," Methods in Enzymology, vol. 167, pp. 766–778, 1988.

[122] R. W. Castenholz, "Culturing methods for cyanobacteria," Methods in Enzymology, vol. 167, pp. 68–93, 1988.

[123] D. J. Lea-Smith, N. Ross, M. Zori, D. S. Bendall, J. S. Dennis, S. A. Scott, A. G. Smith, and C. J. Howe, "Thylakoid terminal oxidases are essential for the cyanobacterium Synechocystis sp. PCC 6803 to survive rapidly changing light intensities," Plant Physiology, vol. 162, no. 1, pp. 484–495, 2013.

[124] T. Herling, T. Müller, L. Rajah, J. Skepper, M. Vendruscolo, and T. Knowles, "Integration and characterization of solid wall electrodes in microfluidic devices fabricated in a single photolithography step," Applied Physics Letters, vol. 102, no. 18, p. 184102, 2013.

[125] F. Oosawa and M. Kasai, "A theory of linear and helical aggregations of macromolecules," Journal of molecular biology, vol. 4, no. 1, pp. 10–21, 1962.

[126] E. Gazit, "Self-assembled peptide nanostructures: the design of molecular building blocks and their technological utilization," Chemical Society Reviews, vol. 36, no. 8, pp. 1263–1269, 2007.

[127] C. Li, S. Bolisetty, and R. Mezzenga, "Hybrid nanocomposites of gold single-crystal platelets and amyloid fibrils with tunable fluorescence, conductivity, and sensing properties," Advanced Materials, vol. 25, no. 27, pp. 3694–3700, 2013.

[128] S. J. Lee, H. S. Lim, E. Masliah, and H. J. Lee, "Protein aggregate spreading in neurodegenerative diseases: Problems and perspectives," Neuroscience Research, vol. 70, no. 4, pp. 339–348, 2011.

[129] D. Eisenberg and M. Jucker, "The amyloid state of proteins in human diseases," Cell, vol. 148, no. 6, pp. 1188–1203, 2012.

[130] K. H. Ashe and A. Aguzzi, "Prions, prionoids and pathogenic proteins in alzheimer disease," Prion, vol. 7, no. 1, pp. 55–59, 2013.

[131] I. Benilova, E. Karran, and B. De Strooper, "The toxic Aβ oligomer and Alzheimer's disease: an emperor in need of clothes," Nature Neuroscience, vol. 15, no. 3, pp. 349–357, 2012.

[132] C. Behl, "Brain aging and late-onset alzheimer's disease: many open questions," International psychogeriatrics, vol. 24, no. S1, pp. S3–S9, 2012.

[133] T. Morawe, C. Hiebel, A. Kern, and C. Behl, "Protein homeostasis, aging and Alzheimer's disease," Molecular Neurobiology, vol. 46, no. 1, pp. 41–54, 2012.

[134] M. Beekes, A. Thomzig, W. J. Schulz-Schaeffer, and R. Burger, "Is there a risk of prion-like disease transmission by Alzheimer- or Parkinson-associated protein particles?," Acta Neuropathologica, pp. 463–476, 2014.

[135] P. Arosio, M. Vendruscolo, C. M. Dobson, and T. P. J. Knowles, "Chemical kinetics for drug discovery to combat protein aggregation diseases," Trends in Pharmacological Sciences, vol. 35, no. 3, pp. 127–135, 2014.

[136] A. Hawe, M. Sutter, and W. Jiskoot, "Extrinsic Fluorescent Dyes as Tools for Protein Characterization," Phar. Res., vol. 25, no. 7, pp. 1487–1499, 2008.

[137] P. Pratim Bose, U. Chatterjee, L. Xie, J. Johansson, E. Göthelid, and P. I. Arvidsson, "Effects of Congo Red on Aβ1-40 fibril formation process and morphology," ACS Chemical Neuroscience, vol. 1, no. 4, pp. 315–324, 2010.

[138] M. Groenning, "Binding mode of Thioflavin T and other molecular probes in the context of amyloid fibrils—current status," J. Chem. Biol., vol. 3, no. 1, pp. 1–18, 2010.

[139] Y. Porat, A. Abramowitz, and E. Gazit, "Inhibition of amyloid fibril formation by polyphenols: Structural similarity and aromatic interactions as a common inhibition mechanism," Chem. Biol. Drug Des., vol. 67, no. 1, pp. 27–37, 2006.

[140] A. Frydman-Marom, R. Shaltiel-Karyo, S. Moshe, and E. Gazit, "The generic amyloid formation inhibition effect of a designed small aromatic beta breaking peptide," Amyloid, vol. 18, no. 3, pp. 119–127, 2011.

[141] A. K. Buell, C. M. Dobson, T. P. J. Knowles, and M. E. Welland, "Interactions between amyloidophilic dyes and their relevance to studies of amyloid inhibitors," Biophys. J., vol. 99, no. 10, pp. 3492–3497, 2010.

[142] M. Biancalana and S. Koide, "Molecular mechanism of thioflavin-t binding to amyloid fibrils," Biochim Biophys ACTA, Proteins and Proteomics, vol. 1804, no. 7, pp. 1405–1412, 2010.

[143] H. Chander, A. Chauhan, and V. Chauhan, "Binding of proteases to fibrillar amyloid beta protein and its inhibition by congo red," J. Alzheimers Dis., vol. 12, no. 3, pp. 261–269, 2007.

[144] M. Biancalana, K. Makabe, A. Koide, and S. Koide, "Molecular mechanism of thioflavin-t binding to the surface of beta rich peptide self-assemblies," J. Mol. Biol., vol. 385, no. 4, pp. 1052–1063, 2009.

[145] V. N. Uversky, J. Li, and A. L. Fink, "Metal-triggered structural transformations, aggregation, and fibrillation of human alpha synuclein: A possible molecular link between parkinsons disease and heavy metal exposure," J. Biol. Chem., vol. 276, no. 47, pp. 44284–96, 2001.

[146] V. Fodera, F. Librizzi, M. Groenning, M. van de Weert, and M. Leone, "Secondary nucleation and accessible surface in insulin amyloid fibril formation," J. Phys. Chem., vol. 112, no. 12, pp. 3853–3858, 2008.

[147] S. I. A. Cohen, M. Vendruscolo, C. M. Dobson, and T. P. J. Knowles, "Nucleated polymerization with secondary pathways. i. time evolution of the principal moments," J. Chem. Phys., vol. 135, no. 6, p. 065105, 2011.

[148] S. I. A. Cohen, M. Vendruscolo, C. M. Dobson, and T. P. J. Knowles, "Nucleated polymerisation in the presence of pre-formed seed filaments," Int. J. Mol. Sci., vol. 12, no. 9, pp. 5844–5852, 2011.

[149] H. Levine III, "Stopped-flow kinetics reveal multiple phases of thioflavin t binding to alzheimer β (1-40) amyloid fibrils," Archives of biochemistry and biophysics, vol. 342, no. 2, pp. 306–316, 1997.

[150] W. Hoyer, T. Antony, D. Cherny, G. Heim, T. M. Jovin, and V. Subramaniam, "Dependence of alpha synuclein aggregate morphology on solution conditions," J. Mol. Biol., vol. 322, no. 2, p. 383–393, 2002.

[151] Y. Hong, L. Meng, S. Chen, C. W. T. Leung, L.-T. Da, M. Faisal, D.-A. Silva, J. Liu, J. W. Y. Lam, X. Huang, and B. Z. Tang, "Monitoring and inhibition of insulin fibrillation by a small organic fluorogen with aggregation-induced emission characteristics," J. Am. Chem. Soc., vol. 134, no. 3, p. 1680–1689, 2012.

[152] J.-B. Wang, Y.-M. Wang, and C.-M. Zeng, "Quercetin inhibits amyloid fibrillation of bovine insulin and destabilizes preformed fibrils," Biochemical and biophysical research communications, vol. 415, no. 4, pp. 675–679, 2011.

[153] L.-Q. Xu, S. Wu, A. K. Buell, S. I. Cohen, L.-J. Chen, W.-H. Hu, S. A. Cusack, L. S. Itzhaki, H. Zhang, T. P. Knowles, et al., "Influence of specific hsp70 domains on fibril formation of the yeast prion protein ure2," Phil. Trans. R. Soc. B, vol. 368, no. 1617, p. 20110410, 2013.

[154] K. W. Oh and C. H. Ahn, "A review of microvalves," Journal of micromechanics and microengineering, vol. 16, no. 5, p. R13, 2006.

[155] A. Abate and D. Weitz, "Single-layer membrane valves for elastomeric microfluidic devices," Applied Physics Letters, vol. 92, no. 24, p. 243509, 2008.

[156] K. L. Saar, Y. Zhang, T. Müller, C. P. Kumar, S. Devenish, A. Lynn, U. Łapińska, X. Yang, S. Linse, and T. P. Knowles, "On-chip label-free protein analysis with downstream electrodes for direct removal of electrolysis products," Lab on a Chip, vol. 18, no. 1, pp. 162–170, 2018.

[157] K. L. Saar, T. Müller, and T. P. Knowles, "Fluidic apparatus and methods," 2017. GB1720627.7, 11 December 2017.

[158] K. L. Saar, T. Müller, J. Charmet, P. K. Challa, and T. P. Knowles, "Enhancing the resolution of micro free flow electrophoresis through spatially controlled sample injection," Analytical chemistry, 2018.

[159] D. E. Raymond, A. Manz, and H. M. Wldmer, "Continuous Sample Pretreatment Using a Free-Flow Electrophoresis Device Integrated onto a Silicon Chip," Analytical chemistry, vol. 66, no. 18, pp. 2858–2865, 1994.

[160] B. R. Fonslow and M. T. Bowser, "Free-flow electrophoresis on an anodic bonded glass microchip," Analytical Chemistry, vol. 77, no. 17, pp. 5706–5710, 2005.

[161] W. Ebina, A. C. Rowat, and D. A. Weitz, "Electrodes on a budget: Micropatterned electrode fabrication by wet chemical deposition," Biomicrofluidics, vol. 3, no. 3, pp. 2605–2609, 2009.

[162] V. Kostal, B. R. Fonslow, E. A. Arriaga, and M. T. Bowser, "Fast determination of mitochondria electrophoretic mobility using micro free-flow electrophoresis," Analytical Chemistry, vol. 81, no. 22, pp. 9267–9273, 2009.

[163] D. G. Rackus, M. D. M. Dryden, J. Lamanna, A. Zaragoza, B. Lam, S. O. Kelley, and A. R. Wheeler, "A digital microfluidic device with integrated nanostructured microelectrodes for electrochemical immunoassays," Lab on a chip, vol. 15, no. 18, pp. 3776–3784, 2015.

[164] S. Wu, P. Wan, J. Li, D. Li, Y. Zhu, and F. He, "Multi-modality of pi distribution in whole proteome," Proteomics, vol. 6, no. 2, pp. 449–455, 2006.

[165] L. P. Kozlowski, "Proteome-pi: proteome isoelectric point database," Nucleic acids research, vol. 45, no. D1, pp. D1112–D1116, 2017.

[166] D. Kohlheyer, J. C. Eijkel, A. van den Berg, and R. Schasfoort, "Miniaturizing free-flow electrophoresis–a critical review," Electrophoresis, vol. 29, no. 5, pp. 977–993, 2008.

[167] S. Köhler, C. Weilbeer, S. Howitz, H. Becker, V. Beushausen, and D. Belder, "PDMS free-flow electrophoresis chips with integrated partitioning bars for bubble segregation.," Lab on a chip, vol. 11, no. 2, pp. 309–314, 2011.

[168] M. Mazereeuw, C. M. D. Best, U. R. Tjaden, H. Irth, and J. V. D. Greef, "Free Flow Electrophoresis Device for Continuous On-Line Separation in Analytical Systems . An Application in Biochemical Detection," Analytical Chemistry, vol. 72, no. 16, pp. 3881–3886, 2000.

[169] D. Kohlheyer, G. A. J. Besselink, S. Schlautmann, and R. B. M. Schasfoort, "Free-flow zone electrophoresis and isoelectric focusing using a microfabricated glass device with ion permeable membranes," Lab on a chip, vol. 6, no. 3, pp. 374–380, 2006.

[170] J. W. Albrecht and K. F. Jensen, "Micro freef-low ief enhanced by active cooling and functionalized gels," Electrophoresis, vol. 27, no. 24, pp. 4960–4969, 2006.

[171] G. Münchow, S. Hardt, J. P. Kutter, and K. Drese, "Electrophoretic partitioning of proteins in two-phase microflows," Lab on a Chip, vol. 7, no. 1, pp. 98–102, 2007.

[172] J. E. Prest, S. J. Baldock, P. R. Fielden, N. J. Goddard, R. Goodacre, R. O?Connor, and B. J. T. Brown, "Miniaturised free flow isotachophoresis of bacteria using an injection moulded separation device," Journal of Chromatography B, vol. 903, pp. 53–59, 2012.

[173] C. Herzog, G. F. Jochem, P. Glaeser, and S. Nagl, "Gas removal in free-flow electrophoresis using an integrated nanoporous membrane," Microchimica Acta, vol. 182, no. 3-4, pp. 887–892, 2015.

[174] D. Janasek, J. Franzke, and A. Manz, "Scaling and the design of miniaturized chemical-analysis systems.," Nature, vol. 442, no. 7101, pp. 374–380, 2006.

[175] C.-X. Zhang and A. Manz, "High-speed free-flow electrophoresis on chip," Analytical chemistry, vol. 75, no. 21, pp. 5759–5766, 2003.

[176] S. Köhler, C. Benz, H. Becker, E. Beckert, V. Beushausend, and D. Belder, "Micro free-flow electrophoresis with injection molded chips," RSC Advances, vol. 2, pp. 520–525, 2012.

[177] S. Jezierski, D. Belder, and S. Nagl, "Microfluidic free-flow electrophoresis chips with an integrated fluorescent sensor layer for real time ph imaging in isoelectric focusing," Chemical Communications, vol. 49, no. 9, pp. 904–906, 2013.

[178] B. Jung, K. Rose, M. Shusteff, A. Persat, and J. Santiago, "Liquid and gel electrodes for transverse free flow electrophoresis," Apr. 7 2015. US Patent 8,999,129.

[179] K. Macounová, C. R. Cabrera, and P. Yager, "Concentration and separation of proteins in microfluidic channels on the basis of transverse IEF," Analytical Chemistry, vol. 73, no. 7, pp. 1627–1633, 2001.

[180] N. W. Frost and M. T. Bowser, "Using buffer additives to improve analyte stream stability in micro free flow electrophoresis.," Lab on a chip, vol. 10, no. 10, pp. 1231–1236, 2010.

[181] B. R. Fonslow and M. T. Bowser, "Optimizing band width and resolution in micro-free flow electrophoresis," Analytical Chemistry, vol. 78, no. 24, pp. 8236–8244, 2006.

[182] R. T. Turgeon and M. T. Bowser, "Micro free-flow electrophoresis: theory and applications," Anal and Bioanal Chem, vol. 394, no. 1, pp. 187–198, 2009.

[183] N. A. Mortensen, F. Okkels, and H. Bruus, "Reexamination of hagen-poiseuille flow: Shape dependence of the hydraulic resistance in microchannels," Physical Review E, vol. 71, no. 5, p. 057301, 2005.

[184] L. Nuttall, "The diffusion coefficient of potassium chloride in aqueous solution at," Annals of the New York Academy of Sciences, vol. 51, pp. 781–788, 1949.

[185] A. M. Friedman and J. W. Kennedy, "The Self-diffusion Coefficients of Potassium, Cesium, Iodide and Chloride Ions in Aqueous Solutions," Journal of the American Chemical Society, vol. 77, no. 17, p. 4499, 1955.

[186] U. Böhme and U. Scheler, "Effective charge of bovine serum albumin determined by electrophoresis NMR," Chemical Physics Letters, vol. 435, no. 4-6, pp. 342–345, 2007.

[187] B. Jachimska and A. Pajor, "Physico-chemical characterization of bovine serum albumin in solution and as deposited on surfaces," Bioelectrochemistry, vol. 87, pp. 138–146, 2012.

[188] E. Hermansson, S. Schultz, D. Crowther, S. Linse, B. Winblad, G. Westermark, J. Johansson, and J. Presto, "The chaperone domain brichos prevents cns toxicity of amyloid-β peptide in drosophila melanogaster," Disease models & mechanisms, vol. 7, no. 6, pp. 659–665, 2014.

[189] S. I. Cohen, P. Arosio, J. Presto, F. R. Kurudenkandy, H. Biverstål, L. Dolfe, C. Dunning, X. Yang, B. Frohm, M. Vendruscolo, et al., "A molecular chaperone breaks the catalytic cycle that generates toxic aβ oligomers," Nature structural & molecular biology, vol. 22, no. 3, pp. 207–213, 2015.

[190] D. E. Raymond, A. Manz, and H. M. Widmer, "Continuous separation of high molecular weight compounds using a microliter volume free-flow electrophoresis microstructure.," Analytical chemistry, vol. 68, no. 15, pp. 2515–2522, 1996.

[191] D. Belder and M. Ludwig, "Surface modification in microchip electrophoresis," Electrophoresis, vol. 24, no. 21, pp. 3595–3606, 2003.

[192] J. Wen, E. W. Wilker, M. B. Yaffe, and K. F. Jensen, "Microfluidic preparative free-flow isoelectric focusing: system optimization for protein complex separation," Anal Chemi, vol. 82, no. 4, pp. 1253–1260, 2010.

[193] J. Shao, L.-Y. Fan, C.-X. Cao, X.-Q. Huang, and Y.-Q. Xu, "Quantitative investigation of resolution increase of free-flow electrophoresis via simple interval sample injection and separation," Electrophoresis, vol. 33, no. 14, pp. 2065–2074, 2012.

[194] T. Müller, P. Arosio, L. Rajah, S. I. Cohen, E. V. Yates, M. Vendruscolo, C. M. Dobson, and T. P. Knowles, "Particle-based simulations of steady-state mass transport at high p\'eclet numbers," Int J Nonlinear Sci, no. 3-4, pp. 175–183.

[195] A. C. Johnson and M. T. Bowser, "Micro free flow electrophoresis," Lab Chip, vol. 18, no. 1, pp. 27–40, 2018.

[196] G. Weber and P. Boček, "Optimized continuous flow electrophoresis," Electrophoresis, vol. 17, no. 12, pp. 1906–1910, 1996.

[197] A. Piruska, I. Nikcevic, S. H. Lee, C. Ahn, W. R. Heineman, P. A. Limbach, and C. J. Seliskar, "The autofluorescence of plastic materials and chips measured under laser irradiation," Lab Chip, vol. 5, no. 12, pp. 1348–1354, 2005.

[198] J. D. Ramsey, S. C. Jacobson, C. T. Culbertson, and J. M. Ramsey, "High-efficiency, two-dimensional separations of protein digests on microfluidic devices," Analytical Chemistry, vol. 75, no. 15, pp. 3758–3764, 2003.

[199] M. Geiger, N. W. Frost, and M. T. Bowser, "Comprehensive multidimensional separations of peptides using nano-liquid chromatography coupled with micro free flow electrophoresis," Analytical chemistry, vol. 86, no. 10, pp. 5136–5142, 2014.

[200] F. Shang, E. Guihen, and J. D. Glennon, "Recent advances in miniaturisation–the role of microchip electrophoresis in clinical analysis," Electrophoresis, vol. 33, no. 1, pp. 105–116, 2012.

[201] Y. Huang, S. Zhao, M. Shi, and H. Liang, "A microchip electrophoresis strategy with online labeling and chemiluminescence detection for simultaneous quantification of thiol drugs," Journal of pharmaceutical and biomedical analysis, vol. 55, no. 5, pp. 889–894, 2011.

[202] M. A. Schwarz and P. C. Hauser, "Rapid chiral on-chip separation with simplified amperometric detection," Journal of Chromatography A, vol. 928, no. 2, pp. 225–232, 2001.

[203] H.-L. Lee and S.-C. Chen, "Microchip capillary electrophoresis with amperometric detection for several carbohydrates," Talanta, vol. 64, no. 1, pp. 210–216, 2004.

[204] Y.-H. Dou, N. Bao, J.-J. Xu, and H.-Y. Chen, "A dynamically modified microfluidic poly (dimethylsiloxane) chip with electrochemical detection for biological analysis," Electrophoresis, vol. 23, no. 20, pp. 3558–3566, 2002.

[205] N. A. Lacher, K. E. Garrison, R. S. Martin, and S. M. Lunte, "Microchip capillary electrophoresis/electrochemistry," Electrophoresis, vol. 22, no. 12, pp. 2526–2536, 2001.

[206] E. Poehler, C. Herzog, C. Lotter, S. A. Pfeiffer, D. Aigner, T. Mayr, and S. Nagl, "Label-free microfluidic free-flow isoelectric focusing, ph gradient sensing and near real-time isoelectric point determination of biomolecules and blood plasma fractions," Analyst, vol. 140, no. 22, pp. 7496–7502, 2015.

[207] S. Ohla and D. Belder, "Chip-based separation devices coupled to mass spectrometry," Current opinion in chemical biology, vol. 16, no. 3, pp. 453–459, 2012.

[208] A. Oedit, P. Vulto, R. Ramautar, P. W. Lindenburg, and T. Hankemeier, "Lab-on-a-chip hyphenation with mass spectrometry: strategies for bioanalytical applications," Current opinion in biotechnology, vol. 31, pp. 79–85, 2015.

[209] X. He, Q. Chen, Y. Zhang, and J.-M. Lin, "Recent advances in microchip-mass spectrometry for biological analysis," TrAC Trends in Analytical Chemistry, vol. 53, pp. 84–97, 2014.

[210] N. Pamme, "Continuous flow separations in microfluidic devices.," Lab on a chip, vol. 7, no. 12, pp. 1644–59, 2007.

[211] T. Herling, T. Mueller, and T. Knowles, "Fluidic analysis and separation," Feb. 23 2017. US Patent App. 15/307,221.

[212] A. Lomakin, G. B. Benedek, and D. B. Teplow, "[27] monitoring protein assembly using quasielastic light scattering spectroscopy," in Methods in enzymology, vol. 309, pp. 429–459, Elsevier, 1999.

[213] J. Szymański, E. Poboży, M. Trojanowicz, A. Wilk, P. Garstecki, and R. Hołyst, "Net charge and electrophoretic mobility of lysozyme charge ladders in solutions of nonionic surfactant," The Journal of Physical Chemistry B, vol. 111, no. 19, pp. 5503–5510, 2007.

[214] G. Yu, J. Liu, and J. Zhou, "Mesoscopic coarse-grained simulations of hydrophobic charge induction chromatography (hcic) for protein purification," AIChE Journal, vol. 61, no. 6, pp. 2035–2047, 2015.

[215] R. Zilionis, J. Nainys, A. Veres, V. Savova, D. Zemmour, A. M. Klein, and L. Mazutis, "Single-cell barcoding and sequencing using droplet microfluidics," nature protocols, vol. 12, no. 1, p. 44, 2017.

[216] E. Z. Macosko, A. Basu, R. Satija, J. Nemesh, K. Shekhar, M. Goldman, I. Tirosh, A. R. Bialas, N. Kamitaki, E. M. Martersteck, et al., "Highly parallel genome-wide expression profiling of individual cells using nanoliter droplets," Cell, vol. 161, no. 5, pp. 1202–1214, 2015.

[217] A. M. Klein, L. Mazutis, I. Akartuna, N. Tallapragada, A. Veres, V. Li, L. Peshkin, D. A. Weitz, and M. W. Kirschner, "Droplet barcoding for single-cell transcriptomics applied to embryonic stem cells," Cell, vol. 161, no. 5, pp. 1187–1201, 2015.

[218] Y. Liu, A. Beyer, and R. Aebersold, "On the dependency of cellular protein levels on mrna abundance," Cell, vol. 165, no. 3, pp. 535–550, 2016.

[219] I. Weibrecht, E. Lundin, S. Kiflemariam, M. Mignardi, I. Grundberg, C. Larsson, B. Koos, M. Nilsson, and O. Söderberg, "In situ detection of individual mrna molecules and protein complexes or post-translational modifications using padlock probes combined with the in situ proximity ligation assay," Nature protocols, vol. 8, no. 2, p. 355, 2013.

[220] B. P. Nicolet, A. Guislain, and M. C. Wolkers, "Combined single-cell measurement of cytokine mrna and protein identifies t cells with persistent effector function," The Journal of Immunology, p. 1601531, 2016.

[221] N. Fortelny, C. M. Overall, P. Pavlidis, and G. V. C. Freue, "Can we predict protein from mrna levels?," Nature, vol. 547, no. 7664, p. E19, 2017.

[222] H. Gong, X. Wang, B. Liu, S. Boutet, I. Holcomb, G. Dakshinamoorthy, A. Ooi, C. Sanada, G. Sun, and R. Ramakrishnan, "Single-cell protein-mrna correlation analysis enabled by multiplexed dual-analyte co-detection," Scientific Reports, vol. 7, no. 1, p. 2776, 2017.

[223] S. Darmanis, C. J. Gallant, V. D. Marinescu, M. Niklasson, A. Segerman, G. Flamourakis, S. Fredriksson, E. Assarsson, M. Lundberg, S. Nelander, et al., "Simultaneous multiplexed measurement of rna and proteins in single cells," Cell reports, vol. 14, no. 2, pp. 380–389, 2016.

[224] J. P. Robinson and M. Roederer, "Flow cytometry strikes gold," Science, vol. 350, no. 6262, pp. 739–740, 2015.

[225] S. C. Bendall, G. P. Nolan, M. Roederer, and P. K. Chattopadhyay, "A deep profiler's guide to cytometry," Trends in immunology, vol. 33, no. 7, pp. 323–332, 2012.

[226] D. R. Bandura, V. I. Baranov, O. I. Ornatsky, A. Antonov, R. Kinach, X. Lou, S. Pavlov, S. Vorobiev, J. E. Dick, and S. D. Tanner, "Mass cytometry: technique for real time single cell multitarget immunoassay based on inductively coupled plasma time-of-flight mass spectrometry," Analytical chemistry, vol. 81, no. 16, pp. 6813–6822, 2009.

[227] S. C. Bendall, E. F. Simonds, P. Qiu, D. A. El-ad, P. O. Krutzik, R. Finck, R. V. Bruggner, R. Melamed, A. Trejo, O. I. Ornatsky, et al., "Single-cell mass cytometry of differential immune and drug responses across a human hematopoietic continuum," Science, vol. 332, no. 6030, pp. 687–696, 2011.

[228] P. Shahi, S. C. Kim, J. R. Haliburton, Z. J. Gartner, and A. R. Abate, "Abseq: ultrahigh-throughput single cell protein profiling with droplet microfluidic barcoding," Scientific reports, vol. 7, p. 44447, 2017.

[229] M. Wilhelm, J. Schlegl, H. Hahne, A. M. Gholami, M. Lieberenz, M. M. Savitski, E. Ziegler, L. Butzmann, S. Gessulat, H. Marx, et al., "Mass-spectrometry-based draft of the human proteome," Nature, vol. 509, no. 7502, p. 582, 2014.

[230] "Dbco-peg5-nhs ester - instructions," September 2018. [online] https://clickchemistrytools.com/wp-content/uploads/2015/12/Instructions_A102P_rev1.pdf.

[231] H. Gong, I. Holcomb, A. Ooi, X. Wang, D. Majonis, M. A. Unger, and R. Ramakrishnan, "Simple method to prepare oligonucleotide-conjugated antibodies and its application in multiplex protein detection in single cells," Bioconjugate chemistry, vol. 27, no. 1, pp. 217–225, 2016.

[232] C. Vogel and E. M. Marcotte, "Insights into the regulation of protein abundance from proteomic and transcriptomic analyses," Nature Reviews Genetics, vol. 13, no. 4, p. 227, 2012.

[233] J. J. Li, P. J. Bickel, and M. D. Biggin, "System wide analyses have underestimated protein abundances and the importance of transcription in mammals," PeerJ, vol. 2, p. e270, 2014.

[234] N. Annabi, A. Tamayol, J. A. Uquillas, M. Akbari, L. E. Bertassoni, C. Cha, G. Camci-Unal, M. R. Dokmeci, N. A. Peppas, and A. Khademhosseini, "25th anniversary article: Rational design and applications of hydrogels in regenerative medicine," Advanced materials, vol. 26, no. 1, pp. 85–124, 2014.

[235] E. W. Young and D. J. Beebe, "Fundamentals of microfluidic cell culture in controlled microenvironments," Chemical Society Reviews, vol. 39, no. 3, pp. 1036–1048, 2010.

[236] P. Domachuk, K. Tsioris, F. G. Omenetto, and D. L. Kaplan, "Bio-microfluidics: biomaterials and biomimetic designs," Advanced materials, vol. 22, no. 2, pp. 249–260, 2010.

[237] D. Sinton, "Energy: the microfluidic frontier," Lab on a Chip, vol. 14, no. 17, pp. 3127–3134, 2014.

[238] K. Hasan, H. B. Yildiz, E. Sperling, P. Ó. Conghaile, M. A. Packer, D. Leech, C. Hägerhäll, and L. Gorton, "Photo-electrochemical communication between cyanobacteria (Leptolyngbia sp.) and osmium redox polymer modified electrodes," Physical Chemistry Chemical Physics, vol. 16, no. 45, pp. 24676–24680, 2014.

[239] A. J. McCormick, P. Bombelli, A. M. Scott, A. J. Philips, A. G. Smith, A. C. Fisher, and C. J. Howe, "Photosynthetic biofilms in pure culture harness solar energy in a mediatorless bio-photovoltaic cell (BPV) system," Energy & Environmental Science, vol. 4, no. 11, pp. 4699–4709, 2011.

[240] "International Energy Agency, Solar Energy Perspectives," 2011.

[241] "British Petroleum, BP Statistical Review of World Energy," 2015.

[242] M. A. Green, "Commercial progress and challenges for photovoltaics," Nature Energy, vol. 1, p. 15015, 2016.

[243] G. W. Crabtee and N. S. Lewis, "Solar energy conversion," Physics Today, vol. 60, no. 3, pp. 37–42, 2007.

[244] N. S. Lewis and D. G. Nocera, "Powering the planet: Chemical challenges in solar energy utilization," Proceedings of the National Academy of Sciences, vol. 103, no. 43, pp. 15729–15735, 2006.

[245] C. S. Tao, J. Jiang, and M. Tao, "Natural resource limitations to terawatt-scale solar cells," Solar Energy Materials and Solar Cells, vol. 95, no. 12, pp. 3176–3180, 2011.

[246] L. M. Peter, "Towards sustainable photovoltaics: the search for new materials," Philosophical Transactions of the Royal Society of London A: Mathematical, Physical and Engineering Sciences, vol. 369, no. 1942, pp. 1840–1856, 2011.

[247] K. A. Mazzio and C. K. Luscombe, "The future of organic photovoltaics," Chemical Society Reviews, vol. 44, no. 1, pp. 78–90, 2014.

[248] M. Hambourger, G. F. Moore, D. M. Kramer, D. Gust, A. L. Moore, and T. A. Moore, "Biology and technology for photochemical fuel production," Chemical Society Reviews, vol. 38, no. 1, pp. 25–35, 2009.

[249] Y. Zou, J. Pisciotta, R. B. Billmyre, and I. V. Baskakov, "Photosynthetic microbial fuel cells with positive light response," Biotechnology and Bioengineering, vol. 104, no. 5, pp. 939–946, 2009.

[250] A. J. McCormick, P. Bombelli, R. W. Bradley, R. Thorne, T. Wenzel, and C. J. Howe, "Biophotovoltaics: oxygenic photosynthetic organisms in the world of bioelectrochemical systems," Energy Environ. Sci., vol. 8, no. 4, pp. 1092–1109, 2015.

[251] K. L. Saar, P. Bombelli, D. J. Lea-Smith, T. Call, E.-M. Aro, T. Müller, C. J. Howe, and T. P. Knowles, "Enhancing power density of biophotovoltaics by decoupling storage and power delivery," Nature Energy, vol. 3, no. 1, p. 75, 2018.

[252] T. M. Squires and S. R. Quake, "Microfluidics: Fluid physics at the nanoliter scale," Reviews of modern physics, vol. 77, no. 3, p. 977, 2005.

[253] R. Ferrigno, A. D. Stroock, T. D. Clark, M. Mayer, and G. M. Whitesides, "Membraneless vanadium redox fuel cell using laminar flow," Journal of the American Chemical Society, vol. 124, no. 44, pp. 12930–12931, 2002.

[254] J. Yang, S. Ghobadian, P. J. Goodrich, R. Montazami, and N. Hashemi, "Miniaturized biological and electrochemical fuel cells: challenges and applications," Physical Chemistry Chemical Physics, vol. 15, no. 34, pp. 14147–14161, 2013.

[255] E. Kjeang, B. T. Proctor, A. G. Brolo, D. A. Harrington, N. Djilali, and D. Sinton, "High-performance microfluidic vanadium redox fuel cell," Electrochimica Acta, vol. 52, no. 15, pp. 4942–4946, 2007.

[256] H. Ren, C. I. Torres, P. Parameswaran, B. E. Rittmann, and J. Chae, "Improved current and power density with a micro-scale microbial fuel cell due to a small characteristic length," Biosensors and Bioelectronics, vol. 61, pp. 587–592, 2014.

[257] J. P. Brody and P. Yager, "Diffusion-based extraction in a microfabricated device," Sensors and Actuators A: Physical, vol. 58, no. 1, pp. 13–18, 1997.

[258] A. E. Kamholz, B. H. Weigl, B. A. Finlayson, and P. Yager, "Quantitative analysis of molecular interaction in a microfluidic channel: the T-sensor," Analytical Chemistry, vol. 71, no. 23, pp. 5340–5347, 1999.

[259] R. W. Bradley, P. Bombelli, S. J. Rowden, and C. J. Howe, "Biological photovoltaics: intra-and extra-cellular electron transport by cyanobacteria," Biochemical Society Transactions, vol. 40, no. 6, pp. 1302–1307, 2012.

[260] P. Bombelli, R. W. Bradley, A. M. Scott, A. J. Philips, A. J. McCormick, S. M. Cruz, A. Anderson, K. Yunus, D. S. Bendall, P. J. Cameron, J. M. Davies, A. G. Smith, C. J. Howe, and A. C. Fisher, "Quantitative analysis of the factors limiting solar power transduction by Synechocystis sp. PCC 6803 in biological photovoltaic devices," Energy & Environmental Science, vol. 4, no. 11, pp. 4690–4698, 2011.

[261] F. Zhao, R. C. Slade, and J. R. Varcoe, "Techniques for the study and development of microbial fuel cells: an electrochemical perspective," Chemical Society Reviews, vol. 38, no. 7, pp. 1926–1939, 2009.

[262] B. E. Logan, B. Hamelers, R. Rozendal, U. Schröder, J. Keller, S. Freguia, P. Aelterman, W. Verstraete, and K. Rabaey, "Microbial fuel cells: methodology and technology," Environmental Science & Technology, vol. 40, no. 17, pp. 5181–5192, 2006.

[263] F. Qian, M. Baum, Q. Gu, and D. E. Morse, "A 1.5 μl microbial fuel cell for on-chip bioelectricity generation," Lab on a Chip, vol. 9, no. 21, pp. 3076–3081, 2009.

[264] P. Bombelli, T. Müller, T. W. Herling, C. J. Howe, and T. P. Knowles, "A high power-density, mediator-free, microfluidic biophotovoltaic device for cyanobacterial cells," Advanced Energy Materials, vol. 5, no. 2, p. e1401299, 2015.

[265] E. Kjeang, N. Djilali, and D. Sinton, "Microfluidic fuel cells: A review," Journal of Power Sources, vol. 186, no. 2, pp. 353–369, 2009.

[266] S. A. M. Shaegh, N.-T. Nguyen, and S. H. Chan, "A review on membraneless laminar flow-based fuel cells," International Journal of Hydrogen Energy, vol. 36, no. 9, pp. 5675–5694, 2011.

[267] Z. Li, Y. Zhang, P. R. LeDuc, and K. B. Gregory, "Microbial electricity generation via microfluidic flow control," Biotechnology and Bioengineering, vol. 108, no. 9, pp. 2061–2069, 2011.

[268] D. J. Lea-Smith, P. Bombelli, R. Vasudevan, and C. J. Howe, "Photosynthetic, respiratory and extracellular electron transport pathways in cyanobacteria," Biochimica et Biophysica Acta (BBA)-Bioenergetics, vol. 1857, no. 3, pp. 247–255, 2016.

[269] D. J. Lea-Smith, R. Vasudevan, and C. J. Howe, "Generation of marked and markerless mutants in model cyanobacterial species," JoVE (Journal of Visualized Experiments), no. 111, p. e54001, 2016.

[270] D. O. Hall and K. K. Rao, Photosynthesis - Sixth edition. Cambridge University Press, 1999.

[271] E. Hao Yu, S. Cheng, K. Scott, and B. Logan, "Microbial fuel cell performance with non-Pt cathode catalysts," Journal of Power Sources, vol. 171, no. 2, pp. 275–281, 2007.

[272] R. Kakarla and B. Min, "Photoautotrophic microalgae scenedesmus obliquus attached on a cathode as oxygen producers for microbial fuel cell MFC operation," International Journal of Hydrogen Energy, vol. 39, no. 19, pp. 10275–10283, 2014.

[273] K. Schneider, R. J. Thorne, and P. J. Cameron, "An investigation of anode and cathode materials in photomicrobial fuel cells," Phil. Trans. R. Soc. A, vol. 374, no. 2061, p. 20150080, 2016.

[274] F. Qian and D. E. Morse, "Miniaturizing microbial fuel cells," Trends in biotechnology, vol. 29, no. 2, pp. 62–69, 2011.

[275] D. J. C. MacKay, "Solar energy in the context of energy use, energy transportation and energy storage," Phil. Trans. R. Soc. A, vol. 371, no. 1996, p. 20110431, 2013.

[276] J. O. Dabiri, J. R. Greer, J. R. Koseff, P. Moin, J. Peng, R. H. Knapp Jr, B. G. Levi, and D. M. Kammen, "A new approach to wind energy: opportunities and challenges," in AIP Conference Proceedings, vol. 1652, pp. 51–57, AIP, 2015.

[277] C. De Castro, M. Mediavilla, L. J. Miguel, and F. Frechoso, "Global solar electric potential: A review of their technical and sustainable limits," Renewable and Sustainable Energy Reviews, vol. 28, pp. 824–835, 2013.

[278] T. Kaneko, S. Sato, H. Kotani, A. Tanaka, E. Asamizu, Y. Nakamura, N. Miyajima, M. Hirosawa, M. Sugiura, S. Sasamoto, et al., "Sequence analysis of the genome of the unicellular cyanobacterium synechocystis sp. strain pcc6803. ii. sequence determination of the entire genome and assignment of potential protein-coding regions," DNA research, vol. 3, no. 3, pp. 109–136, 1996.

[279] J. L. Ried and A. Collmer, "An nptI-sacB-sacR cartridge for constructing directed, unmarked mutations in gram-negative bacteria by marker exchange-eviction mutagenesis," Gene, vol. 57, no. 2-3, pp. 239–246, 1987.